

8-15-2014

Theoretical Investigation of Heterogeneous Catalysis at the Solid–Liquid Interface for the Conversion of Lignocellulosic Biomass Model Molecules

Muhammad Faheem
University of South Carolina - Columbia

Follow this and additional works at: <https://scholarcommons.sc.edu/etd>

 Part of the [Chemical Engineering Commons](#)

Recommended Citation

Faheem, M. (2014). *Theoretical Investigation of Heterogeneous Catalysis at the Solid–Liquid Interface for the Conversion of Lignocellulosic Biomass Model Molecules*. (Doctoral dissertation). Retrieved from <https://scholarcommons.sc.edu/etd/2770>

This Open Access Dissertation is brought to you by Scholar Commons. It has been accepted for inclusion in Theses and Dissertations by an authorized administrator of Scholar Commons. For more information, please contact dillarda@mailbox.sc.edu.

THEORETICAL INVESTIGATION OF HETEROGENEOUS CATALYSIS AT THE
SOLID–LIQUID INTERFACE FOR THE CONVERSION OF LIGNOCELLULOSIC
BIOMASS MODEL MOLECULES

by

Muhammad Faheem

Bachelor of Science

University of Engineering & Technology – Lahore, 2007

Master of Science

University of Engineering & Technology – Lahore, 2009

Submitted in Partial Fulfillment of the Requirements

For the Degree of Doctor of Philosophy in

Chemical Engineering

College of Engineering and Computing

University of South Carolina

2014

Accepted by:

Andreas Heyden, Major Professor

John Weidner, Committee Member

John Monnier, Committee Member

Mark Uline, Committee Member

Vitaly Rassolov, Committee Member

Lacy Ford, Vice Provost and Dean of Graduate Studies

© Copyright by Muhammad Faheem, 2014
All rights reserved.

DEDICATION

To my parents and my wife without whose love, prayers, and sacrifices, this work could not have been completed.

ACKNOWLEDGEMENTS

My stay at the University of South Carolina and successful completion of graduate school owes a lot to the support of many wonderful people. It is a pleasure to have the opportunity to express my gratitude to them.

First and foremost, my thanks are due to my advisor, Dr. Andreas Heyden, for the opportunity he provided me to pursue my doctoral studies in his research group and for his continuous support and encouragement over the years. He has been an incredible mentor and his enthusiasm for research has been the most important driving force at all stages of this work. I would also like to thank Dr. John Weidner, Dr. John Monnier, Dr. Mark Uline, and Dr. Vitaly Rassolov for serving on my advisory committee and Dr. Jochen Lauterbach for serving on my pre-defense committee. Their feedback has been very helpful for improving this dissertation.

I am grateful to all members of the Heyden research group for being great coworkers and friends. It has been a memorable experience working with this group of amazing people. I must give special recognition to Dr. Salai Cheettu Ammal and Dr. Jianmin Lu. Salai helped a great deal to get me started with my project and has always been there, both professionally and personally. And long discussions and arguments with Jianmin over the “correct” way of performing different types of calculations have been crucial for stimulating new research and mutual learning.

I am thankful to the staff members of the Department of Chemical Engineering for their administrative support, which made my graduate school experience very pleasant. I would also like to acknowledge the United States Department of Energy for financial support, and USC Nanocenter, ANL, ORNL, PNNL, NERSC, and XSEDE for supercomputing resources.

Finally, I wish to recognize and thank my family. None of this would have been possible without their unconditional love and support.

ABSTRACT

Catalytic conversion of biomass-derived oxygenates to fuels and value-added chemicals is a promising strategy in the search for renewable and sustainable energy sources. Most relevant catalytic processes are carried out in an aqueous environment using supported transition metal catalysts. The reaction network consists of multiple series and parallel pathways leading to formation of hydrogen, alkanes, and lighter oxygenates. The final product distribution ultimately depends on the sequence and competition of C–C, C–O, C–H, and O–H bonds scissions. Ethylene glycol (EG) is the simplest model molecule of various biomass-derived polyols that has a C:O stoichiometry of 1:1 and contains all relevant C–C, C–O, C–H, and O–H bonds. While the reaction mechanism of EG reforming is to some degree understood at the metal–gas interface, lack of a well-established methodology for describing the influence of a complex liquid phase on a reaction across a solid–liquid interface has hindered similar theoretical studies in an aqueous environment.

In this dissertation, we show how first-principles calculations can be used for a systematic investigation of complex reaction pathways at a metal–water interface. We proposed a multistep strategy where the description of the influence of an aqueous environment on reaction kinetics and equilibria is successively refined. First, we developed a new computational approach for implicit solvation of periodic metal slabs by integrating planewave density functional theory (DFT) calculations with an implicit

solvation model. Rapid convergence with size of the metal cluster and basis set was demonstrated for C–C cleavage in dehydrogenated EG at a Pt (111)/H₂O interface. The method was then successfully applied for predicting experimentally reported CO frequency shifts in water at Pt (111)/H₂O and Pd (111)/H₂O interfaces. Next, we developed a hybrid quantum mechanics/molecular mechanics (QM/MM) method to allow an explicit description of water molecules at the metal–water interface, and applied it to construct the complete free energy profile for a model C–C cleavage reaction. Finally, we investigated the mechanism of EG reforming over Pt (111) in vapor and aqueous phases from first-principles calculations and developed microkinetic models for the respective phases. Initial dehydrogenation of EG was found to be rate-determining under operating conditions which is in agreement with experimental observations.

TABLE OF CONTENTS

DEDICATION	iii
ACKNOWLEDGEMENTS.....	iv
ABSTRACT	vi
LIST OF TABLES	xi
LIST OF FIGURES	xiii
CHAPTER 1: INTRODUCTION	1
1.1. Energy from Lignocellulosic Biomass.....	1
1.2. Scope and Objectives of this Dissertation	3
1.3. Organization of this Dissertation	5
1.4. References.....	8
CHAPTER 2: LITERATURE REVIEW	10
2.1. Chemistry of Biomass.....	10
2.2. Aqueous-Phase Processing of Oxygenated Hydrocarbons	12
2.3. Aqueous-Phase Processing of Ethylene Glycol.....	17
2.4. Computational Studies	23
2.5. Force Fields for Molecular Dynamics Simulations	26
2.6. References.....	28
CHAPTER 3: COMPUTATIONAL METHODS	38
3.1. Density Functional Theory	38
3.2. Conductor-Like Screening Model (COSMO).....	40

3.3. Periodic Electrostatic Embedded Cluster Method (PEECM)	41
3.4. Microkinetic Modeling	42
3.5. References.....	44
CHAPTER 4: NEW IMPLICIT SOLVATION SCHEME FOR SOLID SURFACES	46
4.1. Summary	46
4.2. Introduction.....	46
4.3. Computational Details	49
4.4. Results and Discussion	51
4.5. Conclusions.....	55
4.6. References.....	55
CHAPTER 5: HYBRID QUANTUM MECHANICS/MOLECULAR MECHANICS SOLVATION SCHEME FOR COMPUTING FREE ENERGIES OF REACTIONS AT METAL–WATER INTERFACES	62
5.1. Summary	62
5.2. Introduction.....	63
5.3. Theory	68
5.4. Computational Details	83
5.5. Results and Discussion	87
5.6. Conclusions.....	96
5.7. References.....	97
CHAPTER 6: ETHYLENE GLYCOL REFORMING ON Pt (111): FIRST-PRINCIPLES MICROKINETIC MODELING IN VAPOR AND AQUEOUS PHASES	111
6.1. Summary	111
6.2. Introduction.....	112
6.3. Computational Methods.....	114
6.4. Model Development.....	117

6.5. Results and Discussion	121
6.6. Conclusions.....	133
6.7. References.....	134
CHAPTER 7: CONCLUSIONS AND FUTURE RESEARCH DIRECTIONS.....	154
7.1. Conclusions.....	154
7.2. Future Research Directions.....	157
APPENDIX A: SUPPLEMENTARY INFORMATION FOR CHAPTER 4	158
APPENDIX B: SUPPLEMENTARY INFORMATION FOR CHAPTER 5.....	161
APPENDIX C: SUPPLEMENTARY INFORMATION FOR CHAPTER 6.....	164
APPENDIX D: PERMISSION TO REPRINT	182

LIST OF TABLES

Table 4.1. Effect of water on CO adsorption on Pd (111) and Pt (111).	57
Table 5.1. Structural changes in the presence of water for reactant, product, and transition state.	100
Table 5.2. Effect of water on reaction free energy and activation barrier.	101
Table 6.1. Lateral interaction parameters used in the microkinetic model.	137
Table 6.2. Energetics (eV) of surface reactions in the limit of zero coverage.	138
Table 6.3. Energetics (eV) of adsorption reactions in the limit of zero coverage.	143
Table 6.4. Kinetic properties at 500 K for vapor- and aqueous-phase reforming of ethylene glycol over Pt (111).	144
Table 6.5. Sensitivity analysis for vapor- and aqueous-phase reforming of ethylene glycol over Pt (111).	145
Table 6.6. Summary of vapor- and aqueous-phase microkinetic model predictions with dispersion effects included.	146
Table A.1. Results from periodic-slab calculations (vacuum) for CO on Pd (111) and Pt (111) with PBE functional.	158
Table A.2. Results from iSMS calculations (water) for CO on Pd (111) and Pt (111) with PBE functional.	159
Table A.3. Results from iSMS calculations (vacuum/water) for CO on Pd (111) and Pt (111) with PBE0 functional.	160
Table B.1. ESP-fitted and NPA charges for a 51-atom, Pt (111) cluster.	161
Table C.1. Binding modes and number of occupied surface sites for all surface intermediates.	164
Table C.2. Imaginary frequencies and transition state bond lengths for all surface reactions included in the microkinetic model.	169

Table C.3. Number of unique structures used for fitting CO–CO and H–H lateral interactions.....	180
Table C.4. Number of unique structures used for fitting EG–CO and EG–H lateral interactions (EG = Ethylene Glycol).....	180
Table C.5. Number of unique structures used for fitting CO–H lateral interactions.....	181

LIST OF FIGURES

Figure 2.1. Chemical structure of biomass-derived compounds including: (A) cellulose with β -1,4 glycoside linkages, (B) starches with α -1,4 and α -1,6 glycoside linkages, and (C) structural monomer units of lignin.....	32
Figure 2.2. Process conditions for the catalytic conversion of petroleum and biomass feedstocks.....	33
Figure 2.3. Reaction pathways for the production of alkanes from sorbitol over multifunctional catalysts containing metal and acid sites.....	34
Figure 2.4. Relative rates of C–C bond breaking reaction (white), water-gas shift reaction (grey), and methanation reaction (black). The rate of a particular reaction can be compared for different metals; however, for a specific metal, the absolute rates of the three reactions cannot be compared relative to each other.	35
Figure 2.5. Thermodynamic pathways among stable compounds in ethylene glycol reforming. Each reaction is defined in its thermodynamically favorable direction, and equilibrium constants are listed per mole of reactant at 498 K.....	36
Figure 2.6. Factors controlling the selectivity of aqueous-phase reforming process.....	37
Figure 4.1. Schematic representation of equation (4.1) for calculation of $\Delta G_{\text{surface,rxn}}^{\text{water}}$ for C–C bond cleavage in dehydrogenated ethylene glycol on Pt (111) in water. Arrows connect reactant (up) to cleavage products (down) in the respective models. The four models from left to right are periodic slab in water, periodic slab in vacuum, cluster in water, and cluster in vacuum. Explicit water molecules are shown for illustrative purposes only.....	58
Figure 4.2. Convergence of $\Delta G_{\text{surface,rxn}}^{\text{water}}$ for C–C bond cleavage in dehydrogenated ethylene glycol on Pt (111) in water with iSMS scheme. A value of 9.3 kcal/mol obtained for a $(5 \times 5) \times 4$ cluster is used as reference (solid horizontal line). Cluster model calculations in implicit solvent (without iSMS) are shown as dashed curves.....	59
Figure 4.3. Basis set convergence for C–C cleavage in dehydrogenated ethylene glycol on a $5 \times 5 \times 2$ cluster of Pt (111).	60

Figure 4.4. Shift in electronic density of states (DOS) due to water for 24-atom Pd (111) cluster with and without CO adsorbed on an fcc site. Only metal d-states are plotted for each case. 61

Figure 5.1. Algorithm for geometry optimization using eSMS method. Abbreviations used for QM methods are PW (planewave), GTO (Gaussian-type orbitals), and PEECM (periodic electrostatic embedded cluster method). 102

Figure 5.2. Side (upper panel) and top (lower panel) views of optimized structures on Pt (111) slab in vacuum: (a) reactant, (b) coadsorbed products, and (c) transition state for the reaction $\text{CHOH} - \text{CHOH} \rightarrow 2(\text{CHOH})$ 103

Figure 5.3. QM clusters selected for convergence test of eSMS with respect to cluster size: final state with 7 water molecules is shown. (a) Cluster contains Pt atoms directly bound to CHOH species and their nearest neighbors. (b) Cluster contains all Pt atoms of cluster “a” plus addition rows of Pt atoms involved in screening the Pt atoms that form chemical bounds to CHOH species. (c) Cluster contains all Pt atoms of cluster “b” plus an additional ring of Pt atoms. (d) Benchmark cluster model. 104

Figure 5.4. Convergence of eSMS with size of QM cluster (computed with VASP 5.2). Solid horizontal lines show reference values for $\Delta E_{\text{surface,rxn}}^{\text{water}}$ and $\Delta E_{\text{surface,rxn}}^{\text{vacuum}}$ for a $12 \times 12 \times 4$ Pt (111) slab. Dashed horizontal lines mark a tolerance of ± 0.02 eV about $\Delta E_{\text{surface,rxn}}^{\text{water}}$. Solid lines with filled markers are eSMS results for the four types of QM clusters shown in Figure 5.3. Dashed lines with hollow markers are corresponding results for $\Delta E_{\text{cluster,rxn}}^{\text{water}}$ without using eSMS. For each cluster type, 1–4 layer thick clusters are considered. 233-atom, 4-layer cluster of type “d” is not shown on this scale. 105

Figure 5.5. Convergence of eSMS with size of QM cluster (periodic planewave QM calculations integrated with nonperiodic QM calculations). Solid horizontal lines show reference values of $\Delta E_{\text{surface,rxn}}^{\text{water}}$ and $\Delta E_{\text{surface,rxn}}^{\text{vacuum}}$ for a $12 \times 12 \times 4$ Pt (111) slab. Dashed horizontal lines mark a tolerance of ± 0.02 eV around $\Delta E_{\text{surface,rxn}}^{\text{water}}$. Solid lines with filled markers are eSMS results for two layer clusters of types “a”, “b”, and “c”, as shown in Figure 5.3. Dashed lines with hollow markers are corresponding results for $\Delta E_{\text{cluster,rxn}}^{\text{water}}$ without using eSMS. 106

Figure 5.6. Initial state of dehydrogenated ethylene glycol on a two layer, 51-atom cluster with 2250 TIP3P water molecules. Pt–QM (dark blue), Pt–MM (light blue), C–QM (gray), O–QM (red), and H–QM (white) atoms are shown as solid spheres. MM water molecules are shown as lines with O (red) and H (white) vertices. 107

Figure 5.7. Validation of fixed-charge approximation. Difference between total QM/MM energies of 2 QM conformations is evaluated in an ensemble of 50

representative water conformations using exact QM calculations (X-axis) and with the assumption of fixed QM charges (Y-axis)..... 108

Figure 5.8. Liquid-phase optimization of reactant, product, and transition states using QM/MM-FEP. All free energies are relative to the respective initial states. 109

Figure 5.9. Free energy profile (without vibrational contributions to the partition function/free energy) for the reaction $\text{CHOH} - \text{CHOH} \rightarrow 2(\text{CHOH})$. Dashed vertical lines correspond to gas-phase structures of the reactant state (index = 0), transition state (index = 42), and product state (index = 77). For index 0 to 77 the QM/MM-FEP profile is calculated using the same structures as in the gas phase. Results of QM/MM-FEP optimization are included to the left of the gas phase reactant state (index < 0) and to the right of gas phase product state (index > 77). In addition, the gas phase transition state structure is replaced with the transition state structure obtained in liquid water and steps to the left and right are recalculated. The difference between the results depicted here and Table 5.2 originate from the inclusion of vibrational contributions in Table 5.2. 110

Figure 6.1. Effect of temperature on coverage of most abundant surface intermediates (A), and overall turnover frequency (B) in vapor-phase reforming of ethylene glycol over Pt (111)..... 147

Figure 6.2. Effect of carbon monoxide partial pressure (A), hydrogen partial pressure (B), ethylene glycol partial pressure (C), and total pressure (D) on overall turnover frequency in vapor-phase reforming of ethylene glycol over Pt (111) at 500 K..... 148

Figure 6.3. Free energy diagram at 500 K for vapor-phase reforming of ethylene glycol over Pt in the limit of zero coverage. Species labels show surface intermediates sorted (top to bottom) in order of increasing stability. Percent labels show fraction of the overall reaction flux passing through different pathways and are sorted (top to bottom) in order of increasing stability of respective transition states. Only those pathways are labeled that contribute more than 2% of the overall reaction flux. Excess hydrogen atoms are adsorbed on separate slabs and omitted from labels for simplicity..... 149

Figure 6.4. Comparison of vapor- and aqueous-phase reforming of ethylene glycol over Pt (111). (A) Contribution of initial C–H and O–H scission pathways to total rate of ethylene glycol decomposition. (B) Ratio of reaction rates in aqueous and vapor phases..... 150

Figure 6.5. Effect of temperature on surface coverages of most abundant intermediates (A) and overall turnover frequency (B) in aqueous-phase reforming of ethylene glycol over Pt (111)..... 151

Figure 6.6. Effect of carbon monoxide partial pressure (A), hydrogen partial pressure (B), ethylene glycol partial pressure (C), and total pressure (D) on overall

turnover frequency in aqueous-phase reforming of ethylene glycol over Pt (111)
at 500 K..... 152

Figure 6.7. Free energy diagram at 500 K for aqueous-phase reforming of
ethylene glycol over Pt in the limit of zero coverage. Species labels show surface
intermediates sorted (top to bottom) in order of increasing stability. Percent labels
show fraction of the overall reaction flux passing through different pathways and
are sorted (top to bottom) in order of increasing stability of respective transition
states. Only those pathways are labeled that contribute more than 2% of the
overall reaction flux. Excess hydrogen atoms are adsorbed on separate slabs and
omitted from labels for simplicity..... 153

CHAPTER 1

INTRODUCTION

1.1. Energy from Lignocellulosic Biomass

The quest for alternative energy resources is driven by increasing global energy demands, rapidly depleting fossil fuel reserves, and environmental considerations. World demand for oil, for example, is expected to increase from 87 million barrels/day in 2010 to 115 million barrels/day by 2040 with the transportation sector accounting for two-thirds of this projected increase. Using non-food biomass for production of liquid hydrocarbon fuels is an important option to meet these challenges. It has been estimated that the United States has the capacity to grow and convert enough biomass to replace nearly a third of the nation's current gasoline use.¹⁻³ In particular, lignocellulosic biomass can be sustainably produced at costs that are significantly lower (about \$15 per barrel of oil energy equivalent) than crude oil.⁴⁻⁵ Lignocellulosic biomass includes lignin and fibrous, woody, and generally inedible portions of plants that are composed of cellulose and hemicellulose. It may be derived from forest residues such as tree bark and scrap wood, urban wood residues such as site-clearing debris, municipal paper waste, agricultural wastes such as corn stover and sugarcane bagasse, and dedicated energy crops grown on marginal lands and therefore does not compete with food production. However, significant research challenges exist to develop technologies for economically converting raw biomass into transportation fuels.

Conversion of lignocellulosic biomass to liquid fuels is accomplished using three main routes: gasification, thermal liquefaction or pyrolysis, and hydrolysis.⁶ Gasification is carried out at high temperatures (> 1000 K) to produce syngas, a mixture of H_2 and CO, which is then converted to alkanes via Fischer–Tropsch synthesis⁷⁻⁸ or to methanol via methanol synthesis.⁹⁻¹⁰ However, because of its high energy requirements, the gasification route becomes cost-effective only for large scale processing units where the economics of scale can in principle reduce the unit fuel cost, but where transportation costs of biomass to a central processing location also become significant (because of low energy density of raw biomass).¹¹ Selective thermal processing techniques such as liquefaction and fast pyrolysis thermally decompose the biomass feedstock into liquid bio-oil products that consist of complex mixtures of highly oxygenated molecules and must be refined to produce liquid fuels.¹² Finally, acid and enzyme hydrolysis of lignocellulosic biomass separates carbohydrate/sugar and lignin fractions which can be further processed to produce hydrogen and liquid alkanes from sugars¹³⁻¹⁴ and aromatics from lignin.⁵

Aqueous-phase processing (APP) of biomass feedstocks offers unique advantages for achieving high yield and selectivity for production of hydrogen and liquid alkanes with targeted molecular weights that can be directly used as alternatives to petroleum-based transportation fuels. The process can be carried out at significantly lower temperatures (~ 500 K) compared to gasification, liquefaction and pyrolysis. Under these operating conditions, the water-gas shift (WGS) reaction is thermodynamically favored and the product stream has low CO concentration (100–1000 ppm)¹⁵⁻¹⁶ which makes it suitable for fuel cell applications.¹⁷ The raw biomass must first be pretreated to produce a

feedstock containing sugars and polyols which is then catalytically reformed to desired products in aqueous phase, thus lowering the overall energy requirements of the process by eliminating the need to vaporize the reaction mixture. Furthermore, the reaction products include hydrogen (gas) and immiscible water and hydrocarbon (liquid) phases which self-separate thereby circumventing the need for energy-intensive distillation steps. Finally, APP allows processing of thermally unstable reactant molecules (for example, sugars) in liquid phase, thus avoiding their thermal decomposition which not only improves the overall yield and selectivity of the process but also increases the effective life of the catalyst by reducing the rate of tar and ash deposit in catalyst pores. It is also worth noting that the overall energy efficiency (defined as the ratio of heating value of final product to energy required to produce the product) is approximately 2.2 for APP¹⁸ which compares very favorably with the energy efficiency for the production of bio-ethanol (~1.4).¹⁹

1.2. Scope and Objectives of this Dissertation

The principle idea of APP is to remove excess functionality (for example, $-OH$, $-C=O$, $-CHO$, and $-COOH$ functional groups) from biomass-derived oxygenated compounds in a controlled manner. Because of their high functionality, these oxygenated feedstocks are generally highly reactive and the conversion process is a complex reaction mechanism involving a myriad of reactions. A fundamental challenge to achieve higher selectivity is the ability to effectively and selectively break or make $C-C$, $C-O$, $C-H$, and $O-H$ bonds on a supported metal catalyst in an aqueous environment. However, lack of a well-established methodology for describing the influence of dynamical fluctuations of a complex liquid on a reaction across a solid-liquid interface with quantum

mechanical accuracy and inadequate understanding of structure–activity relationships for heterogeneous catalysis in liquid phase pose significant challenges for application of computational techniques to rational design of catalysts for such processes.

Even if the water molecules do not directly participate in an elementary reaction, the presence of an aqueous environment has the potential to dramatically affect the activity and selectivity of a catalyst by changing the free energies of reactants, products, and transition states by stabilizing or destabilizing charged moieties.²⁰ Activation barriers and reaction rates of elementary steps occurring at a solid–liquid interface can therefore be very different from when the same elementary reactions occur at a solid–gas interface.²¹ To correctly account for the effect of dynamical fluctuations in a complex liquid environment and long range interactions between water molecules, the computational model must include at least a few hundred (if not thousands) of solvent molecules, making it practically impossible to use *ab initio* molecular dynamics (AIMD)²² approaches for systematic investigations of various reaction pathways for the conversion of complex molecules using currently available computational technology and resources. This necessitates the development of alternative computational approaches that are nearly as accurate as AIMD but computationally multiple (5–7) orders of magnitude less expensive.

The objective of this dissertation is to develop and validate an efficient and accurate computational approach for the prediction of reaction kinetics and equilibria at a solid–liquid interface. This approach is then utilized to obtain a fundamental understanding of the overall reaction mechanism under APP conditions by accounting for the specific effects of an aqueous environment on the activity and selectivity of a

transition metal catalyst. In particular, a multistep strategy is proposed where the description of the influence of an aqueous environment on reaction kinetics and equilibria is successively refined. First, a novel computational approach is developed for implicit solvation of periodic metal slabs by integrating periodic planewave density functional theory (DFT) calculations with a nonperiodic continuum solvation model. The goal of this development is to perform a preliminary screening of the reaction network to identify those elementary reactions and surface intermediates that are most affected by an aqueous environment. Next, the quantum mechanics/molecular mechanics free energy perturbation (QM/MM-FEP) method,²³⁻²⁴ originally developed for enzymatic reactions, is extended for application to heterogeneous catalysis in water. The objective of this development is to improve the description of the effects of an aqueous environment for prescreened elementary reactions and surface intermediates by allowing an explicit description of water molecules at the metal–water interface. Finally, the reaction mechanism of ethylene glycol reforming over Pt (111) is investigated in vapor and aqueous phases from first-principles calculations and detailed microkinetic models are developed for the respective phases. This microkinetic analysis is used to obtain insights into the similarities and differences in the ethylene glycol reforming chemistry in vapor and aqueous phases over platinum.

1.3. Organization of this Dissertation

Chapter 2, “Literature Review”, begins with a brief introduction to the biomass chemistry followed by an account of the current state of knowledge of aqueous-phase processing of lignocellulosic biomass. Reforming of ethylene glycol as a model molecule for larger biomass-derived sugars and polyols is comprehensively reviewed with

particular attention to various reaction pathways and thermodynamic, kinetic and selectivity challenges that affect the final product distribution. Previous experimental and computational studies relevant for this work are discussed in detail.

Chapter 3, “Computational Methods”, provides a brief description and theoretical background for various computational approaches used in this dissertation (in Chapters 4, 5, and 6). A more detailed account of the particular methodology specific to a chapter is included as a subsection of that chapter.

Chapter 4, “New Implicit Solvation Scheme for Solid Surfaces”, presents the development of a novel computational approach for implicit solvation of periodic metal slabs. Considering that the continuum solvation models are widely used for nonperiodic molecular systems,²⁵⁻²⁶ whereas periodic DFT calculations can account for the long range metal interactions at an affordable computational cost, it is proposed that the two approaches can be integrated for modeling chemical reactions at metal–water interfaces. Rapid convergence of this scheme with size of the metal cluster and the basis set is demonstrated using a model C–C bond cleavage reaction in dehydrogenated ethylene glycol at a Pt (111)/H₂O interface. The method is then successfully applied for predicting experimentally reported CO frequency shifts in water at Pt (111)/H₂O and Pd (111)/H₂O interfaces.

Chapter 5, “Hybrid Quantum Mechanics/Molecular Mechanics Solvation Scheme for Computing Free Energies of Reactions at Metal–Water Interfaces”, builds upon the concept introduced in Chapter 4. The continuum solvation model is now replaced with molecular dynamics (MD) simulations to allow an explicit description of water molecules at the metal–water interface to account for the dynamical fluctuations in liquid phase. A

potential of mean force (PMF) of the reaction system within the QM/MM framework is derived and integrated with the free energy perturbation method. Using the same C–C cleavage reaction as a test case, gas-phase structures of reactant, product, and transition states are optimized in water using both implicit and explicit solvation schemes. The complete free energy profile for the reaction coordinate is constructed by introducing intermediate states and calculating free energy differences between adjacent states. Results from both implicit and explicit solvation schemes are in good agreement and suggest that changes in intramolecular hydrogen bonding in the adsorbed moieties in an aqueous environment lead to a higher activation barrier for C–C cleavage.

Chapter 6, “Ethylene Glycol Reforming on Pt (111): First-Principles Microkinetic Modeling in Vapor and Aqueous Phases”, presents a detailed computational study of the Pt catalyzed ethylene glycol decomposition for hydrogen production. Detailed microkinetic models are developed to provide insights into the similarities and differences in the reaction chemistry in both phases. The vapor-phase microkinetic model, parametrized using DFT-derived reaction energies and activations barriers, reveals that only the initial dehydrogenation steps are rate controlling. The aqueous phase microkinetic model, parameterized using the continuum solvation approach introduced in Chapter 4, predicts that an aqueous environment increases the rate of decomposition by lowering the activation energy. A comparison of reaction orders and sensitivity coefficients however shows that the reaction chemistry is similar in both phases. These results are in agreement with previous computational and experimental studies.

Chapter 7, “Conclusions and Future Research directions”, summarizes important findings of this work and suggests directions for future research. Furthermore, a logical

procedure for using first-principles calculations for systematic investigation of complex reaction pathways at a metal–water interface is outlined.

1.4. References

1. Perlack, R. D.; Wright, L. L.; Turhollow, A. F.; Graham, R. L.; Stokes, B. J.; Erbach, D. C. *Biomass as Feedstock for a Bioenergy and Bioproducts Industry: The Technical Feasibility of a Billion-Ton Annual Supply*; Oak Ridge National Laboratory (ORNL): 2005.
2. Downing, M.; Eaton, L. M.; Graham, R. L.; Langholtz, M. H.; Perlack, R. D.; Turhollow Jr, A. F.; Stokes, B.; Brandt, C. C. *U.S. Billion-Ton Update: Biomass Supply for a Bioenergy and Bioproducts Industry*; Oak Ridge National Laboratory (ORNL): 2011.
3. Bell, A. T.; Gates, B. C.; Ray, D. *Basic Research Needs: Catalysis for Energy – Report from the U.S. Department of Energy, Office of Basic Energy Sciences Workshop, August 6-8, 2007, in Bethesda, Maryland*; Pacific Northwest National Laboratory (PNNL), Richland, WA (US): 2007.
4. Huber, G. W. *Breaking the Chemical and Engineering Barriers to Lignocellulosic Biofuels: Next Generation Hydrocarbon Biorefineries*; University of Massachusetts Amherst: 2008.
5. Huber, G. W.; Iborra, S.; Corma, A. *Chem. Rev.* **2006**, *106*, 4044–4098.
6. Huber, G. W.; Dumesic, J. A. *Catal. Today* **2006**, *111*, 119–132.
7. Schulz, H. *Appl. Catal., A* **1999**, *186*, 3–12.
8. Tijmensen, M. J. A.; Faaij, A. P. C.; Hamelinck, C. N.; van Hardeveld, M. R. M. *Biomass Bioenergy* **2002**, *23*, 129–152.
9. Chmielniak, T.; Sciazko, M. *Appl. Energy* **2003**, *74*, 393–403.
10. Lee, S. G.; Sardesai, A. *Top. Catal.* **2005**, *32*, 197–207.
11. Hamelinck, C. N.; Faaij, A. P. C.; den Uil, H.; Boerrigter, H. *Energy* **2004**, *29*, 1743–1771.
12. Lin, Y. C.; Huber, G. W. *Energy Environ. Sci.* **2009**, *2*, 68–80.
13. Huber, G. W.; Shabaker, J. W.; Dumesic, J. A. *Science* **2003**, *300*, 2075–2077.
14. Davda, R. R.; Shabaker, J. W.; Huber, G. W.; Cortright, R. D.; Dumesic, J. A. *Appl. Catal., B* **2005**, *56*, 171–186.
15. Davda, R. R.; Dumesic, J. A. *Angew. Chem., Int. Ed.* **2003**, *42*, 4068–4071.
16. Kandoi, S.; Greeley, J.; Simonetti, D.; Shabaker, J.; Dumesic, J. A.; Mavrikakis, M. *J. Phys. Chem. C* **2011**, *115*, 961–971.
17. Tanksale, A.; Beltramini, J. N.; Lu, G. M. *Renewable Sustainable Energy Rev.* **2010**, *14*, 166–182.
18. Huber, G. W.; Chheda, J. N.; Barrett, C. J.; Dumesic, J. A. *Science* **2005**, *308*, 1446–1450.
19. Shapouri, H.; Gallagher, P. W.; Nefstead, W.; Schwartz, R.; Noe, S.; Conway, R. *2008 Energy Balance for the Corn-Ethanol Industry*; U.S. Department of Agriculture: 2010.
20. Rossmeisl, J.; Logadottir, A.; Norskov, J. K. *Chem. Phys.* **2005**, *319*, 178–184.
21. Hibbitts, D. D.; Loveless, B. T.; Neurock, M.; Iglesia, E. *Angew. Chem., Int. Ed.* **2013**, *52*, 12273–12278.
22. Iftimie, R.; Minary, P.; Tuckerman, M. E. *Proc. Natl. Acad. Sci. U.S.A.* **2005**, *102*, 6654–6659.
23. Lu, Z. Y.; Yang, W. T. *J. Chem. Phys.* **2004**, *121*, 89–100.

24. Hu, H.; Lu, Z. Y.; Yang, W. T. *J. Chem. Theory Comput.* **2007**, *3*, 390–406.
25. Cramer, C. J.; Truhlar, D. G. *Chem. Rev.* **1999**, *99*, 2161–2200.
26. Tomasi, J.; Mennucci, B.; Cammi, R. *Chem. Rev.* **2005**, *105*, 2999–3093.

CHAPTER 2

LITERATURE REVIEW

2.1. Chemistry of Biomass

Plants capture solar energy as fixed carbon, from carbon dioxide and water, in a sugar building block $(\text{CH}_2\text{O})_x$, through photosynthesis. The sugar produced by this process is stored in a polymeric form, which depends on the type of the plant material. Plant biomass is typically composed of 75–90 wt.% of sugar polymers, with the other 10–25 wt.% being large organic aromatic compounds called lignin.¹⁻² Other components of biomass present in minor amounts include triglycerides, alkaloids, pigments, resins, sterols, terpenes, terpenoids, and waxes.³

Sugars in biomass are stored in three different types of polymers: starches, cellulose, and hemicellulose. Cellulose forms the skeletal structure of most plant biomass and has a low surface area crystalline form. It is a polysaccharide containing glucose monomer units connected through β -1,4 glycoside linkages (Figure 2.1) and can be broken down to glucose dimer, trimer, and tetramer by partial acid hydrolysis or to glucose monomer by complete acid hydrolysis.⁴ Starches structurally differ from cellulose only in the way glucose monomers are linked: they contain α -1,4 and α -1,6 glycoside linkages in various ratios. Starches can be broken down into water-insoluble amylose (10–20 wt.%) and water-soluble amylopectin (80–90 wt.%) fractions upon treatment with hot water.³ Amylose is a tightly packed linear polymer of D-glucose units

connected through α -1,4 glycoside linkages and is more resistant to digestion than other starch molecules. Amylopectin is a polysaccharide with both α -1,4 and α -1,6 glycoside linkages and possesses a branched structure that can be relatively easily attacked by enzymes allowing for easier hydrolysis. Hemicellulose is a complex polymer of five-carbon (xylose and arabinose) and six-carbon (galactose, glucose, and mannose) sugars, all of which are highly substituted by acetic acid. Hemicellulose is amorphous because of its branched structure and can be relatively easily hydrolyzed to its constituent sugars.⁵ Finally, lignin consists of highly branched, substituted, mononuclear aromatic polymers and is often associated with the cellulose and hemicellulose materials making up lignocellulose compounds.³

The crystalline portion of lignocellulosic biomass is composed of cellulose, whereas amorphous hemicellulose occurs in association with cellulose and lignin. Lignin makes up the walls of lignocellulosic material and protects cellulose and hemicellulose from direct attack by acid hydrolysis necessitating an effective pretreatment step to break the lignin seal. Other factors that make lignocellulosic materials difficult to convert to monomeric sugars include high crystallinity of cellulose, low surface area of the material, heterogeneous character of biomass particles, and cellulose sheathing by hemicellulose. After a suitable pretreatment step such as uncatalyzed steam explosion, treatment in liquid hot water or pH-controlled hot water, flow through hot water or dilute acid, or treatment with lime or ammonia, lignocellulosic biomass can be broken down into sugar monomers by acid or enzyme hydrolysis.⁴⁻⁶

2.2. Aqueous-Phase Processing of Oxygenated Hydrocarbons

2.2.1. Overview

Petroleum-based transportation fuels are mainly mixtures of hydrocarbons with only small fraction of functionalized organic compounds (that is, those containing oxygen and other elements). Biomass-derived compounds, on the other hand, are mainly carbohydrates and contain excess functionality for use as transportation fuels. Any biomass-for-energy strategy must therefore involve an effective mechanism for selective removal of this excess functionality. Carbohydrate feedstocks are generally highly reactive, have low volatility, and decompose at high temperatures commonly employed in the petroleum industry. However, because of their high water solubility, these carbohydrate feedstocks can be processed in an aqueous environment at lower temperatures. Figure 2.2 shows that while petroleum processing is mainly carried out at high temperatures and in vapor phase, biomass feedstocks are processed over a wide range of process conditions.⁷ Pyrolysis, gasification, liquefaction, and vapor-phase reforming are some processing techniques that involve a high-temperature treatment of the biomass feedstock. On the other hand, aqueous-phase processing (APP) is carried out at significantly lower temperatures and pressures (~ 500 K, ~ 50 bar).⁸

Aqueous-phase catalytic processing of biomass-derived oxygenated hydrocarbons was originally developed for the production of hydrogen.⁹⁻¹² Later catalytic routes were found for direct production of liquid alkanes with targeted molecular weights.¹³⁻¹⁴ The principle idea of APP, whether targeted toward hydrogen or alkane production, is to remove excess functionality (for example, $-\text{OH}$, $-\text{C}=\text{O}$, $-\text{CHO}$, and $-\text{COOH}$ functional groups) from biomass-derived oxygenates in a controlled manner. The selectivity toward desired products is therefore directly affected by the ability to effectively and selectively

break or make C–C, C–O, C–H, and O–H bonds on a supported-metal catalyst in an aqueous environment. In particular, reducing the oxygen content of intermediate species is important to control their high reactivity and may be accomplished via dehydration, hydrogenolysis or decarboxylation/decarbonylation mechanisms.¹⁵ Because the biomass-derived oxygenates are C₅- and C₆-sugars and their derivatives, the largest alkane that can be produced by selective removal of oxygen functionality only is hexane. C–C coupling mechanisms such as aldol-condensation and oligomerization are therefore important for the production of heavier transportation fuels with targeted molecular weights.¹⁶

Several reactions occur in an APP process leading to parallel selectivity challenges and complicating the design of suitable catalysts. Figure 2.3 shows a proposed reaction network for APP of sorbitol over a multifunctional catalyst with metal and acid sites (Pt/Al₂O₃-SiO₂).¹³ Hydrogen is produced by C–C cleavage and water-gas shift (WGS) reactions on metal sites. Light alkanes (primarily methane and ethane) are produced as a result of rapid cleavage of C–C and C–O bonds by metal sites and also by methanation and Fischer–Tropsch reactions on some metals (for example, Ru). Heavier alkanes (primarily hexane) are produced by repeated cycles of dehydration and hydrogenation of sorbitol where dehydration occurs on the acid sites followed by hydrogenation of the unsaturated bonds by metal sites. Alkanes with longer carbon chains (C₁₀-C₂₀) for direct use as diesel fuels are obtained by C–C coupling reactions of carbonyl groups (for example, through base-catalyzed aldol-condensation).¹⁶⁻¹⁷ The final product distribution depends on the relative rates of C–C bond cleavage/formation, dehydration, and hydrogenation reactions, which in turn depend on the catalyst composition and reaction conditions.

From a computational point of view, the number of possible elementary reactions, intermediates and products as well as the computational expense associated with calculating individual model parameters (for example, binding energy) scale with the size of the molecule of interest. Using large carbon chains for computational studies of possible reaction pathways is therefore complicated and computationally prohibitive. It is more convenient to use smaller model molecules to study the overall reaction network and selectivity challenges thereof if these model molecules have similar molecular structures, functional groups and reaction pathways. Ethylene glycol (EG) and glycerol are particularly relevant feed molecules for studies of APP reaction mechanism because they contain the same functional characteristics as biomass-derived sugars and sugar-alcohols. These features include the presence of C–C, C–O, C–H, and O–H bonds, –OH groups attached to adjacent carbon atoms, and an overall C:O ratio of 1:1.^{12, 18} In section 2.3, mechanisms for hydrogen and alkane production, and thermodynamic and selectivity considerations for APP will be described using EG as model molecule.

2.2.2. Important Classes of Reactions

Development of processing technologies for biomass-derived oxygenates requires an understanding of the underlying chemistry. In the following, important classes of reactions pertinent to APP are briefly described.

Hydrolysis is the primary mechanism by which sugar monomers and their derivatives are obtained by cleaving the glycoside bonds in biomass-derived polysaccharides. The process is typically carried out at 370–570 K using mineral acid catalysts.^{7, 19-21} Base-catalyzed hydrolysis leads to more side reactions and is less common. The reaction proceeds by C–O–C bond cleavage at the intermediate oxygen

atom between two sugar monomer units. Hemicellulose and starches are more open to attack because of their branched structures and require modest temperatures and dilute acid concentrations for hydrolysis, which improves overall yield by minimizing further degradation of simple sugars.²² Cellulose is more difficult to hydrolyze because of its high crystallinity and relatively compact structure.

Dehydration is important for conversion of sugars to furan compounds (for example, furfural and HMF) that are subsequently converted to diesel fuel additives. Synthesis of hydroxymethylfurfural (HMF), for example, is based on triple dehydration of hexoses and has been studied in water, organic solvents, biphasic systems, ionic liquids, and near- or supercritical water, using a variety of catalysts such as mineral and organic acids, organocatalysts, salts and solid acid catalysts such as ion-exchange resins and zeolites in the temperature range 370–470 K.²³⁻²⁵ The process is more efficient in non-aqueous media both in terms of HMF yield and reaction temperature than in aqueous media.²⁶

Isomerization of carbohydrates is typically carried out in the presence of base catalysts (for example, magnesium-aluminum hydrotalcites) at mild temperatures (310–350 K).²⁷ The most important application of isomerization for APP is the glucose–fructose isomerization in aqueous media for production of HMF which proceeds via a fructose intermediate.²⁶ Carbohydrates in solution may be present as open chains or ring structures. The isomerization reaction proceeds via an intermediate enolate species formed from open-chain forms and results in transformation of aldohexoses (glucose) to ketohexoses (fructose). The rate of glucose conversion is therefore directly proportional

to its fraction in the open-chain form, which in turn is a function of the nature of solvent and reaction temperature.

Aldol-condensation is the most important C–C bond formation reaction for production of targeted molecular weight alkanes for diesel fuel replacement. C–C coupling reactions generally require an activated site next to the carbonyl functionality or an unsaturated C–C bond which may be either conjugated with the carbonyl functionality or isolated.²⁷ Aldol-condensation requires at least one carbonyl compound with α -hydrogen and is generally carried out at mild temperatures (300–370 K) in the presence of a base catalyst.⁷ An initial abstraction of α -hydrogen by the base catalyst results in the formation of an enolate which then attacks the carbon atom of the carbonyl group of another molecule to form a C–C bond. The final product distribution is a function of the nature of the solvent and catalyst material and process variables including reaction temperature, pH, and reactant molar ratio.²⁸

Hydrogenation reactions are important to saturate C=C and C=O bonds and are carried out at moderate temperatures (370–420 K) and pressures (10–30 bar) in the presence of metal catalysts (for example, Pt, Pd, and Ru).⁷ The rate of dehydration/hydrogenation reactions relative to C–C cleavage directly affects the final molecular weight distribution in liquid alkane production using APP. Hydrogen may be supplied externally or produced *in situ* by reforming reactions which eliminates certain problems including the need of high pressures to accumulate enough gas in solution, dissociation of H₂ on catalyst surface and its mass transport in water. Selective hydrogenation reactions are important in the production of biofuels. Selective hydrogenation of C=C bonds of HMF and furfural, for example, produces

tetrahydrofuran-2-carboxyaldehyde and 5-hydroxymethyl-tetrahydrofurfural. These species can undergo self aldol-condensation to produce liquid hydrocarbons ranging from C₈ to C₁₀.^{14, 28}

Hydrogenolysis is targeted at selectively cleaving C–C or C–O bonds in polyols to produce more valuable polyols and/or diols. For example, hydrogenolysis of glycerol under alkaline conditions in the presence of hydrogen over Pt/C and Ru/C catalysts at 473 K and 40 bar produces ethylene glycol, propylene glycol, lactic acid, and formic acid.²⁹⁻³⁰ C–C cleavage is thought to occur through a base-catalyzed retro-aldol-condensation followed by hydrogenation of the products whereas C–O cleavage is thought to occur through a base-catalyzed dehydration mechanism. The initial dehydrogenation step occurs on the transition metal catalyst.³¹

2.3. Aqueous-Phase Processing of Ethylene Glycol

2.3.1. Production of Hydrogen

Reforming of ethylene glycol for hydrogen production takes place according to the following stoichiometric reaction:



The reaction is highly favorable at low temperatures with an equilibrium constant on the order of 10⁷ at 500 K for APP of EG.¹⁸ The mechanism involves cleavage of C–C, C–H, and O–H bonds to form dehydrogenated species on the catalyst surface. Group VIII metals such as Pt, Pd and Rh readily cleave these bonds.³² EG undergoes dissociative adsorption on Pt to form CO at room temperature.³³⁻³⁴ EG also decomposes on Rh catalyst and CO and H₂ are the only desorbing products.³⁵ Because high CO coverage can

significantly decrease the catalytic activity, the adsorbed CO must be removed from the metal surface by the WGS reaction.



An effective reforming catalyst for hydrogen production must possess the following characteristics:

- (1) High activity for C–C bond cleavage at temperatures of interest for APP (which are significantly lower than those for vapor-phase processing).
- (2) High activity for the WGS reaction to remove adsorbed CO from the metal surface to avoid catalyst poisoning.
- (3) Low activity for C–O bond cleavage and hydrogenation, methanation and Fischer–Tropsch reactions which lead to the production of alcohols and alkanes and are thermodynamically highly favorable under APP conditions.

A comparison of the activities of different metals for these reactions is shown in Figure 2.4.^{18, 36-37}

2.3.2. Production of Alkanes

Selective production of light alkanes by APP of biomass-derived oxygenates occurs through repeated cycles of dehydration and hydrogenation reactions. Multifunctional catalysts, such as Pt/SiO₂-Al₂O₃, that contain acid sites for dehydration and metal sites for subsequent hydrogenation of the unsaturated bonds, have been found to be active and selective for the production of light alkanes.¹³ Since the overall reaction uses hydrogen gas to remove oxygen from the feed molecule as water, the largest alkane that can be produced by this process contains the same number of carbon atoms as the

oxygenated feed molecule. For example, production of ethane from EG occurs according to the following stoichiometric reaction:



Hydrogen gas required for this reaction may be produced in the same reactor by APP of the feed molecule or may be supplied from a different process. When using *in situ* hydrogen production, hydrogen generation must be balanced with its consumption which poses additional selectivity challenges.

Using biomass-derived sugar monomers and their derivatives, hexane is the largest alkane that can be produced by this process. However, high volatility of hexane makes it unsuitable for use as a fuel additive. To produce larger alkane molecules that can be used as a replacement for gasoline and diesel fuels, C–C coupling reactions are required. Aldol-condensation reactions are particularly relevant in this context because various species containing carbonyl functionality can be formed from carbohydrates and polyols. For example, dehydration of glucose and fructose respectively yield HMF and furfural which can undergo aldol-condensation with other carbonyl species such as acetone and glyceraldehyde.^{14, 38-41}

A multi-step strategy for producing larger alkanes with targeted molecular weights includes an initial reforming of a fraction of the carbohydrate feed over a Pt–Re/C catalyst to supply hydrogen gas that partially deoxygenates the remaining feed to monofunctional molecules such as alcohols, ketones, and carboxylic acids via a dehydration/hydrogenation process.⁴²⁻⁴³ These reactions remove more than 80% of the initial oxygen content of the sugars and polyols.⁴⁴ Endothermic reforming reactions are balanced by exothermic deoxygenation reactions in the same reactor such that the overall

reaction is only mildly exothermic and the reaction products contain more than 90% of the initial energy content of the oxygenated feed. An example of such step would be the production of acetaldehyde from EG:



These monofunctional organic compounds are then coupled by aldol-condensation or ketonization over catalysts such as CeZrO_x or $\text{CuMg}_{10}\text{Al}_7\text{O}_x$ to produce larger carbon chains.⁴²



Dehydration/hydrogenation of these monofunctional products converts them to alkanes and can be combined with the C–C coupling step.⁴⁴



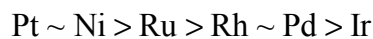
The overall coupling process of ketones, for example, with other species over a copper–alumina–magnesia catalyst consists of Cu-catalyzed dehydrogenation of alcohol groups, followed by base-catalyzed (MgO_x) aldol-condensation, acid-catalyzed (AlO_x) dehydration and subsequent Cu-catalyzed hydrogenation of the unsaturated aldol adduct.⁴⁴ An alternative coupling strategy is based on an initial dehydration of alcohols to olefins over solid acid catalysts such as niobic acid or niobium phosphate in the absence of hydrogen.⁴⁵ These olefins can then be oligomerized to larger carbon chains over zeolite-based catalysts.⁴⁴

2.3.3. Thermodynamics, Kinetics, and Selectivity Considerations

Thermodynamic relationships between stable species encountered in aqueous-phase processing of ethylene glycol are shown in Figure 2.5.⁴⁶ Reforming of EG to produce CO is thermodynamically highly favorable ($K = 10^8$) as are its dehydrogenation

to acetic acid ($K = 10^9$) and dehydration to acetaldehyde ($K = 10^6$). CO may undergo WGS reaction to produce more hydrogen ($K = 10^3$), or methanation to produce methane ($K = 10^9$), or Fischer–Tropsch synthesis to produce ethane ($K = 10^5$). Acetaldehyde is a highly reactive intermediate and produces ethane by further dehydration/deoxygenation ($K = 10^{12}$), methane and CO by C–C cleavage ($K = 10^{11}$), ethanol by hydrogenation ($K = 10^2$), and acetic acid by hydration ($K = 10^4$). Decomposition of all oxygenated intermediates (methanol, ethanol, acetic acid, and acetaldehyde) leads to formation of alkanes (methane and ethane) and is highly favorable under these conditions.⁴⁶ Overall, it is important to note that thermodynamics favors the production of H₂ from oxygenates in comparison to corresponding alkanes. This allows APP of oxygenates for hydrogen production to be carried out at significantly lower temperatures than classical vapor-phase steam reforming of natural gas. This again has the advantage that the WGS reaction can be operated at a much lower temperature where it is thermodynamically favorable for additional hydrogen production and CO removal from the surface.

While Figure 2.5 shows possible thermodynamic pathways for EG reforming, kinetics of individual reactions and final product distribution depend upon the nature of the catalyst and process conditions. For example, methanol is readily reformed to produce H₂ and CO₂ over Pt/Al₂O₃ and Sn-promoted Raney Ni (R-NiSn) catalysts. However, condensation of methanol to form EG and dehydration of EG to acetaldehyde are significantly slower reactions on a R-NiSn catalyst reducing the production of byproducts.⁴⁶ Using silica-supported metal catalysts, Dumesic and coworkers¹⁸ found that the overall rate of EG reforming at 483 K decreases in the order:



whereas the selectivity towards hydrogen production decreases in the order:



Considering good activity and long-term stability, Pt has been found to be the most suitable catalyst for hydrogen production from APP.^{6, 8} It has also been found that the nature of the catalyst support has a profound effect on the rate of hydrogen production⁴⁷ which decreases in order:



In general, acidic supports such as $\text{SiO}_2\text{-Al}_2\text{O}_3$ are more alkane-selective whereas basic and neutral supports such as Al_2O_3 and carbon are more H_2 selective.⁶ Tests using sintered $\text{Pt/Al}_2\text{O}_3$ catalyst have revealed that the effect of catalyst support on reforming activity and selectivity is greater than the effect of metal dispersion.⁴⁸ Finally, selectivity depends upon the feed molecule, with the smaller molecules being more H_2 -selective.⁹ Figure 2.6 summarizes the effects of various factors on the selectivity towards hydrogen or alkane production from aqueous-phase reforming of biomass-derived oxygenates.

Considering that monofunctional alkanes are the most desirable products from APP of carbohydrates and polyols and that *in situ* hydrogen production by reforming and WGS reactions is required for these conversions, an ideal catalyst should have high activity for (1) cleaving C–O bonds of fully functionalized molecules, and (2) WGS reaction, but limited activity for (1) cleaving C–C bonds of non-functionalized carbon atoms, (2) methanation, and (3) Fischer–Tropsch synthesis.

While all these selectivity issues can in principle be studied using computational tools, we do not concentrate on WGS, methanation and Fischer–Tropsch reactions in this

study and focus instead on a systematic investigation of Pt catalyzed EG decomposition for hydrogen production. In particular, we aim at better understanding the role of an aqueous environment by relating the activity and selectivity of various bond cleavage reactions to the polarity and hydrogen bonding ability of adsorbed intermediates and transition states.

2.4. Computational Studies

2.4.1. Vapor-Phase Reforming of Ethylene Glycol over Pt-Based Catalysts

Adsorption of oxygenates on transition metals and reactions pertinent to APP have been extensively studied using computational techniques.⁴⁹⁻⁵⁹ Only those studies most relevant to this work are briefly discussed in this section.

Skoplyak and coworkers^{53, 56} studied dehydrogenation and decarbonylation of ethylene glycol and ethanol over Pt (111) and Ni/Pt (111) bimetallic surfaces and showed that EG reacted via dehydrogenation to produce H₂ and CO. A linear correlation was observed between reforming activities of both oxygenates and surface d-band center.⁵⁷ Similar trends were observed for production of H₂ and CO from reforming of glycerol.⁶⁰ However, reforming selectivity could not be correlated to surface d-band center.

Using ethanol, ethylene glycol and isopropyl alcohol as model molecules, Saliccioli et al.⁵⁹ demonstrated that linear scaling relationships⁶¹⁻⁶² can be used to predict the binding energies of larger oxygenates on Pt and Pt-based bimetallic surfaces. They observed that C–H bond cleaving pathways tend to be thermodynamically favored over O–H bond cleaving pathways during EG dehydrogenation. DFT calculations later showed that thermal decomposition of EG on Pt (111) proceeds via initial O–H bond scission, followed by C–H cleavage and a second O–H bond scission. On a Ni/Pt (111)

bimetallic surface, both O–H bonds are cleaved initially. These results were confirmed by temperature-programmed desorption (TPD) and vibrational spectra.⁶³ A detailed first-principles microkinetic model was developed for prediction of experimentally observed kinetic trends. Sensitivity analysis confirmed catalyst poisoning by adsorbed CO and H and that only early dehydrogenation reactions are rate determining.⁶⁴⁻⁶⁵

Ethylene glycol differs from monofunctional alcohols in that it has a lower barrier for initial O–H cleavage than C–H cleavage. Stresses in bidentate EG-derived surface intermediates force the C–O bonds into an angle more perpendicular to the plane of the surface and facilitate proximity of the hydroxyl-hydrogen to the metal surface.^{56, 63} The bond breaking sequence for EG decomposition on Pt (111) is therefore different from decomposition pathways of monofunctional alcohols.^{51-52, 58} These observations support our choice of ethylene glycol over ethanol as model molecule for larger oxygenates. Because C–C cleaving intermediates and transition states are multiply bonded to the metal surface, the rate of C–C cleavage depends on the surface coverage of more abundant adsorbates. This assertion has been used to explain higher activity of Pt–Re catalyst (compared to Pt) for glycerol reforming since the blocking of active sites of mixed Pt–Re catalyst by reaction intermediates and products is less extensive.⁶⁶

Kandoi et al.⁶⁷ compared the kinetics of EG reforming over Pt in vapor and aqueous phases through microkinetic modeling based on a reduced mechanism of 7 lumped reactions. Brønsted–Evans–Polanyi-type correlations⁶¹⁻⁶² developed for monofunctional alcohols⁴⁹⁻⁵⁰ were used to estimate activation barriers for bond cleavage steps. Microkinetic model parameters were then fitted to available experimental data.^{47, 68} They observed that similar values of kinetic parameters could be used to describe the

experimental data for both vapor- and aqueous-phase reforming, suggesting that the reaction chemistry is similar in both phases.

2.4.2. Computational Studies at Metal–Water Interfaces

Reactions at solid–liquid interfaces are much less understood than their counterparts at solid–gas interfaces because of the challenge to accurately yet efficiently account for the dynamical effects of a liquid phase. In order to capture the effect of an aqueous environment on reaction chemistry during catalytic conversions, water molecules must be treated explicitly at the QM level which significantly increases the computational cost. In practice, it remains largely uncertain how many explicit water molecules would be sufficient for this purpose. One approach is to use a few explicit water molecules as the core solvation shell and to use a continuum solvation model to account for the long range electrostatic interactions from bulk water. This approach has been used to study the formation of water on Pt and Pt-based alloys⁶⁹ and the oxidation of formic acid at the Pt/H₂O interface.⁷⁰ While implicit solvation models significantly reduce the number of degrees of freedom of the system, they cannot correctly reproduce the anisotropic site-specific interactions⁷¹ between the solute and solvent molecules over a solid catalyst.

An alternative approach based on *ab initio* QM calculations consists of optimizing a hexagonally close-packed ice-like network of water molecules at the metal interface⁷²⁻⁷³ before replacing one of the water molecules with a reaction moiety. The preoptimized water network effectively serves as an initial guess for further geometry optimizations and transition state searches. This approach has been used to study methanol decomposition on Pt (111).⁵² Formation of an H₃O_{aq}⁺ ion and an electron, which is

donated to the metal surface, was observed. The heterolytic pathway ($\text{CH}_3\text{OH}_{\text{ad}} + \text{H}_2\text{O}_{\text{aq}} \rightarrow \text{CH}_3\text{O}_{\text{ad}} + \text{H}_3\text{O}_{\text{aq}}^+ + \text{e}_{\text{metal}}^-$) was found to control the dehydrogenation energetics since the homolytic pathway ($\text{CH}_3\text{OH}_{\text{ad}} \rightarrow \text{CH}_3\text{O}_{\text{ad}} + \text{H}_{\text{ad}}$) was 43 kJ/mol more endothermic.⁷⁴ Using the same approach, Zope et al.⁷⁵ studied the mechanism of selective oxidation of ethanol to acetic acid on Pt(111) and Au(111). They observed that for some reactions involving a hydroxide intermediate or a water molecule, the hydroxide or water actually originates from the surrounding water network. The effect of explicit water molecules on reaction energies and activation barriers can be strongly correlated to the interactions (that is, hydrogen bonding ability) of the reactants, products, and transition states with the surrounding water molecules.

The role of water becomes more significant for reactions when there is a change in the dipole orientation between the two states as this possibly leads to a change in the number of hydrogen bonds and/or a change in polarizability, both of which can stabilize one state over the other resulting in a marked increase or decrease in the activation barrier.⁷⁶

2.5. Force Fields for Molecular Dynamics Simulations

Molecular dynamics simulations of aqueous solutions with explicit water molecules are carried out using classical water models, of which 3-site SPC and TIP3P, and 4-site TIP4P models are most popular. The 3-site models have three interaction sites corresponding to the actual atoms of a water molecule. The 4-site TIP4P model has an additional massless charged site that improves the electrostatic distribution around the water molecule. All these models have been parameterized to reproduce experimental

data for energy, density, and radial density profiles near 25 °C and 1 atm. We have chosen the TIP3P model since its geometric parameters more closely represent the geometry of a water molecule than those of SPC model.⁷⁷

The structure of pure liquid ethylene glycol has been extensively studied using a united-atom approach.⁷⁸⁻⁷⁹ Six interaction sites are considered per EG molecule; CH₂ groups are treated as single interaction sites with their centers located at the position of the carbon atoms. Hydrogen atoms of this united group are not explicitly considered; they are taken into account implicitly in the force field parameters.⁸⁰⁻⁸¹ Molecular dynamics simulations of pure liquid and aqueous mixtures of ethylene glycol with a number of polarizable and nonpolarizable force fields have shown that polarization effects might play an important role in correctly describing attractive interactions between EG and water co-solvent molecules.⁸² However, considering that the ratio of the number of EG-derived species (1) to the number of TIP3P water molecules (~2500) is very small in our model, these polarization effects will likely be negligible or very similar between reactant and product states and a non-polarizable OPLS-AA force field⁸² should suffice for these simulations.

Water adsorption on platinum surfaces preferentially occurs on atop sites with water molecules being nearly parallel to the surface.^{73, 83} Special functional forms are required in order to correctly describe the Pt–water interface. The most commonly used potential function in this respect was proposed by Spohr and Heinzinger⁸⁴ by fitting a set of exponential functions to extended Hückel calculations of a water molecule in different orientations over platinum:

$$\begin{aligned}\phi_{\text{H}_2\text{O-Pt}} &= \phi_{\text{O-Pt}} + \phi_{\text{H(1)-Pt}} + \phi_{\text{H(2)-Pt}} \\ \phi_{\text{O-Pt}} &= \left[1894.2e^{-1.1004r} - 1886.3e^{-1.0996r} \right] f + 10^6 e^{-5.3568r} (1-f) \\ \phi_{\text{H-Pt}} &= 1.7142e^{-1.2777r} \\ f &= e^{-0.5208\rho^2}\end{aligned}\quad \dots(2.7)$$

The energy is given in units of 10^{-19} J and r and ρ are in Å. The interatomic distances are denoted by r , whereas ρ is the length of the projection of the distance vector onto the surface plane. The Spohr–Heinzinger model correctly describes the adsorption site and adsorption energy of water on platinum and has recently been successfully used for thermal conductivity⁸⁵ and latent heat⁸⁶ enhancement studies.

2.6. References

1. Wyman, C. E. *Annu. Rev. Energy Env.* **1999**, *24*, 189–226.
2. Huber, G. W.; Iborra, S.; Corma, A. *Chem. Rev.* **2006**, *106*, 4044–4098.
3. Huber, G. W.; Dumesic, J. A. *Catal. Today* **2006**, *111*, 119–132.
4. Sun, Y.; Cheng, J. Y. *Bioresour. Technol.* **2002**, *83*, 1–11.
5. Mosier, N.; Wyman, C.; Dale, B.; Elander, R.; Lee, Y. Y.; Holtzapple, M.; Ladisch, M. *Bioresour. Technol.* **2005**, *96*, 673–686.
6. Tanksale, A.; Beltramini, J. N.; Lu, G. M. *Renewable Sustainable Energy Rev.* **2010**, *14*, 166–182.
7. Chheda, J. N.; Huber, G. W.; Dumesic, J. A. *Angew. Chem., Int. Ed.* **2007**, *46*, 7164–7183.
8. Kirilin, A.; Warna, J.; Tokarev, A.; Murzin, D. Y. *Ind. Eng. Chem. Res.* **2014**, *53*, 4580–4588.
9. Cortright, R. D.; Davda, R. R.; Dumesic, J. A. *Nature* **2002**, *418*, 964–967.
10. Davda, R. R.; Dumesic, J. A. *Angew. Chem., Int. Ed.* **2003**, *42*, 4068–4071.
11. Huber, G. W.; Shabaker, J. W.; Dumesic, J. A. *Science* **2003**, *300*, 2075–2077.
12. Davda, R. R.; Dumesic, J. A. *Chem. Commun.* **2004**, 36–37.
13. Huber, G. W.; Cortright, R. D.; Dumesic, J. A. *Angew. Chem., Int. Ed.* **2004**, *43*, 1549–1551.
14. Huber, G. W.; Chheda, J. N.; Barrett, C. J.; Dumesic, J. A. *Science* **2005**, *308*, 1446–1450.
15. Vardon, D. R.; Sharma, B. K.; Jaramillo, H.; Kim, D.; Choe, J. K.; Ciesielski, P. N.; Strathmann, T. J. *Green Chem.* **2014**, *16*, 1507–1520.
16. Chheda, J. N.; Dumesic, J. A. *Catal. Today* **2007**, *123*, 59–70.
17. Lin, Y. C.; Huber, G. W. *Energy Environ. Sci.* **2009**, *2*, 68–80.
18. Davda, R. R.; Shabaker, J. W.; Huber, G. W.; Cortright, R. D.; Dumesic, J. A. *Appl. Catal., B* **2003**, *43*, 13–26.
19. Moreau, C.; Durand, R.; Duhamet, J.; Rivalier, P. *J. Carbohydr. Chem.* **1997**, *16*, 709–714.
20. Torget, R. W.; Kim, J. S.; Lee, Y. Y. *Ind. Eng. Chem. Res.* **2000**, *39*, 2817–2825.

21. Karimi, K.; Kheradmandinia, S.; Taherzadeh, M. J. *Biomass Bioenergy* **2006**, *30*, 247–253.
22. Nagamori, M.; Funazukuri, T. *J. Chem. Technol. Biotechnol.* **2004**, *79*, 229–233.
23. Kuster, B. F. M. *Starch* **1990**, *42*, 314–321.
24. Moreau, C.; Durand, R.; Razigade, S.; Duhamet, J.; Faugeras, P.; Rivalier, P.; Ros, P.; Avignon, G. *Appl. Catal., A* **1996**, *145*, 211–224.
25. Moreau, C.; Belgacem, M. N.; Gandini, A. *Top. Catal.* **2004**, *27*, 11–30.
26. James, O. O.; Maity, S.; Usman, L. A.; Ajanaku, K. O.; Ajani, O. O.; Siyanbola, T. O.; Sahu, S.; Chaubey, R. *Energy Environ. Sci.* **2010**, *3*, 1833–1850.
27. Huber, G. W. *Breaking the Chemical and Engineering Barriers to Lignocellulosic Biofuels: Next Generation Hydrocarbon Biorefineries*; University of Massachusetts Amherst: 2008.
28. Barrett, C. J.; Chheda, J. N.; Huber, G. W.; Dumesic, J. A. *Appl. Catal., B* **2006**, *66*, 111–118.
29. Maris, E. P.; Davis, R. J. *J. Catal.* **2007**, *249*, 328–337.
30. Maris, E. P.; Ketchie, W. C.; Murayama, M.; Davis, R. J. *J. Catal.* **2007**, *251*, 281–294.
31. Wang, K. Y.; Hawley, M. C.; Furney, T. D. *Ind. Eng. Chem. Res.* **1995**, *34*, 3766–3770.
32. Mavrikakis, M.; Barteau, M. A. *J. Mol. Catal. A: Chem.* **1998**, *131*, 135–147.
33. Gootzen, J. F. E.; Visscher, W.; vanVeen, J. A. R. *Langmuir* **1996**, *12*, 5076–5082.
34. Gootzen, J. F. E.; Wonders, A. H.; Visscher, W.; vanVeen, J. A. R. *Langmuir* **1997**, *13*, 1659–1667.
35. Brown, N. F.; Barteau, M. A. *J. Phys. Chem.* **1994**, *98*, 12737–12745.
36. Vannice, M. A. *J. Catal.* **1977**, *50*, 228–236.
37. Grenoble, D. C.; Estadt, M. M.; Ollis, D. F. *J. Catal.* **1981**, *67*, 90–102.
38. Gutsche, C. D.; Redmore, D.; Buriks, R. S.; Nowotny, K.; Grassner, H.; Armbrust, C. W. *J. Am. Chem. Soc.* **1967**, *89*, 1235–1245.
39. Rao, K. K.; Gravelle, M.; Valente, J. S.; Figueras, F. *J. Catal.* **1998**, *173*, 115–121.
40. Choudary, B. M.; Kantam, M. L.; Sreekanth, P.; Bandopadhyay, T.; Figueras, F.; Tuel, A. *J. Mol. Catal. A: Chem.* **1999**, *142*, 361–365.
41. Climent, M. J.; Corma, A.; Iborra, S.; Epping, K.; Velty, A. *J. Catal.* **2004**, *225*, 316–326.
42. Kunkes, E. L.; Simonetti, D. A.; West, R. M.; Serrano-Ruiz, J. C.; Gartner, C. A.; Dumesic, J. A. *Science* **2008**, *322*, 417–421.
43. West, R. M.; Liu, Z. Y.; Peter, M.; Dumesic, J. A. *ChemSusChem* **2008**, *1*, 417–424.
44. West, R. M.; Tucker, M. H.; Braden, D. J.; Dumesic, J. A. *Catal. Commun.* **2009**, *10*, 1743–1746.
45. West, R. M.; Braden, D. J.; Dumesic, J. A. *J. Catal.* **2009**, *262*, 134–143.
46. Shabaker, J. W.; Dumesic, J. A. *Ind. Eng. Chem. Res.* **2004**, *43*, 3105–3112.
47. Shabaker, J. W.; Huber, G. W.; Davda, R. R.; Cortright, R. D.; Dumesic, J. A. *Catal. Lett.* **2003**, *88*, 1–8.
48. Davda, R. R.; Shabaker, J. W.; Huber, G. W.; Cortright, R. D.; Dumesic, J. A. *Appl. Catal., B* **2005**, *56*, 171–186.
49. Alcalá, R.; Mavrikakis, M.; Dumesic, J. A. *J. Catal.* **2003**, *218*, 178–190.
50. Greeley, J.; Mavrikakis, M. *J. Am. Chem. Soc.* **2004**, *126*, 3910–3919.
51. Vesselli, E.; Coslovich, G.; Comelli, G.; Rosei, R. *J. Phys.: Condens. Matter* **2005**, *17*, 6139–6148.

52. Cao, D.; Lu, G. Q.; Wieckowski, A.; Wasileski, S. A.; Neurock, M. *J. Phys. Chem. B* **2005**, *109*, 11622–11633.
53. Skoplyak, O.; Barteau, M. A.; Chen, J. G. G. *J. Phys. Chem. B* **2006**, *110*, 1686–1694.
54. Kandoi, S.; Greeley, J.; Sanchez-Castillo, M. A.; Evans, S. T.; Gokhale, A. A.; Dumesic, J. A.; Mavrikakis, M. *Top. Catal.* **2006**, *37*, 17–28.
55. Wang, H. F.; Liu, Z. P. *J. Am. Chem. Soc.* **2008**, *130*, 10996–11004.
56. Skoplyak, O.; Barteau, M. A.; Chen, J. G. G. *Surf. Sci.* **2008**, *602*, 3578–3587.
57. Skoplyak, O.; Menning, C. A.; Barteau, M. A.; Chen, J. G. G. *Top. Catal.* **2008**, *51*, 49–59.
58. Ferrin, P.; Simonetti, D.; Kandoi, S.; Kunkes, E.; Dumesic, J. A.; Norskov, J. K.; Mavrikakis, M. *J. Am. Chem. Soc.* **2009**, *131*, 5809–5815.
59. Saliccioli, M.; Chen, Y.; Vlachos, D. G. *J. Phys. Chem. C* **2010**, *114*, 20155–20166.
60. Skoplyak, O.; Barteau, M. A.; Chen, J. G. *ChemSusChem* **2008**, *1*, 524–526.
61. Norskov, J. K.; Bligaard, T.; Logadottir, A.; Bahn, S.; Hansen, L. B.; Bollinger, M.; Benggaard, H.; Hammer, B.; Sljivancanin, Z.; Mavrikakis, M.; Xu, Y.; Dahl, S.; Jacobsen, C. J. H. *J. Catal.* **2002**, *209*, 275–278.
62. Jones, G.; Bligaard, T.; Abild-Pedersen, F.; Norskov, J. K. *J. Phys.: Condens. Matter* **2008**, *20*, 064239.
63. Saliccioli, M.; Yu, W. T.; Barteau, M. A.; Chen, J. G. G.; Vlachos, D. G. *J. Am. Chem. Soc.* **2011**, *133*, 7996–8004.
64. Saliccioli, M.; Vlachos, D. G. *ACS Catal.* **2011**, *1*, 1246–1256.
65. Saliccioli, M.; Vlachos, D. G. *ACS Catal.* **2012**, *2*, 306–306 Erratum.
66. Kunkes, E. L.; Simonetti, D. A.; Dumesic, J. A.; Pyrz, W. D.; Murillo, L. E.; Chen, J. G. G.; Buttrey, D. J. *J. Catal.* **2008**, *260*, 164–177.
67. Kandoi, S.; Greeley, J.; Simonetti, D.; Shabaker, J.; Dumesic, J. A.; Mavrikakis, M. *J. Phys. Chem. C* **2011**, *115*, 961–971.
68. Shabaker, J. W.; Davda, R. R.; Huber, G. W.; Cortright, R. D.; Dumesic, J. A. *J. Catal.* **2003**, *215*, 344–352.
69. Jacob, T.; Goddard, W. A. *ChemPhysChem* **2006**, *7*, 992–1005.
70. Wang, H. F.; Liu, Z. P. *J. Phys. Chem. C* **2009**, *113*, 17502–17508.
71. Toney, M. F.; Howard, J. N.; Richer, J.; Borges, G. L.; Gordon, J. G.; Melroy, O. R.; Wiesler, D. G.; Yee, D.; Sorensen, L. B. *Nature* **1994**, *368*, 444–446.
72. Henderson, M. A. *Surf. Sci. Rep.* **2002**, *46*, 1–308.
73. Hodgson, A.; Haq, S. *Surf. Sci. Rep.* **2009**, *64*, 381–451.
74. Neurock, M.; Wasileski, S. A.; Mei, D. *Chem. Eng. Sci.* **2004**, *59*, 4703–4714.
75. Zope, B. N.; Hibbitts, D. D.; Neurock, M.; Davis, R. J. *Science* **2010**, *330*, 74–78.
76. Rossmesl, J.; Logadottir, A.; Norskov, J. K. *Chem. Phys.* **2005**, *319*, 178–184.
77. Jorgensen, W. L.; Chandrasekhar, J.; Madura, J. D.; Impey, R. W.; Klein, M. L. *J. Chem. Phys.* **1983**, *79*, 926–935.
78. Saiz, L.; Padro, J. A.; Guardia, E. *J. Chem. Phys.* **2001**, *114*, 3187–3199.
79. Gubskaya, A. V.; Kusalik, P. G. *J. Phys. Chem. A* **2004**, *108*, 7151–7164.
80. Jorgensen, W. L. *J. Phys. Chem.* **1986**, *90*, 1276–1284.
81. Kony, D.; Damm, W.; Stoll, S.; van Gunsteren, W. F. *J. Comput. Chem.* **2002**, *23*, 1416–1429.
82. Geerke, D. P.; Van Gunsteren, W. F. *Mol. Phys.* **2007**, *105*, 1861–1881.

83. Meng, S.; Wang, E. G.; Gao, S. W. *Phys. Rev. B* **2004**, *69*, 195404.
84. Spohr, E. *J. Phys. Chem.* **1989**, *93*, 6171–6180.
85. Sankar, N.; Mathew, N.; Sobhan, C. B. *Int. Commun. Heat Mass Transfer* **2008**, *35*, 867–872.
86. Ameen, M. M.; Prabhul, K.; Sivakumar, G.; Abraham, P. P.; Jayadeep, U. B.; Sobhan, C. B. *Int. J. Thermophys.* **2010**, *31*, 1131–1144.

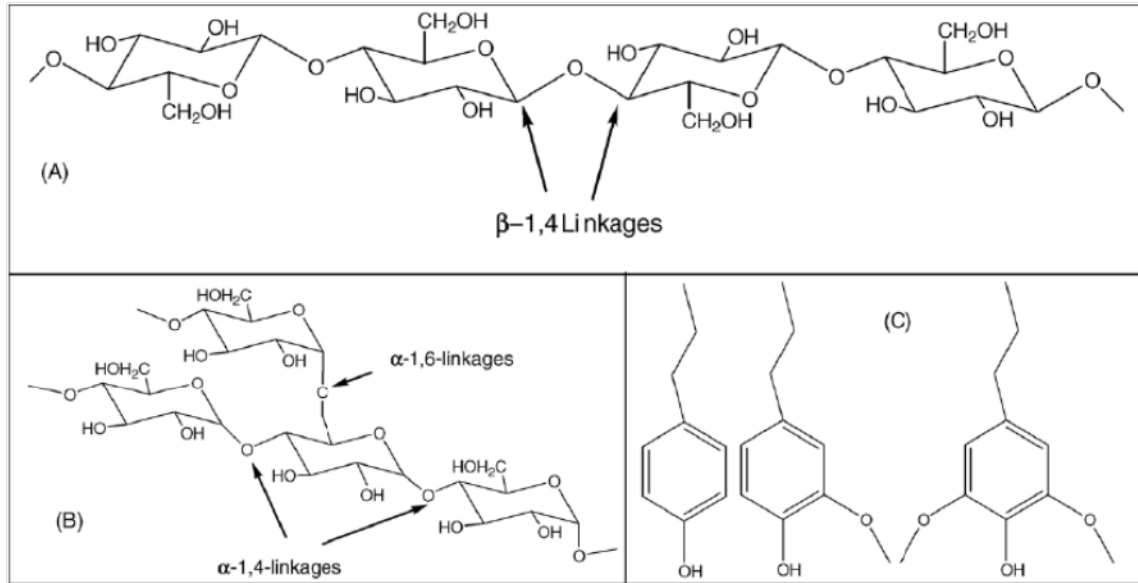


Figure 2.1. Chemical structure of biomass-derived compounds including: (A) cellulose with β -1,4 glycoside linkages, (B) starches with α -1,4 and α -1,6 glycoside linkages, and (C) structural monomer units of lignin.³

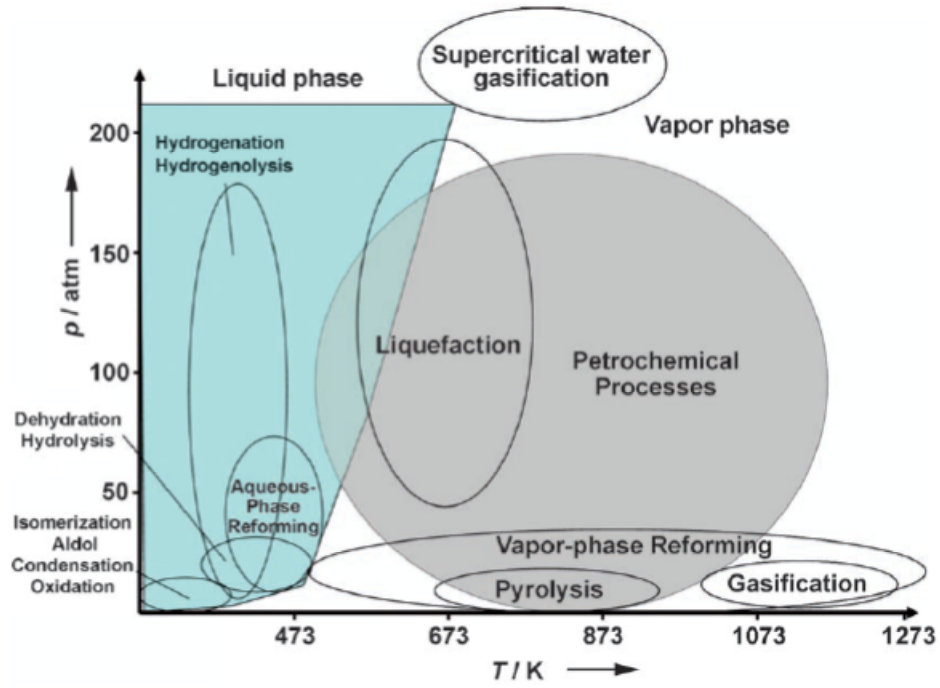


Figure 2.2. Process conditions for the catalytic conversion of petroleum and biomass feedstocks.⁷

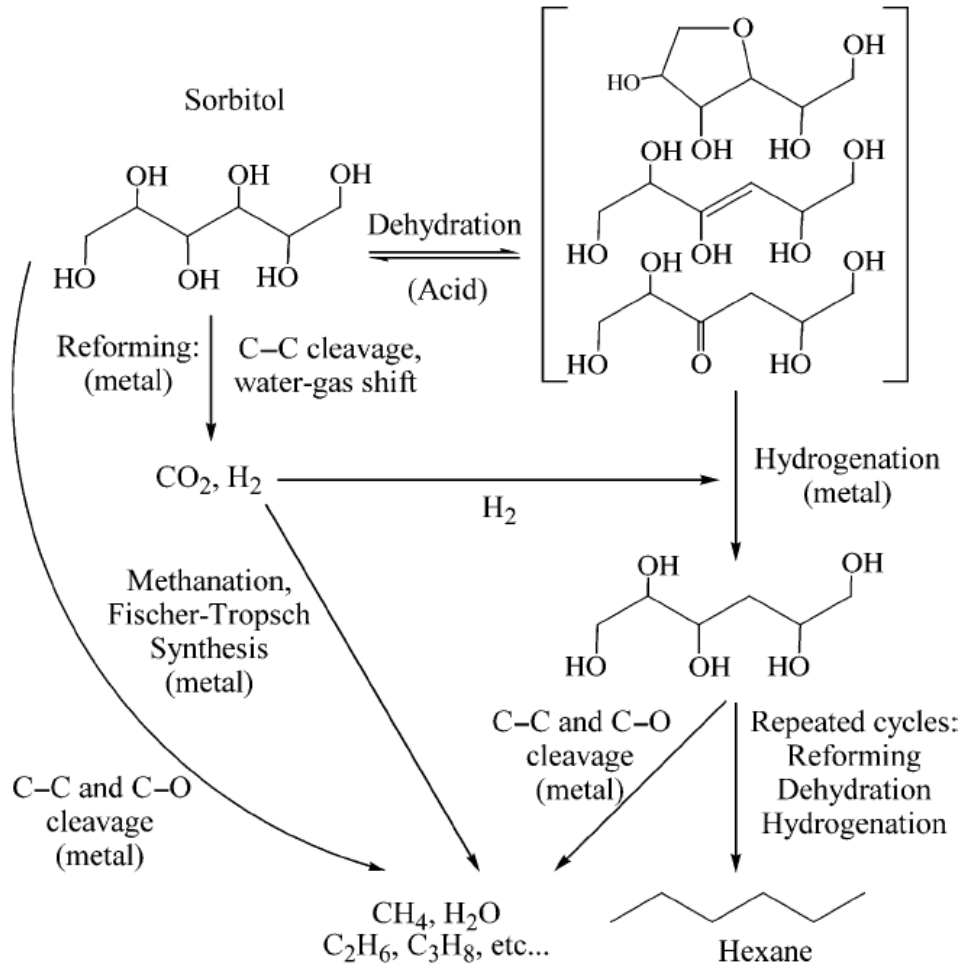


Figure 2.3. Reaction pathways for the production of alkanes from sorbitol over multifunctional catalysts containing metal and acid sites.¹³

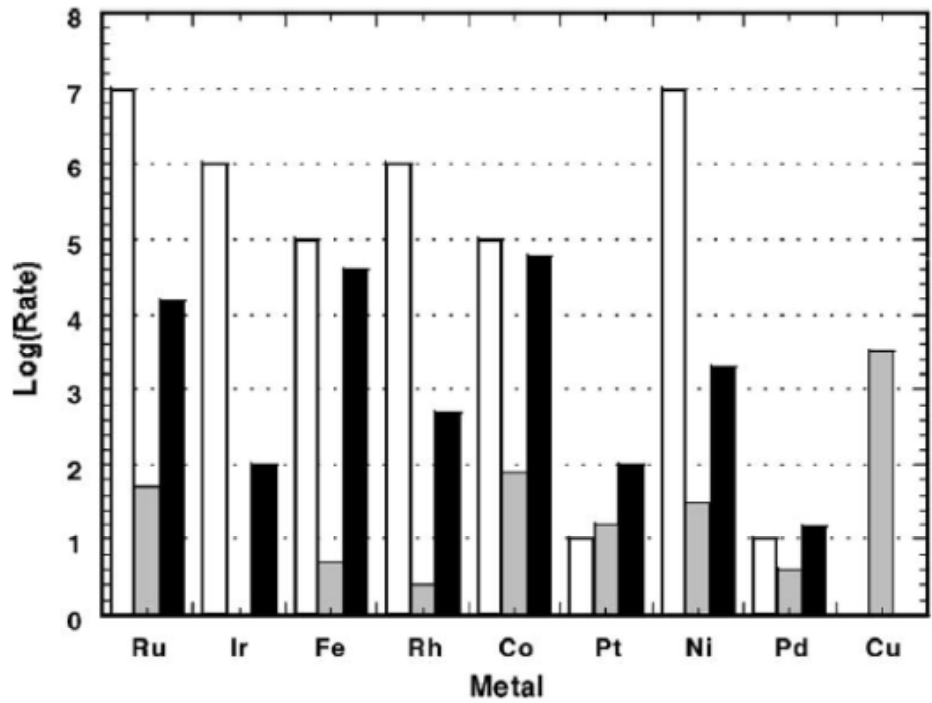


Figure 2.4. Relative rates of C–C bond breaking reaction (white), water-gas shift reaction (grey), and methanation reaction (black). The rate of a particular reaction can be compared for different metals; however, for a specific metal, the absolute rates of the three reactions cannot be compared relative to each other.¹⁸

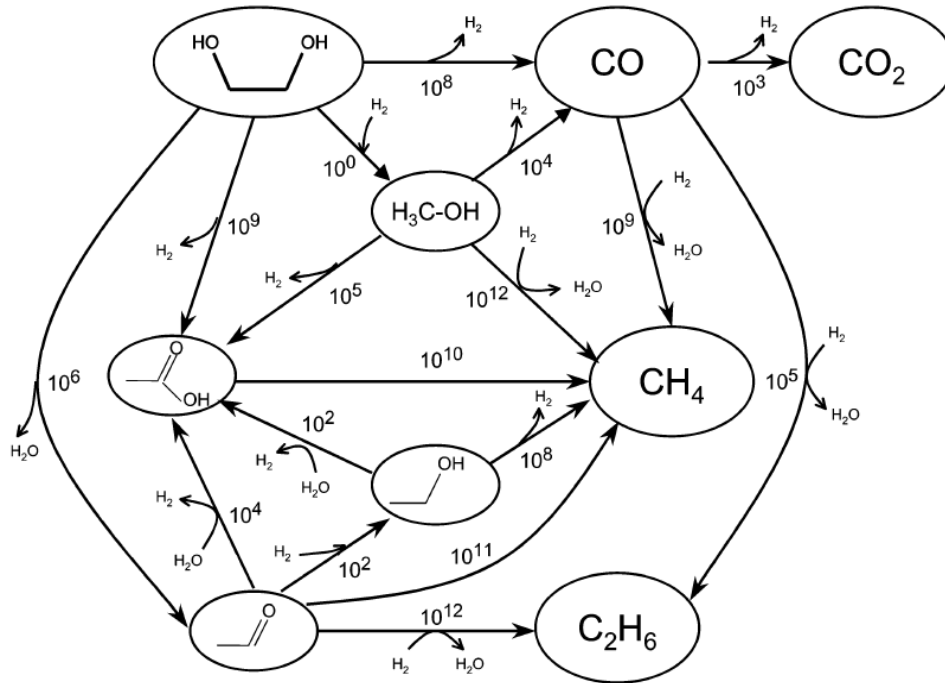


Figure 2.5. Thermodynamic pathways among stable compounds in ethylene glycol reforming. Each reaction is defined in its thermodynamically favorable direction, and equilibrium constants are listed per mole of reactant at 498 K.⁴⁶

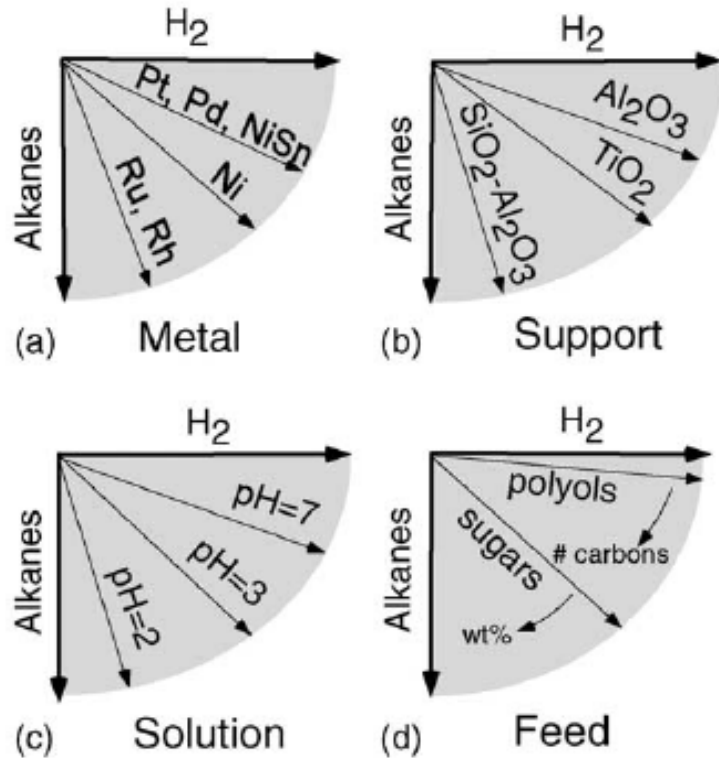


Figure 2.6. Factors controlling the selectivity of aqueous-phase reforming process.⁴⁸

CHAPTER 3

COMPUTATIONAL METHODS

3.1. Density Functional Theory

Computational studies based on a quantum mechanical (QM) description of the interactions between electrons and atomic nuclei have become an important tool for obtaining qualitative and, in many cases, quantitative insights into the structural and electronic properties of catalyst nanoparticles and their roles in the reaction mechanisms. Fundamental to these calculations is the time-independent Schrödinger equation:

$$H\Psi = E\Psi \quad \dots(3.1)$$

where H is the Hamiltonian operator, E is the total energy of the system, and Ψ is the corresponding wavefunction. The solution of this equation yields the energy eigenvalues and probability distribution for all particles in the system.

Analytical solution of Equation (3.1) is not possible for most systems of practical interest and certain simplifying assumptions must be made. The electronic and nuclear degrees of freedom are separated using the Born–Oppenheimer approximation. This simplification assumes that the electronic relaxation is instantaneous with respect to the movement of the nuclei. The electronic energy is then calculated for fixed configurations of nuclei in a sea of electrons. The electronic Schrödinger equation is

$$(H_{el} + V_N)\Psi_{el} = E_{el}\Psi_{el} \quad \dots(3.2)$$

where the subscript el emphasizes the use of the Born–Openheimer approximation. V_N is the nuclear–nuclear repulsion energy and is a constant for a fixed configuration of nuclear coordinates.

Density functional theory (DFT) assumes that the ground state electronic energy (E) of an atom or molecule can be expressed exactly as a function of the electron density (ρ) of the molecule.¹⁻² The term “functional” refers to a function of a function. That is, the electronic energy is a function of electron density which is a function of electronic coordinates. In DFT formalism, the total electronic energy is expressed as

$$E = T + V_{\text{nucl}} + V_{\text{rep}} + E_{\text{xc}} \quad \dots(3.3)$$

The four terms on the right side of Equation (3.3) are electronic kinetic energy (T), electron–nuclei interaction (V_{nucl}), inter-electronic Coulombic repulsion (V_{rep}), and exchange-correlation energy (E_{xc}). The electronic kinetic energy is typically calculated using the wavefunction whereas the electron–nuclei interaction and electron–electron repulsion terms are expressed as functionals of electron density.³

$$T = -\frac{1}{2} \sum_i \int \psi_i \nabla^2 \psi_i d\tau; \quad V_{\text{nucl}} = -\sum_{\alpha} \int \frac{Z_{\alpha} \rho(1)}{r_{1\alpha}} d\tau_1; \quad V_{\text{rep}} = \frac{1}{2} \iint \frac{\rho(1)\rho(2)}{r_{12}} d\tau_1 d\tau_2 \quad \dots(3.4)$$

There is no known exact expression for E_{xc} . However, several approximate expressions have been developed leading to a variety of DFT methods. The simplest of these approximations is the local density approximation (LDA) which estimates E_{xc} from local electron density only. The quality of DFT results can be substantially improved by additionally taking into account the gradient of the electron density, an approach known as generalized gradient approximation (GGA). GGA functionals have been successful for

predicting structures and electronic properties of molecules on metallic surfaces that are significantly better than the conventional Hartree–Fock theory.³

Because the core electrons are present in the inner shells and do not actively participate in bond breaking and forming processes, it is not necessary to explicitly account for their effect in every cycle of the self-consistent field calculations. In the frozen core approximation, one-electron wavefunctions for the core electrons are fixed at a reference condition (that is, for an isolated atom) and are not reevaluated during the DFT calculations. This approximation significantly reduces the computational cost by reducing the size of the variational problem at hand.

Two modes of DFT calculations are used in this study. For an isolated molecule (or a finite metal cluster), the electron density at an infinite distance from the system must fall to zero. Nonperiodic DFT calculations using Gaussian-type atomic orbitals (basis sets) are sufficient for this purpose. To account for long range metal interactions, extended surfaces must be modeled. This necessitates the use of a slab model with periodic boundary conditions and planewave basis sets.

3.2. Conductor-Like Screening Model (COSMO)

The conductor-like screening model (COSMO) is a continuum solvation model where the solvent is modeled as a homogeneous medium characterized by an appropriate dielectric constant (ϵ), and the solute is placed in carefully constructed cavities within this continuum.⁴ QM charge distribution of the solute polarizes the surrounding dielectric medium. The response of the polarized solvent is expressed in terms of screening charges on the surface of the cavity.⁵ Assuming an electrostatically ideal solvent ($\epsilon = \infty$), the

boundary condition of vanishing electrostatic potential for a conductor ($\Phi_{\text{total}} = 0$) is used. The solute potential (Φ_{solute}) and the vector of screening charges (q) must satisfy overall charge neutrality of the system.

$$\Phi_{\text{total}} = \Phi_{\text{solute}} + Aq = 0; \quad q = -A^{-1}\Phi_{\text{solute}} \quad \dots(3.5)$$

where A is the Coulomb matrix of the screening charge interactions.⁶⁻⁷ The finite permittivity of real solvents is taken into account by scaling the screening charges.

$$f(\epsilon) = \frac{\epsilon - 1}{\epsilon + 0.5}; \quad q^* = q \cdot f(\epsilon) \quad \dots(3.6)$$

This reaction field is included as electrostatic potential (ESP) in every cycle of the self-consistent field calculations allowing a simultaneous variational optimization of both the molecular orbitals and the screening charges. The total free energy of the solvated molecule is the sum of the energy of the isolated system calculated with the solvated wavefunction and the dielectric energy.⁶

$$E = E(\Psi_{\text{solv}}) + E_{\text{diel}} \quad \dots(3.7)$$

3.3. Periodic Electrostatic Embedded Cluster Method (PEECM)

The periodic electrostatic embedded cluster method provides a QM/MM functionality of embedding a finite QM cluster in a periodic, infinite array of point charges.⁸ The system is divided into an inner part, which is treated quantum mechanically, and an outer part which describes the environment of the QM cluster in terms of effective core potentials (ECPs) or simply point charges. This approach is different from periodic planewave QM calculations (section 3.1) where the whole system as well as its periodic images are treated quantum mechanically. In PEECM, the Coulombic interaction energy from the periodic field of point charges is evaluated using

the periodic fast multipole method.⁹ This approach was originally developed for QM calculations involving localized defects in ionic crystals.⁸ In this study, we use water conformations generated from molecular dynamics simulations as the field of point charges.

3.4. Microkinetic Modeling

Mean-field microkinetic modeling provides an efficient mechanism for analysis of experimental and computational data to obtain insights into the reaction mechanism and the nature of the active site under reaction conditions. The catalytic process is assumed to take place through a sequence of elementary reactions. The net rate of a reversible elementary reaction i is calculated using

$$r_i = k_{f,i} \prod_{j=1, n_j < 0}^{j=N} C_j^{-n_j} - k_{r,i} \prod_{j=1, n_j > 0}^{j=N} C_j^{n_j} \quad \dots(3.8)$$

where $k_{f,i}$ and $k_{r,i}$ are the forward and reverse reaction rate constants, respectively. Index j loops over all N species involved in the reaction, and the corresponding concentration C_j equals either a fractional surface coverage (θ_j) or a gas-phase partial pressure (P_j). The stoichiometric coefficient n_j is negative for reactants and positive for products. For all surface reactions, forward rate constants can be calculated using harmonic transition state theory.¹⁰

$$k_{f,i} = \frac{\gamma k_B T}{h} \exp\left(\frac{-\Delta G_i^\ddagger}{k_B T}\right) \quad \dots(3.9)$$

Here, ΔG_i^\ddagger is the free energy of activation, T is the absolute temperature, γ is the transmission coefficient, and k_B and h are respectively the Boltzmann and Planck

constants. Zero-point energies and (harmonic) vibrational partition functions are calculated using vibrational frequencies (ν_i) derived from QM calculations.

$$E_{zpv} = \sum_i \frac{h\nu_i}{2}, \quad q_{vib} = \prod_i \left[1 - \exp\left(\frac{-h\nu_i}{k_B T}\right) \right]^{-1} \quad \dots(3.10)$$

Adsorption is generally assumed to be a nonactivated process and collision theory is used to calculate the forward rate constants.

$$k_{f,i} = \frac{S\sigma}{N\sqrt{2\pi M_i k_B T}} \quad \dots(3.11)$$

Here, N/S is the number of catalytic sites per unit surface area, σ is the sticking probability, and M_i is the molecular weight of the adsorbate. To ensure thermodynamic consistency, reverse rate constants are calculated from the thermodynamic equilibrium constants (K_{eq}).

$$K_{eq,i} = \exp\left(\frac{-\Delta G_i}{k_B T}\right); \quad k_{r,i} = \frac{k_{f,i}}{K_{eq,i}} \quad \dots(3.12)$$

where ΔG_i is the Gibbs free energy of reaction. At steady state, the fractional coverage of a surface intermediate is given by

$$\frac{d\theta_j}{dt} = \sum_i \nu_{j,i} r_i = 0 \quad \dots(3.13)$$

where index i loops over all reactions. In addition, the total number of sites is conserved.

$$\sum_j n_j \theta_j = 1 \quad \dots(3.14)$$

Equations (3.13) and (3.14) form a set of differential algebraic equations that must be iteratively solved to obtain the fractional coverages of all surface intermediates. The same converged solution yields the rates of individual elementary steps following Equation

(3.8). This information can be used to identify the dominant reaction pathway and to calculate the contribution of various pathways to the overall turnover frequency.

For comparison with experimental data, microkinetic modeling can be used for prediction of general kinetic trends including apparent activation energy (E_{app}) and reaction orders (α_i) with respect to various reactants and products:

$$E_{app} = -k_B \left[\frac{\partial \ln(r)}{\partial \left(\frac{1}{T}\right)} \right]_{P_i} ; \quad \alpha_i = \left[\frac{\partial \ln(r)}{\partial \ln(P_i)} \right]_{T, P_{j \neq i}} \quad \dots(3.15)$$

Also, Campbell's degree of rate control¹¹ and degree of thermodynamic rate control¹²⁻¹³ analyses can be used to identify rate-controlling elementary steps and surface intermediates.

$$X_{RC,i} = \left[\frac{\partial \ln(r)}{\partial \left(\frac{-G_i^{0,TS}}{k_B T}\right)} \right]_{G_{j \neq i}^{0,TS}, G_m^0} ; \quad X_{TRC,n} = \left[\frac{\partial \ln(r)}{\partial \left(\frac{-G_n^0}{k_B T}\right)} \right]_{G_{m \neq n}^0, G_i^{0,TS}} \quad \dots(3.16)$$

Here, $X_{RC,i}$ is the degree of rate control for elementary reaction i , $X_{TRC,n}$ is the degree of thermodynamic rate control for adsorbate n , r is the overall rate of reaction, $G_i^{0,TS}$ is the free energy of transitions state i , and G_n^0 is the free energy of adsorbate n .

3.5. References

1. Hohenberg, P.; Kohn, W. *Phys. Rev.* **1964**, *136*, B864.
2. Kohn, W.; Sham, L. J. *Phys. Rev.* **1965**, *140*, A1133.
3. Ratner, M. A.; Schatz, G. C. *Introduction to Quantum Mechanics in Chemistry*. Prentice Hall: Upper Saddle River, NJ, 2001.
4. Klamt, A.; Schuurmann, G. *J. Chem. Soc., Perkin Trans. 2* **1993**, 799–805.
5. Klamt, A.; Jonas, V. *J. Chem. Phys.* **1996**, *105*, 9972–9981.
6. TURBOMOLE V6.4 2012, a development of University of Karlsruhe and Forschungszentrum Karlsruhe GmbH, 1989–2007, TURBOMOLE GmbH, since 2007.
7. Schafer, A.; Klamt, A.; Sattel, D.; Lohrenz, J. C. W.; Eckert, F. *Phys. Chem. Chem. Phys.* **2000**, *2*, 2187–2193.

8. Burow, A. M.; Sierka, M.; Dobler, J.; Sauer, J. *J. Chem. Phys.* **2009**, *130*, 174710.
9. Kudin, K. N.; Scuseria, G. E. *Chem. Phys. Lett.* **1998**, *283*, 61–68.
10. Pechukas, P. *Annu. Rev. Phys. Chem.* **1981**, *32*, 159–177.
11. Campbell, C. T. *J. Catal.* **2001**, *204*, 520–524.
12. Stegelmann, C.; Andreasen, A.; Campbell, C. T. *J. Am. Chem. Soc.* **2009**, *131*, 8077–8082.
13. Stegelmann, C.; Andreasen, A.; Campbell, C. T. *J. Am. Chem. Soc.* **2009**, *131*, 13563–13563
Erratum.

CHAPTER 4

NEW IMPLICIT SOLVATION SCHEME FOR SOLID SURFACES

4.1. Summary

It is shown that the effect of water on the bonding characteristics of transition metal surfaces with adsorbates is short ranged. As a result, adsorption energies in water can be evaluated by a combination of planewave density functional theory calculations in vacuum and properly chosen cluster model calculations with and without an implicit solvation model. The scheme is demonstrated for a model C–C cleavage reaction on Pt (111) and for predicting CO frequency shifts on Pd and Pt due to water. We conclude that these shifts originate from water–metal interactions and can be explained by changes in π back-donation. Overall, the results demonstrate that the proposed methodology represents a highly efficient computational approach for approximating the effect of solvents on elementary reaction steps occurring at solid–liquid interfaces of heterogeneous catalysts.

4.2. Introduction

Computational investigations of chemical reactions at solid–liquid interfaces pose a unique challenge of accurately yet efficiently accounting for the effect of the liquid-phase environment. Liquid molecules can affect the activity and selectivity of a catalyst

Adapted with permission from Faheem, M.; Suthirakun, S.; Heyden, A. *J. Phys. Chem. C* **2012**, *116*, 22458–22462. © 2012 American Chemical Society.

by stabilizing or destabilizing adsorbed intermediates and transition states¹ and by providing low-energy pathways for reactions, for example, for proton transfer between neighboring active sites.² Free energy differences and rates of elementary reaction steps occurring at solid–liquid interfaces are often very different from the same processes occurring at solid–gas interfaces. To correctly account for the effect of a liquid phase on reaction rates, the dynamic fluctuations in the complex liquid and the long range electrostatic interactions of the liquid molecules must be considered, requiring the simulation of a large number of liquid molecules over a (computationally) long time period. As a result, the use of *ab initio* molecular dynamics (AIMD) approaches³ for systematic investigations of such processes becomes for the foreseeable future computationally prohibitive.

A common procedure for modeling liquid water at solid–liquid interfaces consists of optimizing a hexagonally closed-packed ice-like structure at the metal interface before replacing one of the water molecules with the reactant species.⁴⁻⁵ Although significantly faster than AIMD, this approach includes no or very limited sampling of the water configuration space and is error-prone for relatively large adsorbates where it is difficult to identify a meaningful initial configuration of the water molecules. Alternatively, Jacob and Goddard⁶ have pioneered the use of implicit continuum solvation models⁷⁻⁹ on large metal clusters of (111) surface shape. While continuum solvation models cannot accurately describe site-specific interactions between the adsorbates and the surrounding solvent molecules, they are computationally fast and reasonably accurate for computing free energies in solution. Furthermore, solvents and reaction conditions such as temperature can easily be changed with modern implicit solvation models developed for

molecular systems.¹⁰ Unfortunately, relatively large metal clusters must be selected to describe the long range metal interactions and to overcome unwanted boundary effects⁶ due to the finite size of the cluster.¹¹ Similarly, implicit solvation models have been developed for periodic systems. However, most implementations only consider electrostatic effects although nonelectrostatic contributions are crucial for obtaining accurate solvation free energies.¹² Considering furthermore that the implementation of smooth gradients of free energies has been progressing slowly in plane wave density functional theory (DFT) codes,¹³⁻¹⁵ it would be very beneficial if current nonperiodic implicit solvation models could be used to describe the effect of solvents on processes occurring at “periodic” solid–liquid interfaces.

In this paper, we propose a simple but potentially very powerful new approach for modeling reactions at solid–liquid interfaces with implicit solvation models, which we call implicit solvation model for solid surfaces (iSMS). The objective of this theoretical study is to validate this procedure for a model C–C cleavage reaction in water and by comparing predicted CO frequency shifts in water to experimental data. This paper is organized as follows: After introducing the iSMS methodology and describing the computational details in section 4.3, we present in section 4.4 the convergence properties of iSMS methodology with respect to the size of the cluster model and the size of the basis set for the C–C cleavage reaction in double-dehydrogenated ethylene glycol on Pt(111) in water. Next, we use iSMS to calculate CO frequency shifts in water on Pd(111) and Pt(111) that can be directly compared to available experimental data. Finally, conclusions are summarized in section 4.5.

4.3. Computational Details

4.3.1. iSMS Free Energy Function

The key idea of the proposed scheme is to include the long range metal interactions through periodic-slab calculations within the framework of DFT calculations in the absence of a solvent and to consider the effect of the liquid as a localized perturbation of free energy differences that can be described by cluster models embedded in an implicit continuum solvent. We define a free energy function for an adsorbed reactant on a periodic metal slab in liquid, $G_{\text{surface+reactant}}^{\text{liquid}}$, using a simple subtraction scheme

$$G_{\text{surface+reactant}}^{\text{liquid}} = E_{\text{surface+reactant}}^{\text{vacuum}} + \left(G_{\text{cluster+reactant}}^{\text{liquid}} - E_{\text{cluster+reactant}}^{\text{vacuum}} \right) \quad \dots(4.1)$$

where $E_{\text{surface+reactant}}^{\text{vacuum}}$ is the planewave DFT energy of the periodic-slab model in the absence of a solvent, $G_{\text{cluster+reactant}}^{\text{liquid}}$ is the free energy in the liquid of a metal cluster constructed by removing selected metal atoms from the periodic-slab model and removing the periodic boundary conditions, and $E_{\text{cluster+reactant}}^{\text{vacuum}}$ is the DFT energy of the same cluster in the absence of the solvent (Figure 4.1).

Equation (4.1) becomes exact for an infinitely large cluster. Any practical application however requires that this energy function converges for clusters of small size and predictable shape. Considering that the water–metal interaction only involves a limited amount of charge transfer and has been shown to be localized at the interfaces,¹⁶ we hypothesize that the indirect effect of a solvent on binding energies (by affecting the electron density of metal atoms forming the active site) is short ranged. That is, only the active site of the catalyst, the adsorbate, and their immediate environment need to be included in the cluster model. We note that similar correction schemes have been used to

study the adsorption of CO on Cu (111) with correction for exchange correlation¹⁷⁻¹⁸ and protonation reactions in zeolites with correction for long range van der Waals contributions to adsorption.¹⁹

4.3.2. DFT Calculations

All periodic planewave DFT calculations were performed using the Vienna *Ab Initio* Simulation Package (VASP 5.2)²⁰⁻²³ with Perdew–Burke–Ernzerhof (PBE) density functional.²⁴⁻²⁵ The Pt (111) surface was modeled as a 4×4 periodic slab model with four layers of metal atoms separated by a vacuum of 15 Å from its periodic image. An energy cutoff of 400 eV and energy convergence criterion of 1.0×10^{-5} eV were used for all calculations. A $4 \times 4 \times 1$ Monkhorst–Pack k-mesh²⁶ was used. Dipole and quadrupole corrections to the energy were included using a modified version of the Makov–Payne method.²⁷ Harris–Foulkes-type corrections were used for forces. Fractional occupancies of bands were allowed using the Methfessel–Paxton smearing method²⁸ within a window of 0.10 eV. Double-dehydrogenated ethylene glycol was adsorbed on a bridge site, whereas the C–C cleavage products were adsorbed on neighboring bridge sites on the same slab (Figure 4.1). The bottom two layers of the metal slab were kept fixed during geometry optimizations. The structures were relaxed until the force on each atom was less than 0.05 eV/Å. Periodic cluster models were obtained by deleting “unnecessary” atoms from the periodic-slab model (see Figure 4.1); the coordinates of all cluster atoms are equivalent to the corresponding atoms in the periodic-slab model. For these cluster models, Γ -point energy calculations were performed in a period box of 25 Å length.

Cluster-model calculations in vacuum were carried out using the TURBOMOLE 6.0 program package.²⁹⁻³¹ The cluster models were obtained by removal

of the periodic boundary conditions from the periodic cluster models. For convergence of iSMS results with respect to lateral size and depth of clusters (Figure 4.2), adsorbate atoms were represented by all-electron basis sets of triple- ζ quality (def2-TZVP).³²⁻³⁴ Pt atoms were represented by relativistic small core effective core potentials (ECPs) together with a basis set of same quality as the adsorbate atoms for the valence electrons. DFT calculations were performed with PBE functional. The RI-J approximation with auxiliary basis sets was used to approximate Coulomb potentials.³⁵⁻³⁷ Single-point energy calculations were performed with a self-consistent field (SCF) energy convergence criterion of 1.0×10^{-7} hartree. For each cluster model, multiple spin states were tested and the lowest energy spin state was used for further calculations.

For cluster models in water, COSMO³⁸ calculations were performed for the lowest energy spin state configurations at the same level of theory using radii-based cavities and a dielectric constant of 80.4 (for water).

4.4. Results and Discussion

4.4.1. C–C Cleavage in Ethylene Glycol

Figure 4.2 confirms the smooth and rapid convergence of the iSMS scheme with cluster size for calculating the free energy of C–C cleavage, $\Delta G_{\text{surface,rxn}}^{\text{water}}$, in dehydrogenated ethylene glycol on Pt (111) in water, $\text{C}_2\text{H}_4\text{O}_2 \rightleftharpoons 2\text{HCOH}$ (one H atom is removed from both C atoms and the cleavage products are coadsorbed on the surface). While periodic-slab models in vacuum predict $\Delta G_{\text{surface,rxn}}^{\text{vacuum}} = 7.5 \text{ kcal/mol}$, $\Delta G_{\text{surface,rxn}}^{\text{water}}$ converges to 9.3 kcal/mol for large clusters with the iSMS scheme. (Larger reaction energy differences between gas- and liquid-phase systems are expected for heterolytic

bond cleavages.) More importantly, the predicted values are within ± 0.5 kcal/mol of the converged value for all cluster models that are at least two layers thick and have at least one metal atom surrounding any metal atom included in the binding sites for reactant and products. Interestingly, the results are unchanged by spin-polarization of the finite metal clusters because the implicit continuum solvent does not affect their spin state and most unpaired electrons are present on the outer undercoordinated metal atoms that do not directly adsorb reactant or product species. Furthermore, Figure 4.2 shows that the use of cluster models (without iSMS) is not recommended for metal surfaces because the long range metal interactions converge slowly with cluster size.

Convergence of iSMS results for a $5 \times 5 \times 2$ cluster with respect to basis sets is shown in Figure 4.3. It can be seen that (i) iSMS converges for very small basis sets and (ii) the presence of metal clusters requires for all other methodologies basis sets of at least triple- ζ quality.

4.4.2. CO Frequency Shifts in Water

To permit a direct comparison between theory and experiment, we consider experimentally observed red-shifts in C–O stretching frequency for CO adsorption on Pd/Al₂O₃³⁹ and Pt/Al₂O₃⁴⁰ due to the presence of water. To exclude CO dipole coupling effects,⁴¹ DFT optimizations of equation (4.1) are performed at low coverage ($\theta = 1/16$ monolayer) and compared with short-time experimental results. For geometry optimizations in iSMS calculations, the top two metal layers in the periodic slabs and all atoms in the cluster models are relaxed until the maximum norms of SCF energy and basis set gradients are less than 1.0×10^{-4} au and 1.0×10^{-3} au, respectively. For the periodic-slab calculations in iSMS, an energy convergence criterion of 1.0×10^{-8} hartree

has been used. For the cluster-model calculations in iSMS, triple- ζ quality basis sets (def2-TZVP) and an energy convergence criterion of 1.0×10^{-8} hartree have been selected. Frequency calculations are performed assuming nonequilibrium solvation using numerical gradients and central differences with a step size of 0.02 au.

Table 4.1 shows that the calculated effect of water on an isolated CO molecule leads to a blue-shift in CO frequency of 8 cm^{-1} and a shortening of the C–O bond (the experimental blue-shift is 11 cm^{-1}).⁴² In contrast for adsorbed CO on Pd(111) and Pt(111), we calculate for the computationally preferred⁴³⁻⁴⁴ fcc and hcp adsorption sites red-shifts of $49\text{--}54 \text{ cm}^{-1}$ and $48\text{--}49 \text{ cm}^{-1}$ which agree well with experimental red-shifts of 58 and 50 cm^{-1} , respectively.^{39-40, 45} Because metals are perfect conductors and the relative permittivity of water is high, the direct interaction of water with CO is similar, and the observed red-shifts for adsorbed CO must largely originate from changes in bonding between CO and the transition metal surface. According to the Blyholder model,⁴⁵⁻⁴⁶ the interaction of the CO molecule with a transition metal surface is a combination of donation of electrons from the highest occupied molecular orbital (HOMO, 5σ) of CO into empty metal d-orbitals and a back-donation of electrons from metal d-orbitals into the lowest unoccupied molecular orbitals (LUMOs, $2\pi^*$) of the CO molecule. A decrease in the C–O bond order stretches the bond and causes the frequency of adsorbed CO to be red-shifted compared to the gas-phase CO molecule. In the presence of water, the metal orbitals shift to higher energy (Figure 4.4), resulting in an increased π back-donation from the metal surface to the CO molecule. Table 4.1 shows that the total charge on the adsorbed CO molecule becomes more negative in the presence of water, showing a net shift of electron density from the metal surface to the CO

molecule. The frequency is red-shifted as the C–O bond is stretched, and the C–metal bond is shortened by the presence of water. The only anomaly observed is for on-top adsorption of CO, which is a known failure of local and semi-local DFT functionals such as PBE.^{43, 47-49}

To better understand the water effect for on-top adsorption, we also performed DFT calculations using the hybrid PBE0 functional.⁵⁰ Following the procedure for including hybrid exchange from Hu et al.¹⁷⁻¹⁸ for CO adsorption on metal surfaces

$$E_{\text{surface+CO}}^{\text{PBE0}} = E_{\text{surface+CO}}^{\text{PBE}} + (E_{\text{cluster+CO}}^{\text{PBE0}} - E_{\text{cluster+CO}}^{\text{PBE}}) \quad \dots(4.2)$$

Equation (4.1) becomes the following approximate free energy function for adsorption in water

$$G_{\text{surface+CO}}^{\text{water,PBE0}} = E_{\text{surface+CO}}^{\text{vacuum,PBE}} + (G_{\text{cluster+CO}}^{\text{water,PBE0}} - E_{\text{cluster+CO}}^{\text{vacuum,PBE}}) \quad \dots(4.3)$$

For iSMS calculations with hybrid PBE0 functional, SCF calculations are performed without auxiliary basis sets. In addition, geometry optimizations are carried out with softer convergence criterion, that is, until the maximum norms of SCF energy and basis set gradient are less than 1.0×10^{-3} and 1.0×10^{-2} au, respectively. Frequency calculations in water are performed for equilibrium solvation using numerical gradients and central differences with a step size of 0.02 au. Table 4.1 shows that with the approximate inclusion of hybrid exchange red-shifts of 44 and 29 cm^{-1} are calculated for on-top adsorption on Pd (111) and Pt (111), respectively, which are again in reasonable agreement with experimental observations and the Blyholder model.

4.5. Conclusions

We presented a novel scheme to compute approximate reaction free energies of elementary reactions occurring at solid–liquid interfaces within the framework of planewave DFT and implicit solvation models developed for nonperiodic clusters. A smooth and rapid convergence is achieved for small cluster sizes that contain one metal atom next to the adsorption site in each direction as demonstrated by studying the model C–C cleavage reaction of dehydrogenated ethylene glycol on Pt. Rapid convergence with respect to the size of the basis set has also been demonstrated. Next, this scheme has been used to compute red-shifts in the metal adsorbed C–O frequency due to water. The predicted shifts are in good agreement with experimental results and can be explained using the Blyholder model as an indirect electronic effect of water on the metal atoms forming the adsorption site.

4.6. References

1. Rossmeisl, J.; Logadottir, A.; Norskov, J. K. *Chem. Phys.* **2005**, *319*, 178–184.
2. Roudgar, A.; Eikerling, M.; van Santen, R. *Phys. Chem. Chem. Phys.* **2010**, *12*, 614–620.
3. Iftimie, R.; Minary, P.; Tuckerman, M. E. *Proc. Natl. Acad. Sci. U.S.A.* **2005**, *102*, 6654–6659.
4. Cao, D.; Lu, G. Q.; Wieckowski, A.; Wasileski, S. A.; Neurock, M. *J. Phys. Chem. B* **2005**, *109*, 11622–11633.
5. Zope, B. N.; Hibbitts, D. D.; Neurock, M.; Davis, R. J. *Science* **2010**, *330*, 74–78.
6. Jacob, T.; Goddard, W. A. *ChemPhysChem* **2006**, *7*, 992–1005.
7. Cramer, C. J.; Truhlar, D. G. *Chem. Rev.* **1999**, *99*, 2161–2200.
8. Tomasi, J.; Mennucci, B.; Cammi, R. *Chem. Rev.* **2005**, *105*, 2999–3093.
9. Cramer, C. J.; Truhlar, D. G. *Acc. Chem. Res.* **2008**, *41*, 760–768.
10. Chamberlin, A. C.; Cramer, C. J.; Truhlar, D. G. *J. Phys. Chem. B* **2008**, *112*, 3024–3039.
11. Okamoto, Y. *Chem. Phys. Lett.* **2005**, *405*, 79–83.
12. Andreussi, O.; Dabo, I.; Marzari, N. *J. Chem. Phys.* **2012**, *136*, 064102.
13. York, D. M.; Karplus, M. *J. Phys. Chem. A* **1999**, *103*, 11060–11079.
14. Wang, H. F.; Liu, Z. P. *J. Phys. Chem. C* **2009**, *113*, 17502–17508.
15. Sanchez, V. M.; Sued, M.; Scherlis, D. A. *J. Chem. Phys.* **2009**, *131*, 174108.
16. Meng, S.; Wang, E. G.; Gao, S. W. *Phys. Rev. B* **2004**, *69*, 195404.
17. Hu, Q. M.; Reuter, K.; Scheffler, M. *Phys. Rev. Lett.* **2007**, *98*, 176103.

18. Hu, Q. M.; Reuter, K.; Scheffler, M. *Phys. Rev. Lett.* **2007**, *99*, 169903 Erratum.
19. Tuma, C.; Sauer, J. *Phys. Chem. Chem. Phys.* **2006**, *8*, 3955–3965.
20. Kresse, G.; Hafner, J. *Phys. Rev. B* **1993**, *47*, 558–561.
21. Kresse, G.; Hafner, J. *Phys. Rev. B* **1994**, *49*, 14251–14269.
22. Kresse, G.; Furthmüller, J. *Phys. Rev. B* **1996**, *54*, 11169–11186.
23. Hafner, J. *Comput. Phys. Commun.* **2007**, *177*, 6–13.
24. Perdew, J. P.; Burke, K.; Ernzerhof, M. *Phys. Rev. Lett.* **1996**, *77*, 3865–3868.
25. Perdew, J. P.; Burke, K.; Ernzerhof, M. *Phys. Rev. Lett.* **1997**, *78*, 1396–1396 Erratum.
26. Monkhorst, H. J.; Pack, J. D. *Phys. Rev. B* **1976**, *13*, 5188–5192.
27. Makov, G.; Payne, M. C. *Phys. Rev. B* **1995**, *51*, 4014–4022.
28. Methfessel, M.; Paxton, A. T. *Phys. Rev. B* **1989**, *40*, 3616–3621.
29. TURBOMOLE V6.0 2009, a development of University of Karlsruhe and Forschungszentrum Karlsruhe GmbH, 1989–2007, TURBOMOLE GmbH, since 2007.
30. Ahlrichs, R.; Bar, M.; Haser, M.; Horn, H.; Kolmel, C. *Chem. Phys. Lett.* **1989**, *162*, 165–169.
31. Treutler, O.; Ahlrichs, R. *J. Chem. Phys.* **1995**, *102*, 346–354.
32. Weigend, F.; Haser, M.; Patzelt, H.; Ahlrichs, R. *Chem. Phys. Lett.* **1998**, *294*, 143–152.
33. Weigend, F.; Ahlrichs, R. *Phys. Chem. Chem. Phys.* **2005**, *7*, 3297–3305.
34. Weigend, F. *Phys. Chem. Chem. Phys.* **2006**, *8*, 1057–1065.
35. Eichkorn, K.; Treutler, O.; Ohm, H.; Haser, M.; Ahlrichs, R. *Chem. Phys. Lett.* **1995**, *240*, 283–290.
36. Eichkorn, K.; Weigend, F.; Treutler, O.; Ahlrichs, R. *Theor. Chem. Acc.* **1997**, *97*, 119–124.
37. Von Arnim, M.; Ahlrichs, R. *J. Comput. Chem.* **1998**, *19*, 1746–1757.
38. Klamt, A.; Schuurmann, G. *J. Chem. Soc., Perkin Trans. 2* **1993**, 799–805.
39. Ebbesen, S. D.; Mojet, B. L.; Lefferts, L. *Phys. Chem. Chem. Phys.* **2009**, *11*, 641–649.
40. Ebbesen, S. D.; Mojet, B. L.; Lefferts, L. *J. Catal.* **2007**, *246*, 66–73.
41. Chang, S. C.; Weaver, M. J. *J. Chem. Phys.* **1990**, *92*, 4582–4594.
42. Brookes, M. D.; McKellar, A. R. W. *J. Chem. Phys.* **1998**, *109*, 5823–5829.
43. Feibelman, P. J.; Hammer, B.; Norskov, J. K.; Wagner, F.; Scheffler, M.; Stumpf, R.; Watwe, R.; Dumesic, J. *J. Phys. Chem. B* **2001**, *105*, 4018–4025.
44. See Appendix A for complete results for Table 4.1.
45. Mojet, B. L.; Ebbesen, S. D.; Lefferts, L. *Chem. Soc. Rev.* **2010**, *39*, 4643–4655.
46. Blyholder, G. *J. Phys. Chem.* **1964**, *68*, 2772–2777.
47. Kresse, G.; Gil, A.; Sautet, P. *Phys. Rev. B* **2003**, *68*, 073401.
48. Stroppa, A.; Termentzidis, K.; Paier, J.; Kresse, G.; Hafner, J. *Phys. Rev. B* **2007**, *76*, 195440.
49. Lazic, P.; Alaei, M.; Atodiresei, N.; Caciuc, V.; Brako, R.; Blugel, S. *Phys. Rev. B* **2010**, *81*, 045401.
50. Perdew, J. P.; Ernzerhof, M.; Burke, K. *J. Chem. Phys.* **1996**, *105*, 9982–9985.

Table 4.1. Effect of water on CO adsorption on Pd (111) and Pt (111).^a

	N_{metal}	$\Delta\nu_{\text{C-O}}$ (cm^{-1})	$\Delta\Delta G_{\text{ads}}$ (kcal/mol)	$\Delta L_{\text{C-O}}$ (pm)	$\Delta L_{\text{C-M}}$ (pm)	Δq_{CO} (au)
CO molecule ($\Delta\nu_{\text{C-O,exp}} = +11$) ⁴²						
		+8		-0.06		
CO on Pd (111) ^b ($\Delta\nu_{\text{C-O,exp}} = -58$) ³⁹						
top	19	-2 (-44) ^c	+0.72 (-0.11)	+0.16 (+0.20)	-0.53 (-0.52)	-0.015 (-0.068)
fcc	24	-49	-1.41	+0.92	-1.02	-0.069
hcp	22	-54	-2.42	+1.01	-1.24	-0.075
CO on Pt (111) ^b ($\Delta\nu_{\text{C-O,exp}} = -50$) ⁴⁰						
top	19	+78 (-29) ^c	+0.23 (-2.00)	-0.06 (+0.01)	-0.17 (-0.14)	+0.003 (-0.071)
fcc	24	-49	-1.46	+0.88	-0.92	-0.069
hcp	22	-48	-1.37	+0.90	-1.26	-0.069

^a Calculated effect of water on C–O stretching frequency ($\Delta\nu_{\text{C-O}}$), free energy of adsorption ($\Delta\Delta G_{\text{ads}}$), C–O ($\Delta L_{\text{C-O}}$) and C–metal ($\Delta L_{\text{C-M}}$) bond lengths, and total charge on adsorbed CO (Δq_{CO}) from Mullikan population analysis with PBE functional. N_{metal} is the number of atoms in the metal cluster. Values in parentheses for on-top adsorption show results obtained with PBE0 functional.

^b CO adsorbed on bridge site moves to an fcc site during optimization in water.

^c Equilibrium solvation frequency shift only.

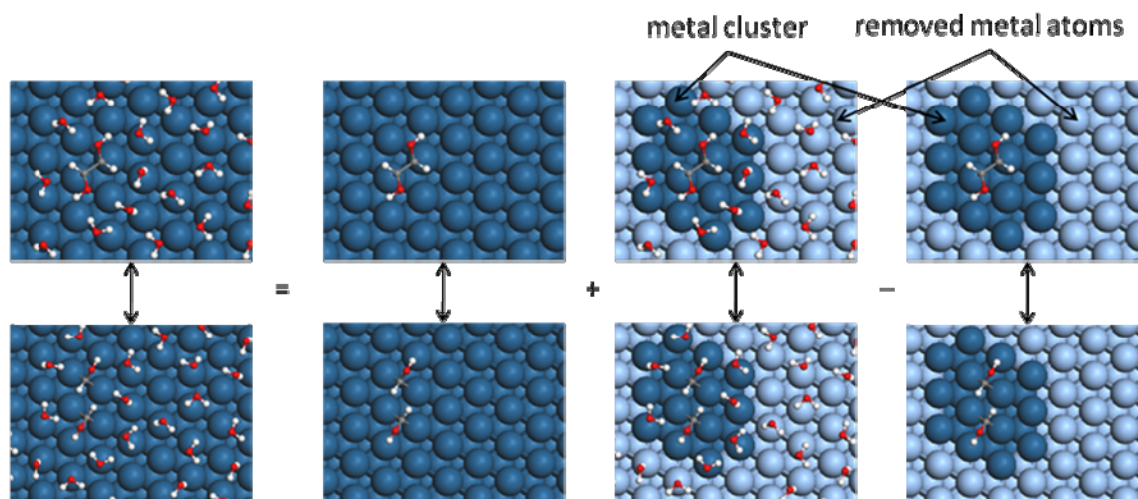


Figure 4.1. Schematic representation of equation (4.1) for calculation of $\Delta G_{\text{surface,rxn}}^{\text{water}}$ for C–C bond cleavage in dehydrogenated ethylene glycol on Pt(111) in water. Arrows connect reactant (up) to cleavage products (down) in the respective models. The four models from left to right are periodic slab in water, periodic slab in vacuum, cluster in water, and cluster in vacuum. Explicit water molecules are shown for illustrative purposes only.

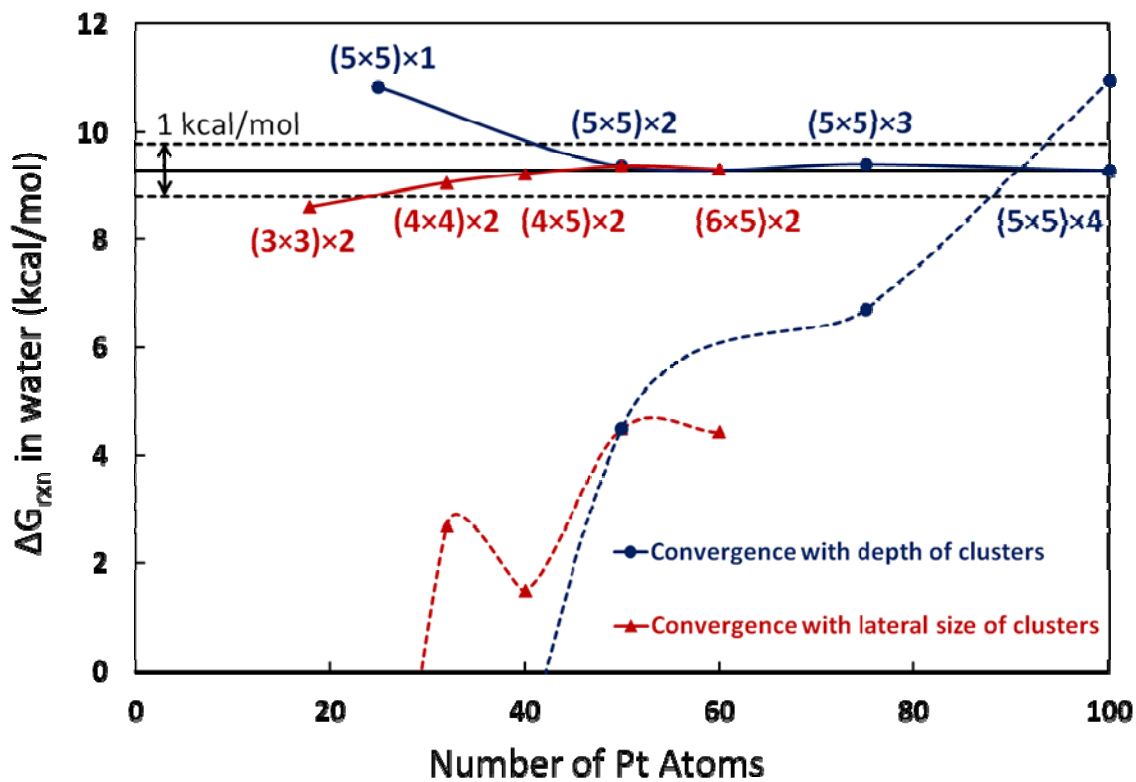


Figure 4.2. Convergence of $\Delta G_{\text{surface,rxn}}^{\text{water}}$ for C–C bond cleavage in dehydrogenated ethylene glycol on Pt (111) in water with iSMS scheme. A value of 9.3 kcal/mol obtained for a $(5 \times 5) \times 4$ cluster is used as reference (solid horizontal line). Cluster model calculations in implicit solvent (without iSMS) are shown as dashed curves.

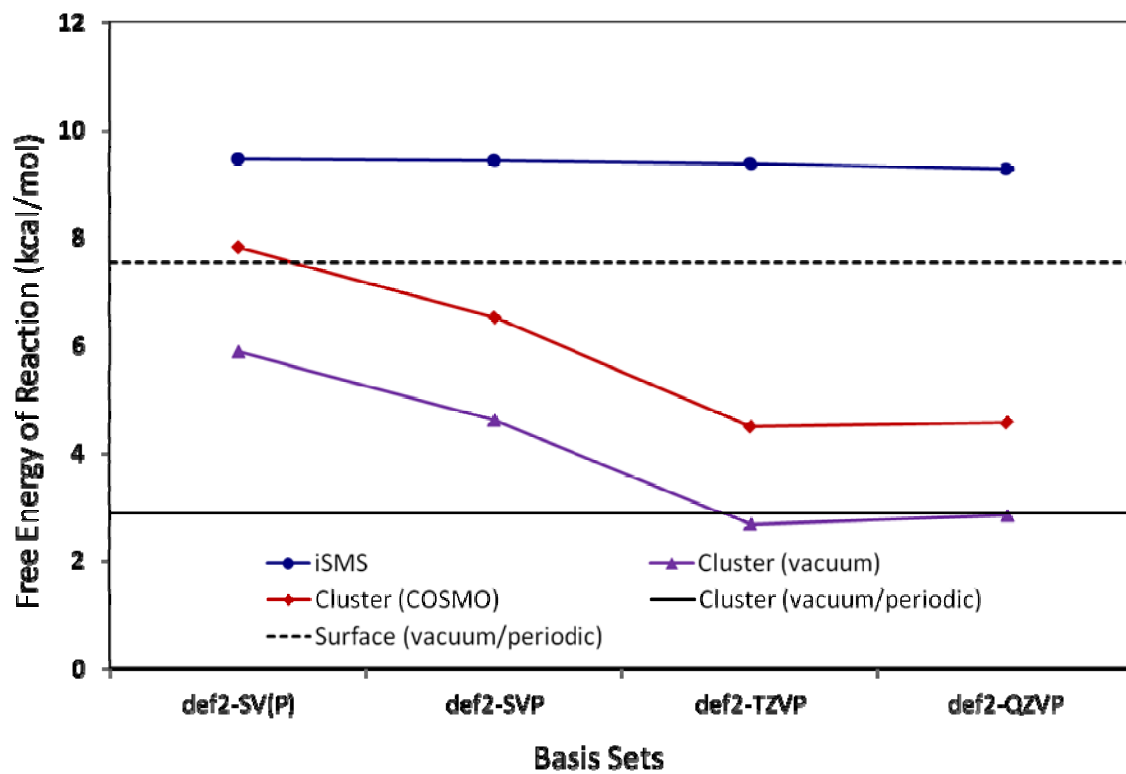


Figure 4.3. Basis set convergence for C–C cleavage in dehydrogenated ethylene glycol on a $5 \times 5 \times 2$ cluster of Pt (111).

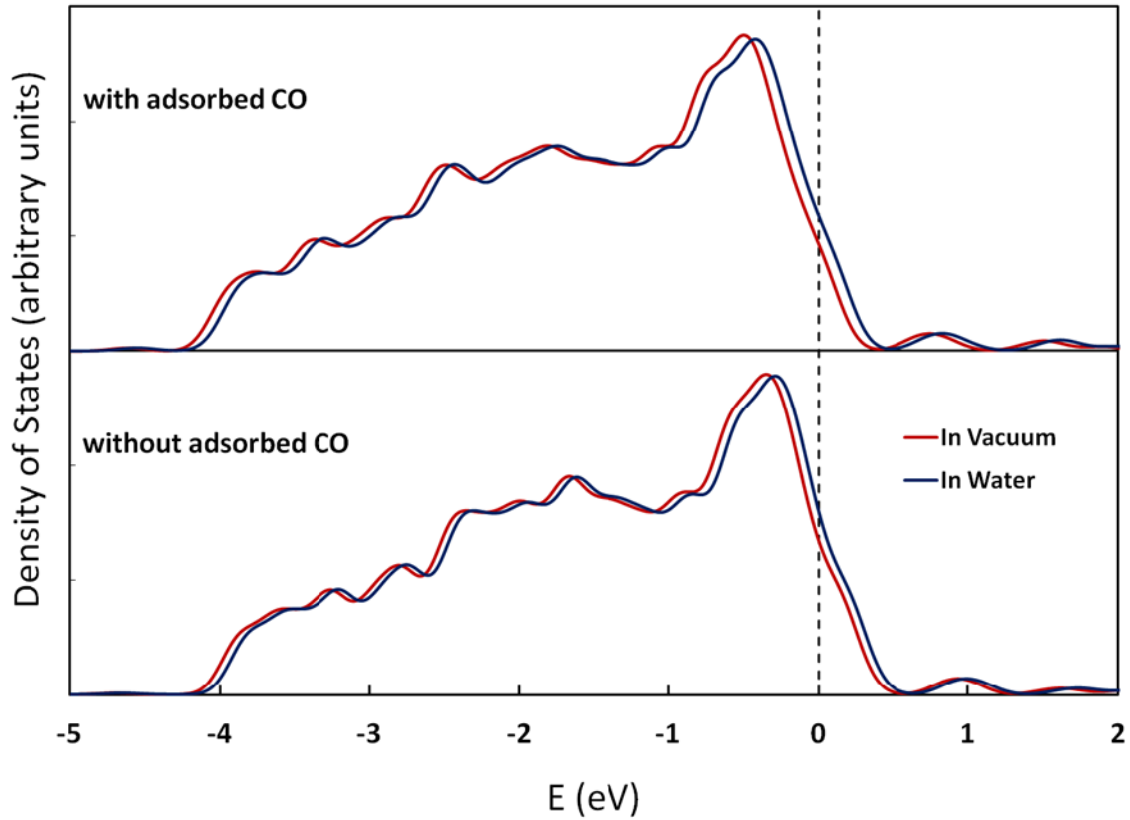


Figure 4.4. Shift in electronic density of states (DOS) due to water for 24-atom Pd (111) cluster with and without CO adsorbed on an fcc site. Only metal d-states are plotted for each case.

CHAPTER 5

HYBRID QUANTUM MECHANICS/MOLECULAR MECHANICS SOLVATION SCHEME FOR COMPUTING FREE ENERGIES OF REACTIONS AT METAL–WATER INTERFACES

5.1. Summary

We report the development of a quantum mechanics/molecular mechanics free energy perturbation (QM/MM-FEP) method for modeling chemical reactions at metal–water interfaces. This novel solvation scheme combines planewave density function theory (DFT), periodic electrostatic embedded cluster method (PEECM) calculations using Gaussian-type orbitals, and classical molecular dynamics (MD) simulations to obtain a free energy description of a complex metal–water system. We derive a potential of mean force (PMF) of the reaction system within the QM/MM framework. A fixed-size, finite ensemble of MM conformations is used to permit precise evaluation of the PMF of QM coordinates and its gradient defined within this ensemble. Local conformations of adsorbed reaction moieties are optimized using sequential MD-sampling and QM-optimization steps. An approximate reaction coordinate is constructed using a number of interpolated states and the free energy difference between adjacent states is calculated using the QM/MM-FEP method. By avoiding on-the-fly QM

Adapted with permission from Faheem, M.; Heyden, A. *J. Chem. Theory Comput.* **2014**, *10*, In Press. [Online Early Access] DOI: 10.1021/ct500211w. © 2014 American Chemical Society.

calculations and by circumventing the challenges associated with statistical averaging during MD sampling, a computational speedup of multiple orders of magnitude is realized. The method is systematically validated against the results of *ab initio* QM calculations and demonstrated for C–C cleavage in double-dehydrogenated ethylene glycol on a Pt (111) model surface.

5.2. Introduction

Computational investigations of chemical reactions at solid–liquid interfaces have long been and continue to be very challenging. Liquid molecules can affect the activity and selectivity of a heterogeneous catalyst in a variety of ways. Long range electrostatic interactions of solvent molecules with other solvent molecules and with the catalyst and the adsorbed moieties create a reaction environment that is radically different from the gas phase, resulting in stabilization or destabilization of charged intermediates and transition states.¹ Nonharmonic dynamic fluctuations in a complex liquid phase and diffusion of the solvent molecules can affect reactant and product diffusivities² and alter the dynamics of energy accumulation and relaxation. Direct participation of solvent molecules in the reaction mechanism not only causes a concentration effect on the overall rate of reaction but can also provide lower-energy pathways, for example, for proton transfer between neighboring active sites.³ Solute–solvent phase equilibria can affect the overall selectivity by suppressing or enhancing various reaction pathways.⁴ Reaction free energies, free energy barriers, and turnover frequencies of elementary reaction steps occurring at a solid–liquid interface can therefore be very different from when the same processes occur at a solid–gas interface.⁵ Unfortunately, due to a lack of a well-established methodology for describing the influence of dynamic fluctuations of the

liquid phase on chemical reactions across a solid–liquid interface with quantum mechanical (QM) accuracy, we have currently only a limited understanding of the structure–activity relationships of heterogeneous catalysts in liquid phase and we are unable to rationally design new catalytic materials for liquid phase processes.

Computer simulations of chemical reactions at solid–liquid interfaces face multiple challenges. First, the potential energy surface (PES) must accurately describe the electronic structure of the most interesting part of the system directly involved in the bond forming or breaking process, that is, the active site of the catalyst, adsorbed moiety, and possibly some solvent molecules in the immediate neighborhood. Second, a significant fraction of the system configuration space must be sampled for calculation of accurate free energy differences and to ensure that the results are statistically converged. Finally, nonharmonic dynamic fluctuations in the liquid phase, long range electrostatic interactions between water molecules, delocalization of electrons in transition metals, and finite size effects⁶⁻⁷ require the computational model to be sufficiently large. Although *ab initio* molecular dynamics (AIMD) approaches⁸ can, in principle, be used for such simulations, current computer technology and resources limit a full quantum mechanical treatment of the entire condensed-phase reaction system to a few hundred atoms and a few picoseconds of simulation time.⁹⁻¹¹ This necessitates the development of alternative computational approaches that are nearly as accurate as AIMD but computationally multiple (5–7) orders of magnitude less expensive.

One approach that circumvents these problems is the use of isotropic continuum solvation models.¹²⁻¹³ The solvent is modeled as a homogeneous medium characterized by an appropriate dielectric constant, and the solute is placed in carefully constructed

cavities within this continuum.¹⁴ QM charge distribution of the solute polarizes the surrounding dielectric medium. The response of the polarized solvent creates a reaction field which is included as electrostatic potential (ESP) in the self-consistent field (SCF) calculations at the same level of QM theory. Implicit solvation models are computationally very efficient because, in the absence of explicit solvent molecules, the size of the electronic structure problem is the same as in gas phase. This approach has been used to study the formation of water on Pt and Pt-based alloys¹⁵ and the oxidation of formic acid at the Pt/H₂O interface.¹⁶ Recently, we have developed the iSMS¹⁷ (Implicit Solvation for Metal Surfaces) method for combining nonperiodic implicit solvation models with planewave density functional theory (DFT) calculations to describe the effect of solvents on processes occurring at “periodic” metal–water interfaces. This method has been successfully applied for calculating CO frequency shifts on Pd/H₂O and Pt/H₂O interfaces¹⁷ and for predicting solvent effects on the hydrodeoxygenation of propanoic acid over Pd (111).¹⁸ Although implicit solvation models are generally reasonably accurate for computing free energies in solution, they cannot correctly reproduce the anisotropic site-specific interactions¹⁹ between the solute and solvent molecules over a solid catalyst. Inclusion of one or more explicit solvent molecules as part of the QM solute structure may help in some cases,¹⁶ but the broader challenge of sampling the configuration space of a complex liquid environment in a statistically relevant manner remains unaddressed.

An alternative approach based on *ab initio* QM calculations consists of optimizing a hexagonally close-packed ice-like network of water molecules²⁰⁻²¹ at the metal interface before replacing one of the water molecules with a reaction moiety. The preoptimized

water network effectively serves as an initial guess for further geometry optimizations and transition state searches. This approach has been used to study methanol decomposition on Pt (111)²² and selective oxidation of ethanol to acetic acid on Pt (111) and Au (111).²³ However, such “freezing” of the water structure leads to insufficient sampling of the water configuration space and the predicted adsorption energies and activation barriers are often highly dependent on the initial structure guess. A more suitable approach would be to perform such optimizations in an average field of a sufficiently large number of water conformations. This is, however, impossible with *ab initio* methods for the foreseeable future.

The dual need for both accurate electronic structure calculations and extensive configuration space sampling is not unique for reactions at metal–water interfaces. A similar problem is encountered in modeling enzyme-catalyzed processes and molecular biological systems where the system of interest often contains tens of thousands to millions of atoms. A closer examination reveals that, in many chemical reactions, bond breaking and forming are localized events and involve relatively few atoms. The interactions of these “active” atoms must be described accurately. Atoms in the remainder of the system experience minimal changes in their electronic structures but still contribute to the reaction process by creating a unique steric and electrostatic environment around the active site. This permits the use of multilevel quantum mechanical/molecular mechanical (QM/MM) methods²⁴ where only the active site of, for example, the enzyme and its immediate environment, that make the most important and direct contributions to the electronic structure of the atoms involved in reaction chemistry, are described quantum mechanically, whereas the remainder of the system, for

example, the nonreactive part of the enzyme and the bulk of the liquid water, is treated at classical molecular mechanical level of theory. This combination of a moderately-sized QM region and a large classical MM region provides an accurate yet computationally affordable energetic description of the complex system. Similar arguments can be made for metal-catalyzed reactions in water. For most reaction moieties, the adsorption site involves a handful of metal atoms. Metal–water interactions only involve a limited amount of charge transfer that is localized at the interface.²⁵ In addition, we have recently shown that the effect of water on the bonding characteristics of transition metal surfaces with adsorbates is short ranged in metal.¹⁷ Noting that the enzyme catalysis community has developed various highly efficient QM/MM algorithms for calculating reaction free energies and free energy barriers,²⁶⁻³⁰ we hypothesize that it is possible to develop similar approaches for simulating chemical reactions at metal–water interfaces.

In this paper, we report the development of a hybrid QM/MM methodology, named eSMS (Explicit Solvation for Metal Surfaces), for modeling reactions at metal–water interfaces. The proposed procedure has similarity to our recently developed iSMS method but uses an all-atom description of the reaction system, involves QM/MM-FEP (free energy perturbation)³¹ calculations and can therefore be considered as a bridge between implicit solvation models and AIMD approaches. The objective of this theoretical study is to validate this procedure for a model C–C cleavage reaction at the Pt (111)/H₂O interface. This paper is organized as follows: In section 5.3, we first introduce our QM/MM approach and derive an expression for the total QM/MM energy with approximate QM/MM electrostatic interactions. We then derive an equivalent but more practical expression that permits easier integration of various QM and MD program

packages. Next, we derive expressions for the potential of mean force (PMF) of QM coordinates and its gradient within the QM/MM-FEP framework and show how these results can be integrated with our eSMS method in a step-by-step procedure. Computational details are outlined in section 5.4 and comprehensive results addressing the validation and application of the proposed methodology are presented in section 5.5. Finally, general conclusions of this work are summarized in section 5.6.

5.3. Theory

5.3.1. Approximate Total QM/MM Energy Function

In the combined QM/MM approach, the model system is partitioned into QM (\mathbf{r}_{QM}) and MM (\mathbf{r}_{MM}) subsystems. Each atom of the entire system is assigned to either of the subsystems. Because of the interaction between the two subsystems, the total QM/MM energy is not simply a sum of the energies of the individual subsystems, but must also include their interaction energy. In general,³² the total energy of the system (E_{T}) can be written as

$$E_{\text{T}}(\mathbf{r}_{\text{QM}}, \mathbf{r}_{\text{MM}}) = E_{\text{QM}}(\mathbf{r}_{\text{QM}}) + E_{\text{QM/MM}}(\mathbf{r}_{\text{QM}}, \mathbf{r}_{\text{MM}}) + E_{\text{MM}}(\mathbf{r}_{\text{MM}}) \quad \dots(5.1)$$

The three terms on the right-hand side are the energy of the QM subsystem (E_{QM}), the interaction energy between the QM and MM subsystems ($E_{\text{QM/MM}}$), and the energy of the MM subsystem (E_{MM}), respectively. Equation (5.1) is the working equation adopted in the majority of QM/MM schemes³² and carries no assumption as long as the selected QM and MM methods are capable of describing the respective subsystems and their interaction. The QM/MM interaction energy can be further decomposed into electrostatic

$(E_{QM/MM}^{elec})$, van der Waals $(E_{QM/MM}^{vdW})$ and covalent $(E_{QM/MM}^{cov})$ contributions. For simulating elementary processes at metal–water interfaces, we define a QM subsystem containing some metal atoms, adsorbed reaction moieties, and possibly a few water molecules, whereas the MM subsystem contains only water molecules and metal atoms far away from the reaction site. Because there are no covalent bonds connecting the QM and MM subsystems in our problems of interest (there are only metallic bonds), this partitioning scheme considerably simplifies the description of the boundary between the two subsystems and as we will show below, eliminates the need to consider alternative approaches, for example, adding link hydrogen atoms,³³ pseudo-bond method,³⁴ or the frozen local-orbital method.³⁵

$$E_T(\mathbf{r}_{QM}, \mathbf{r}_{MM}) = \begin{cases} E_{QM}(\mathbf{r}_{QM}) + E_{QM/MM}^{elec}(\mathbf{r}_{QM}, \mathbf{r}_{MM}) + \\ E_{QM/MM}^{vdW}(\mathbf{r}_{QM}, \mathbf{r}_{MM}) + E_{MM}(\mathbf{r}_{MM}) \end{cases} \dots(5.2)$$

Using an electrostatic embedding scheme, the electrostatic potential (ESP) from the MM atoms can be rigorously included in the QM calculations at the same level of theory, allowing the QM energy (E_{QM}) and QM/MM electrostatic interaction energy $(E_{QM/MM}^{elec})$ to be computed together in a self-consistent manner.

$$E_{QM}(\mathbf{r}_{QM}) + E_{QM/MM}^{elec}(\mathbf{r}_{QM}, \mathbf{r}_{MM}) = \langle \Psi | H_{eff}(\mathbf{r}_{QM}, \mathbf{r}_{MM}) | \Psi \rangle \dots(5.3)$$

$$E_T(\mathbf{r}_{QM}, \mathbf{r}_{MM}) = \langle \Psi | H_{eff}(\mathbf{r}_{QM}, \mathbf{r}_{MM}) | \Psi \rangle + E_{QM/MM}^{vdW}(\mathbf{r}_{QM}, \mathbf{r}_{MM}) + E_{MM}(\mathbf{r}_{MM}) \dots(5.4)$$

Here, H_{eff} is the effective QM Hamiltonian which includes the electrostatic potential of the MM subsystem, and Ψ is the electronic wavefunction of the QM subsystem. Computation of this wavefunction is the bottleneck for application of Eq. (5.4) because a

new SCF calculation is required for each QM or MM conformation. To address this problem, we consider the reaction path potential (RPP) method developed by Lu and Yang.³⁶ The idea is to separate the QM energy into two components that can be expanded analytically in terms of both changes in the QM conformation and the MM electrostatic potential. We assume that the QM/MM electrostatic interaction can be approximated as the Coulombic interactions between MM point charges and ESP-fitted charges on the QM atoms.

$$E_{\text{QM/MM}}^{\text{elec(ESP)}}(\underline{r}_{\text{QM}}, \underline{r}_{\text{MM}}) = \sum_{j \in \text{MM}} \sum_{i \in \text{QM}} \frac{q_j Q_i(\underline{r}_{\text{QM}}, \underline{r}_{\text{MM}})}{|\underline{r}_{\text{QM},i} - \underline{r}_{\text{MM},j}|} \quad \dots(5.5)$$

Here, q_j is the point charge of MM atom j from the MM force field which is usually a constant. The ESP-fitted charge of QM atom i , $Q_i(\underline{r}_{\text{QM}}, \underline{r}_{\text{MM}})$, depends on all QM and MM coordinates in the system. Next, we define a QM internal energy function³⁶ (E'_{QM}) as the energy of the QM subsystem in the presence of an electrostatic field of MM point charges, minus the Coulombic interactions between MM point charges and ESP-fitted charges of QM atoms.

$$E'_{\text{QM}}(\underline{r}_{\text{QM}}, \underline{r}_{\text{MM}}) \equiv \langle \Psi | H_{\text{eff}}(\underline{r}_{\text{QM}}, \underline{r}_{\text{MM}}) | \Psi \rangle - E_{\text{QM/MM}}^{\text{elec(ESP)}}(\underline{r}_{\text{QM}}, \underline{r}_{\text{MM}}) \quad \dots(5.6)$$

Equation (5.4) can now be written as

$$E_{\text{T}}(\underline{r}_{\text{QM}}, \underline{r}_{\text{MM}}) = \begin{cases} E'_{\text{QM}}(\underline{r}_{\text{QM}}, \underline{r}_{\text{MM}}) + \sum_{j \in \text{MM}} \sum_{i \in \text{QM}} \frac{q_j Q_i(\underline{r}_{\text{QM}}, \underline{r}_{\text{MM}})}{|\underline{r}_{\text{QM},i} - \underline{r}_{\text{MM},j}|} + \\ E_{\text{QM/MM}}^{\text{vdW}}(\underline{r}_{\text{QM}}, \underline{r}_{\text{MM}}) + E_{\text{MM}}(\underline{r}_{\text{MM}}) \end{cases} \quad \dots(5.7)$$

Calculation of E'_{QM} also requires a new SCF calculation for each QM or MM conformation. For configuration space sampling in long-time MD simulations, it is highly

desirable to reformulate Eq. (5.7) as an approximate total QM/MM energy function without the need for recurrent SCF calculations.

In this context, perturbation theory can be used where changes in the total energy of the system, for a given QM conformation, are characterized by the response to changes in electrostatic potential of the MM atoms. Although expressions for higher-order perturbations are available,³⁶⁻³⁹ we limit our approach to a zero-order approximation, assuming that it is adequate to neglect changes in polarization of the QM subsystem in response to moving MM atoms in the environment. In other words, both QM conformation and QM electron density are frozen during MD simulations.^{29, 37} Using a reference MM conformation $\underline{\mathbf{r}}_{\text{MM}}^0$

$$Q_i(\underline{\mathbf{r}}_{\text{QM}}, \underline{\mathbf{r}}_{\text{MM}}) \approx Q_i(\underline{\mathbf{r}}_{\text{QM}}, \underline{\mathbf{r}}_{\text{MM}}^0)$$

$$E_{\text{QM/MM}}^{\text{elec(ESP)}}(\underline{\mathbf{r}}_{\text{QM}}, \underline{\mathbf{r}}_{\text{MM}}) = \sum_{j \in \text{MM}} \sum_{i \in \text{QM}} \frac{q_j Q_i(\underline{\mathbf{r}}_{\text{QM}}, \underline{\mathbf{r}}_{\text{MM}})}{|\underline{\mathbf{r}}_{\text{QM},i} - \underline{\mathbf{r}}_{\text{MM},j}|} \approx \sum_{j \in \text{MM}} \sum_{i \in \text{QM}} \frac{q_j Q_i(\underline{\mathbf{r}}_{\text{QM}}, \underline{\mathbf{r}}_{\text{MM}}^0)}{|\underline{\mathbf{r}}_{\text{QM},i} - \underline{\mathbf{r}}_{\text{MM},j}|} \quad \dots(5.8)$$

$$E'_{\text{QM}}(\underline{\mathbf{r}}_{\text{QM}}, \underline{\mathbf{r}}_{\text{MM}}) \approx E'_{\text{QM}}(\underline{\mathbf{r}}_{\text{QM}}, \underline{\mathbf{r}}_{\text{MM}}^0)$$

$$= \langle \Psi | H_{\text{eff}}(\underline{\mathbf{r}}_{\text{QM}}, \underline{\mathbf{r}}_{\text{MM}}^0) | \Psi \rangle - \sum_{j \in \text{MM}} \sum_{i \in \text{QM}} \frac{q_j Q_i(\underline{\mathbf{r}}_{\text{QM}}, \underline{\mathbf{r}}_{\text{MM}}^0)}{|\underline{\mathbf{r}}_{\text{QM},i} - \underline{\mathbf{r}}_{\text{MM},j}^0|} \quad \dots(5.9)$$

With these assumptions, the approximate total QM/MM energy (\tilde{E}_T) is written using Eq.

(5.7)

$$\tilde{E}_T(\underline{\mathbf{r}}_{\text{QM}}, \underline{\mathbf{r}}_{\text{MM}}) = \begin{cases} \langle \Psi | H_{\text{eff}}(\underline{\mathbf{r}}_{\text{QM}}, \underline{\mathbf{r}}_{\text{MM}}^0) | \Psi \rangle - \sum_{j \in \text{MM}} \sum_{i \in \text{QM}} \frac{q_j Q_i(\underline{\mathbf{r}}_{\text{QM}}, \underline{\mathbf{r}}_{\text{MM}}^0)}{|\underline{\mathbf{r}}_{\text{QM},i} - \underline{\mathbf{r}}_{\text{MM},j}^0|} + \\ \sum_{j \in \text{MM}} \sum_{i \in \text{QM}} \frac{q_j Q_i(\underline{\mathbf{r}}_{\text{QM}}, \underline{\mathbf{r}}_{\text{MM}}^0)}{|\underline{\mathbf{r}}_{\text{QM},i} - \underline{\mathbf{r}}_{\text{MM},j}|} + E_{\text{QM/MM}}^{\text{vdW}}(\underline{\mathbf{r}}_{\text{QM}}, \underline{\mathbf{r}}_{\text{MM}}) + E_{\text{MM}}(\underline{\mathbf{r}}_{\text{MM}}) \end{cases} \quad \dots(5.10)$$

We note here that the Coulombic interaction term describing $\left(E_{QM/MM}^{elec(ESP)}\right)$ is included in Eq. (5.10) twice in different contexts. First, it is subtracted as a constant evaluated at the reference MM conformation; then it is added for all MM conformations assuming constant ESP charges for the QM atoms (evaluated at the reference MM conformation).

5.3.2. Alternative Expression for the Approximate Total QM/MM Energy Function

When the QM and MM calculations are performed using different program packages, there is a need to streamline the communication and exchange of information between them. In the following, we derive an equivalent but more practical expression for the approximate total QM/MM energy function. As described earlier, an electrostatic embedding scheme will be used to calculate both the energy of the QM subsystem and the QM/MM electrostatic interactions in a self-consistent manner. However, in most program packages these calculations do not include the electrostatic and van der Waals interactions within the MM subsystem and the van der Waals interactions between the QM and MM subsystems. All these contributions must be included with the MM program package. The total energy of the QM/MM system in a reference MM conformation can be expressed as

$$E_T(\mathbf{r}_{QM}, \mathbf{r}_{MM}^0) = \langle \Psi | H_{\text{eff}}(\mathbf{r}_{QM}, \mathbf{r}_{MM}^0) | \Psi \rangle + E_{MM}^{elec}(\mathbf{r}_{MM}^0) + E_{MM+QM/MM}^{vdW}(\mathbf{r}_{QM}, \mathbf{r}_{MM}^0) \quad \dots(5.11)$$

where we neglected for simplicity all intramolecular force field contributions in the MM subsystem because they are not present in most water force field models. Adding these intramolecular contributions for any solvent model does not add any complication as long as the QM/MM interface does not cross chemical bonds.

Substituting Eq. (5.6) in Eq. (5.11) and noting that ESP charges are required only for QM atoms whereas point charges for MM atoms are obtained from the force field

$$E_T(\underline{r}_{QM}, \underline{r}_{MM}^0) = \begin{cases} E'_{QM}(\underline{r}_{QM}, \underline{r}_{MM}^0) + E_{MM+QM/MM}^{elec(ESP)}(\underline{r}_{QM}, \underline{r}_{MM}^0) + \\ E_{MM+QM/MM}^{vdW}(\underline{r}_{QM}, \underline{r}_{MM}^0) \end{cases} \dots(5.12)$$

Similarly, for any other MM conformation

$$E_T(\underline{r}_{QM}, \underline{r}_{MM}) = \begin{cases} E'_{QM}(\underline{r}_{QM}, \underline{r}_{MM}) + E_{MM+QM/MM}^{elec(ESP)}(\underline{r}_{QM}, \underline{r}_{MM}) + \\ E_{MM+QM/MM}^{vdW}(\underline{r}_{QM}, \underline{r}_{MM}) \end{cases} \dots(5.13)$$

Subtracting Eq. (5.12) from Eq. (5.13)

$$\begin{matrix} E_T(\underline{r}_{QM}, \underline{r}_{MM}) - \\ E_T(\underline{r}_{QM}, \underline{r}_{MM}^0) \end{matrix} = \begin{cases} E'_{QM}(\underline{r}_{QM}, \underline{r}_{MM}) - E'_{QM}(\underline{r}_{QM}, \underline{r}_{MM}^0) + \\ E_{MM+QM/MM}^{elec(ESP)}(\underline{r}_{QM}, \underline{r}_{MM}) - E_{MM+QM/MM}^{elec(ESP)}(\underline{r}_{QM}, \underline{r}_{MM}^0) + \\ E_{MM+QM/MM}^{vdW}(\underline{r}_{QM}, \underline{r}_{MM}) - E_{MM+QM/MM}^{vdW}(\underline{r}_{QM}, \underline{r}_{MM}^0) \end{cases} \dots(5.14)$$

Making the approximation of an invariant QM internal energy function as in Eq. (5.9), the first two terms on the right-hand side of Eq. (5.14) cancel each other. In addition, assumption of invariant polarization of QM atoms (Eq.(5.8)) means that the electrostatic interactions within the QM subsystem will be exactly same for all MM conformations.

$$\begin{aligned} Q_i(\underline{r}_{QM}, \underline{r}_{MM}) &\approx Q_i(\underline{r}_{QM}, \underline{r}_{MM}^0) \\ E_{QM}^{elec(ESP)}(\underline{r}_{QM}) &= E_{QM}^{elec(ESP)}(\underline{r}_{QM}, \underline{r}_{MM}) = E_{QM}^{elec(ESP)}(\underline{r}_{QM}, \underline{r}_{MM}^0) = \text{constant} \end{aligned} \dots(5.15)$$

With these assumptions, Eq. (5.14) is rewritten as

$$\begin{matrix} \tilde{E}_T(\underline{r}_{QM}, \underline{r}_{MM}) - \\ E_T(\underline{r}_{QM}, \underline{r}_{MM}^0) \end{matrix} = \begin{cases} E_{MM+QM/MM}^{elec(ESP)}(\underline{r}_{QM}, \underline{r}_{MM}) - E_{MM+QM/MM}^{elec(ESP)}(\underline{r}_{QM}, \underline{r}_{MM}^0) + \\ E_{MM+QM/MM}^{vdW}(\underline{r}_{QM}, \underline{r}_{MM}) - E_{MM+QM/MM}^{vdW}(\underline{r}_{QM}, \underline{r}_{MM}^0) \end{cases} \dots(5.16)$$

Combining terms that can be computed together

$$\tilde{E}_T(\underline{r}_{QM}, \underline{r}_{MM}) - E_T(\underline{r}_{QM}, \underline{r}_{MM}^0) = \begin{cases} E_{QM+MM+QM/MM}^{\text{elec(ESP)+vdW}}(\underline{r}_{QM}, \underline{r}_{MM}) - \\ E_{QM+MM+QM/MM}^{\text{elec(ESP)+vdW}}(\underline{r}_{QM}, \underline{r}_{MM}^0) \end{cases} \quad \dots(5.17)$$

where $E_{QM+MM+QM/MM}^{\text{elec(ESP)+vdW}}(\underline{r}_{QM}, \underline{r}_{MM})$ is the energy of the total system at the MM level of theory. We note that the electrostatic and van der Waals interactions of the QM subsystem cancel on the right side of Eq. (5.17) due to an identical QM geometry and the frozen charge approximation. Finally, substituting Eq. (5.11) in Eq. (5.17) and rearranging

$$\tilde{E}_T(\underline{r}_{QM}, \underline{r}_{MM}) = \begin{cases} \langle \Psi | H_{\text{eff}}(\underline{r}_{QM}, \underline{r}_{MM}^0) | \Psi \rangle + \\ E_{MM}^{\text{elec}}(\underline{r}_{MM}^0) + E_{MM+QM/MM}^{\text{vdW}}(\underline{r}_{QM}, \underline{r}_{MM}^0) + \\ E_{QM+MM+QM/MM}^{\text{elec(ESP)+vdW}}(\underline{r}_{QM}, \underline{r}_{MM}) - E_{QM+MM+QM/MM}^{\text{elec(ESP)+vdW}}(\underline{r}_{QM}, \underline{r}_{MM}^0) \end{cases} \quad \dots(5.18)$$

The second and third terms on right-hand side can be combined by removing charges from all QM atoms in their evaluation.

$$\tilde{E}_T(\underline{r}_{QM}, \underline{r}_{MM}) = \begin{cases} \langle \Psi | H_{\text{eff}}(\underline{r}_{QM}, \underline{r}_{MM}^0) | \Psi \rangle + \left[E_{MM+QM/MM}^{\text{elec+vdW}}(\underline{r}_{QM}, \underline{r}_{MM}^0) \right]_{Q_i=0, i \in QM} + \\ E_{QM+MM+QM/MM}^{\text{elec(ESP)+vdW}}(\underline{r}_{QM}, \underline{r}_{MM}) - E_{QM+MM+QM/MM}^{\text{elec(ESP)+vdW}}(\underline{r}_{QM}, \underline{r}_{MM}^0) \end{cases} \quad \dots(5.19)$$

Evaluation of $\tilde{E}_T(\underline{r}_{QM}, \underline{r}_{MM})$ using Eq. (5.19) thus requires one SCF calculation in the electrostatic potential of the reference MM conformation to obtain the QM internal energy and ESP-fitted charges for the QM atoms, one MM calculation for each MM conformation where all QM atoms are assigned ESP-fitted charges, and one additional MM calculation for the reference MM conformation where charges from all QM atoms have been removed.

Equation (5.19) is a general formulation for the approximate total QM/MM energy function for MM subsystems with no intramolecular interactions and a QM/MM interface that does not cross chemical bonds. Addition of intramolecular interactions to the MM subsystem is trivial. The significance of this formulation is that it allows interfacing of any combination of QM and MM program packages through simple file parsers without modifying the respective source codes.

5.3.3. Potential of Mean Force of QM Coordinates

For a complex metal–water interface model, the enormous number of water degrees of freedom makes it virtually impossible to explore the full potential energy landscape with high accuracy (QM level of theory). Even if high level QM calculations were possible for such complex systems, insufficient sampling due to the finite length and time scales of currently practical simulations would impede calculation of accurate free energies. Instead, one can focus on a potential of mean force (PMF) description of the reaction system in terms of the most important degrees of freedom where contributions from less important degrees of freedom are ensemble-averaged. While solvent/water coordinates can be included in the reaction coordinate, we limit ourselves here to reaction coordinates that do not include water coordinates. As a result, the PMF is an approximation for the free energy of the QM/MM system under the mean-field and frozen QM approximation.³⁷

In order to derive a PMF description with respect to QM coordinates, we recall that the total partition function of the QM/MM system is

$$Z_T = \int \exp\{-\beta E_T(\underline{r}_{QM}, \underline{r}_{MM})\} d\underline{r}_{QM} d\underline{r}_{MM}, \quad \beta = \frac{1}{k_B T} \quad \dots(5.20)$$

Here, k_B and T are respectively the Boltzmann constant and the absolute temperature. The integration is over all QM and MM degrees of freedom. The total free energy of the system is

$$A_T = -\frac{1}{\beta} \ln(Z_T) = -\frac{1}{\beta} \ln \left[\int \exp\{-\beta E_T(\underline{r}_{QM}, \underline{r}_{MM})\} d\underline{r}_{QM} d\underline{r}_{MM} \right] \quad \dots(5.21)$$

By focusing on a selected subset of the system (i.e., the QM subsystem), we can define the PMF of the QM/MM system in terms of the QM atom conformation.

$$Z(\underline{r}_{QM}) = \int \exp\{-\beta E_T(\underline{r}_{QM}, \underline{r}_{MM})\} d\underline{r}_{MM} \quad \dots(5.22)$$

$$A(\underline{r}_{QM}) = -\frac{1}{\beta} \ln\{Z(\underline{r}_{QM})\} = -\frac{1}{\beta} \ln \left[\int \exp\{-\beta E_T(\underline{r}_{QM}, \underline{r}_{MM})\} d\underline{r}_{MM} \right]$$

Integration of this PMF in the $\{\underline{r}_{QM}\}$ space recovers the total free energy of the system.

$$A_T = -\frac{1}{\beta} \ln \left[\int \exp\{-\beta A(\underline{r}_{QM})\} d\underline{r}_{QM} \right] \quad \dots(5.23)$$

Equation (5.22) is of great utility because the configuration space of the whole reaction system is now expressed as PMF of the QM subsystem. This reduction in dimensionality of the size of QM problem is similar to the one observed in implicit solvation models. Assuming ergodicity in MD sampling, this PMF surface fully accounts for the thermodynamic contributions of the MM subsystem.³⁷ Dynamic contributions of the QM subsystem may be approximated by computing vibrational frequencies of the QM subsystem. For most heterogeneously catalyzed reactions, especially if water is not part of the reaction coordinate, periodic planewave calculations should be sufficient for this purpose.

To avoid convergence problems associated with MM sampling and to improve the computational efficiency, we perform a geometry optimization of the QM subsystem on

this PMF in a fixed ensemble of MM conformations. This procedure permits evaluation of PMF and its gradient defined within this fixed ensemble. The free energy difference between two QM conformations α and β is calculated using the free energy perturbation expression.

$$\Delta A_{\alpha \rightarrow \beta} = -\frac{1}{\beta} \ln \left\langle \exp \left\{ -\beta \left[E_T(\mathbf{r}_{\text{QM}(\beta)}, \mathbf{r}_{\text{MM}}) - E_T(\mathbf{r}_{\text{QM}(\alpha)}, \mathbf{r}_{\text{MM}}) \right] \right\} \right\rangle_{\alpha, \{\mathbf{r}_{\text{MM}}\}} \quad \dots(5.24)$$

Subscript α indicates that MM sampling is performed using the initial QM conformation and subscript $\{\mathbf{r}_{\text{MM}}\}$ indicates the use of a fixed ensemble of MM conformations. Using approximate total energy functions we obtain

$$\Delta A_{\alpha \rightarrow \beta} = -\frac{1}{\beta} \ln \left[\frac{1}{N} \sum_{\tau=1}^N \exp \{ -\beta \Delta \tilde{E}_T(\tau) \} \right] \quad \dots(5.25)$$

$$\Delta \tilde{E}_T(\tau) = \left[\tilde{E}_T(\mathbf{r}_{\text{QM}(\beta)}, \mathbf{r}_{\text{MM}}(\tau)) - \tilde{E}_T(\mathbf{r}_{\text{QM}(\alpha)}, \mathbf{r}_{\text{MM}}(\tau)) \right]_{\alpha}, \quad \tau \in \{\mathbf{r}_{\text{MM}}\}$$

Considering α as reference conformation of the QM subsystem and β as conformation of the QM subsystem at current optimization step, the gradient of Eq. (5.25) with respect to the k-th QM coordinate is

$$\frac{\partial A(\mathbf{r}_{\text{QM}})}{\partial \mathbf{r}_{\text{QM},k}} = -\frac{1}{\beta} \times \frac{\partial}{\partial \mathbf{r}_{\text{QM},k}} \ln \left[\frac{1}{N} \sum_{\tau=1}^N \exp \{ -\beta \Delta \tilde{E}_T(\tau) \} \right] \quad \dots(5.26)$$

$$\frac{\partial A(\mathbf{r}_{\text{QM}})}{\partial \mathbf{r}_{\text{QM},k}} = \frac{\sum_{\tau=1}^N \left[\exp \{ -\beta \Delta \tilde{E}_T(\tau) \} \times \frac{\partial \tilde{E}_T(\mathbf{r}_{\text{QM}}, \mathbf{r}_{\text{MM}}(\tau))}{\partial \mathbf{r}_{\text{QM},k}} \right]}{\sum_{\tau=1}^N \exp \{ -\beta \Delta \tilde{E}_T(\tau) \}} \quad \dots(5.27)$$

$$= \left\langle \frac{\partial \tilde{E}_T(\mathbf{r}_{\text{QM}}, \mathbf{r}_{\text{MM}}(\tau))}{\partial \mathbf{r}_{\text{QM},k}} \right\rangle_{\Delta \tilde{E}_T(\tau)}$$

In other words, the gradient of the PMF is simply an ensemble average of the gradients of the QM atoms and may be evaluated from the same fixed-size ensemble of MM

conformations. Substituting Eq. (5.19) in Eq. (5.27), the complete expression for gradients becomes

$$\frac{\partial A(\underline{r}_{QM})}{\partial \underline{r}_{QM,k}} = \left\{ \begin{array}{l} \frac{\partial \langle \Psi | H_{\text{eff}}(\underline{r}_{QM}, \underline{r}_{MM}^0) | \Psi \rangle}{\partial \underline{r}_{QM,k}} + \frac{\partial [E_{MM+QM/MM}^{\text{elec+vdW}}(\underline{r}_{QM}, \underline{r}_{MM}^0)]_{Q_i=0, i \in QM}}{\partial \underline{r}_{QM,k}} + \\ \left\langle \frac{\partial E_{QM+MM+QM/MM}^{\text{elec(ESP)+vdW}}(\underline{r}_{QM}, \underline{r}_{MM}(\tau))}{\partial \underline{r}_{QM,k}} \right\rangle_{\Delta \tilde{E}_T(\tau)} \\ \frac{\partial E_{QM+MM+QM/MM}^{\text{elec(ESP)+vdW}}(\underline{r}_{QM}, \underline{r}_{MM}^0)}{\partial \underline{r}_{QM,k}} \end{array} \right. \quad \dots(5.28)$$

Considering that the free energy is a state function and is therefore path independent, the total free energy change between two end states can be determined by introducing a sufficient number of intermediate states. Equation (5.24) is separately applied for each step and all such contributions are summed up. Even if the structures of such interpolated states are nonphysical, the free energy difference between the two end states will be correct. The only requirement is that the water ensembles are large enough.

5.3.4. Integration with eSMS

Currently, the challenge still remains on how to practically compute the SCF energy of a large “periodic” system immersed in a liquid phase environment. The principle idea of eSMS introduced here is based on our recent successes with iSMS. The key idea of iSMS has been to include the long range metal interactions through periodic-slab calculations within the framework of DFT calculations in the absence of a solvent and to consider the effect of solvent molecules as a localized perturbation (small or large) of free energy differences that can be described by a cluster model embedded in an implicit solvent. Specifically, we defined the free energy function for an adsorbed

reactant on a “periodic” metal slab in solvent, $A_{\text{surface+adsorbate}}^{\text{liquid}}$, using a simple subtraction scheme

$$A_{\text{surface+adsorbate}}^{\text{liquid}} = E_{\text{surface+adsorbate}}^{\text{vacuum}} - E_{\text{cluster+adsorbate}}^{\text{vacuum}} + A_{\text{cluster+adsorbate}}^{\text{liquid}} \quad \dots(5.29)$$

where $E_{\text{surface+adsorbate}}^{\text{vacuum}}$ is the planewave DFT energy of the periodic slab in vacuum, $A_{\text{cluster+adsorbate}}^{\text{liquid}}$ is the free energy in solvent of a metal cluster constructed by removing selected metal atoms from the periodic-slab model and removing the periodic boundary conditions (computed using an implicit solvation model), and $E_{\text{cluster+adsorbate}}^{\text{vacuum}}$ is the DFT energy of the same cluster in vacuum. We note that Eq. (5.29) becomes exact for an infinitely large cluster. Importantly, we found that since electrons move freely in metals, they screen electric fields very well such that converged results can be obtained for very small cluster sizes of predictable shape. In eSMS we use a similar subtraction scheme to iSMS; however, we compute $A_{\text{cluster+adsorbate}}^{\text{liquid}}$ using an explicit description of the water molecules and we do not remove any metal atoms but use a QM/MM description for the computation of $A_{\text{cluster+adsorbate}}^{\text{liquid}}$ and $E_{\text{cluster+adsorbate}}^{\text{vacuum}}$. As a result, the long range electrostatic interaction of thousands of water molecules with adsorbed reactants and transition states can be accounted for. Also, the indirect effect of water molecules on energy differences of processes on a metal surface by changing the electron density of surface metal atoms is considered as long as this interaction is short ranged. That is, it can be described with an electrostatically embedded metal cluster approach. Considering that water molecules are included only in the $A_{\text{cluster+adsorbate}}^{\text{liquid}}$ term, only the SCF energy and gradient terms in Eq. (5.19) and Eq. (5.28) need to be replaced using Eq.(5.29). That is, total QM/MM energy function and its gradient in QM/MM-FEP-eSMS formulation are given by

$$\tilde{E}_T(\underline{r}_{QM}, \underline{r}_{MM}) = \left\{ \begin{array}{l} E_{QM}^{\text{surface}}(\underline{r}_{QM}) - E_{QM}^{\text{cluster}}(\underline{r}_{QM}) + \\ \left\langle \Psi \left| H_{\text{eff}}(\underline{r}_{QM}, \underline{r}_{MM}^0) \right| \Psi \right\rangle + \left[E_{MM+QM/MM}^{\text{elec+vdW}}(\underline{r}_{QM}, \underline{r}_{MM}^0) \right]_{Q_i=0, i \in QM} + \\ E_{QM+MM+QM/MM}^{\text{elec(ESP)+vdW}}(\underline{r}_{QM}, \underline{r}_{MM}) - E_{QM+MM+QM/MM}^{\text{elec(ESP)+vdW}}(\underline{r}_{QM}, \underline{r}_{MM}^0) \end{array} \right. \dots(5.30)$$

$$\frac{\partial A(\underline{r}_{QM})}{\partial \underline{r}_{QM,k}} = \left\{ \begin{array}{l} \frac{\partial E_{QM}^{\text{surface}}(\underline{r}_{QM})}{\partial \underline{r}_{QM,k}} - \frac{\partial E_{QM}^{\text{cluster}}(\underline{r}_{QM})}{\partial \underline{r}_{QM,k}} + \frac{\partial \left\langle \Psi \left| H_{\text{eff}}(\underline{r}_{QM}, \underline{r}_{MM}^0) \right| \Psi \right\rangle}{\partial \underline{r}_{QM,k}} + \\ \frac{\partial \left[E_{MM+QM/MM}^{\text{elec+vdW}}(\underline{r}_{QM}, \underline{r}_{MM}^0) \right]_{Q_i=0, i \in QM}}{\partial \underline{r}_{QM,k}} + \\ \left\langle \frac{\partial E_{QM+MM+QM/MM}^{\text{elec(ESP)+vdW}}(\underline{r}_{QM}, \underline{r}_{MM}(\tau))}{\partial \underline{r}_{QM,k}} \right\rangle_{\Delta \tilde{E}_T(\tau)} - \\ \frac{\partial E_{QM+MM+QM/MM}^{\text{elec(ESP)+vdW}}(\underline{r}_{QM}, \underline{r}_{MM}^0)}{\partial \underline{r}_{QM,k}} \end{array} \right. \dots(5.31)$$

The first two terms in Eq. (5.30) correspond to the first two terms in Eq. (5.29) and are evaluated for a periodic slab in vacuum and a QM cluster in vacuum, respectively. All other terms in Eq. (5.30) are included following Eq. (5.19), and collectively account for QM cluster in explicit solvent. Equation (5.31) is similarly obtained by combining Eq. (5.28) and Eq. (5.29).

Next, we list a step-by-step procedure for performing geometry optimizations using eSMS. The sequential MD-sampling, QM-optimization algorithm is similar to the one developed by Hu et al.³⁸

- (1) Set optimization cycle $n=0$. Optimize the adsorbate on a periodic metal slab using planewave QM calculations.
- (2) Expand the model and add water molecules.

- (3) Equilibrate the water using MD simulation, keeping all metal and adsorbate atoms fixed at $\{\mathbf{r}_{\text{QM}}^{(0)}\}$ without any charges assigned to them. Save the last water conformation.
- (4) Select an appropriate QM cluster-in-water model containing all adsorbate atoms and only “active” metal atoms. Remaining metal atoms in the expanded periodic box and all water molecules constitute the MM subsystem.
- (5) Remove all MM water molecules and MM metal atoms from step (4) to obtain QM cluster-in-vacuum model.
- (6) Determine the lowest energy-spin state for QM cluster-in-vacuum model from step (5).
- (7) Set optimization cycle $n=n+1$. Evaluate charges of QM atoms in the electrostatic potential of reference MM conformation.
- (8) Using QM charges obtained in step (7) and keeping the QM atoms fixed at $\{\mathbf{r}_{\text{QM}}^{(n-1)}\}$, equilibrate the system using MD simulations and sample a set of MM conformations, $\{\mathbf{r}_{\text{MM}}^{(n)}(\tau), \tau=1\cdots N\}$, where N is the number of MM conformations sampled.
- (9) With the MM ensemble fixed at $\{\mathbf{r}_{\text{MM}}^{(n)}(\tau)\}$, minimize the PMF of the QM subsystem as given by Eq. (5.30). The corresponding gradient is given by Eq. (5.31). For each evaluation of QM energy or gradient, we need
 - (a) planewave QM calculation for periodic slab in vacuum (first term on RHS of Eq. (5.30)),

- (b) QM calculation for cluster-in-vacuum model using Gaussian-type orbitals (second term on RHS of Eq. (5.30)),
- (c) QM calculation and evaluation of QM charges for cluster-in-water model using Gaussian-type orbitals and a periodic electrostatic embedding scheme (third term on RHS of Eq. (5.30)),
- (d) MM calculation for reference MM conformation without any charges assigned to QM atoms (fourth term on RHS of Eq. (5.30)), and
- (e) MM calculation for each sampled conformation in $\{\mathbf{r}_{\text{MM}}^{(n)}(\boldsymbol{\tau})\}$ where the QM atoms are assigned charges as determined in step (c) (5-sixth terms on RHS of Eq. (5.30)).
- (f) Steps (a)–(d) can be performed simultaneously or sequentially in any order, but must precede step (e). The MM calculations in step (e) are independent of each other and may be performed in any arrangement, considering efficient utilization of computational resources. Coordinates of the QM atoms must remain synchronized among all QM and MM models.

(10) Go to step (7) until converged.

The main feature of this iterative algorithm (Figure 5.1) is the use of a finite, fixed-size ensemble of MM conformations for each QM optimization sequence. The PMF of QM coordinates and its gradient can be evaluated precisely within this ensemble, circumventing statistical convergence problems with MD sampling. The starting QM structure is already optimized in vacuum and should serve as an excellent initial guess for most cases. During iterative sampling/optimization cycles, each optimized QM structure serves as the reference QM structure for next cycle, and improves the one from the

previous step by providing better QM charges and total QM/MM energy. Convergence is generally obtained within a few cycles.

5.4. Computational Details

5.4.1. Periodic Planewave QM Calculations

Periodic DFT calculations were performed using the Vienna *Ab Initio* Simulation Package (VASP 5.2).⁴⁰⁻⁴¹ A planewave basis set with a cutoff energy of 400 eV and an SCF convergence criterion of 1.0×10^{-7} eV were employed for the valence electrons. Ionic core potentials were described using the projector augmented wave (PAW) method.⁴² Electron exchange and correlation effects were accounted for using the Perdew–Burke–Ernzerhof (PBE) density functional⁴³⁻⁴⁴ within the generalized gradient approximation (GGA). The Pt (111) surface was simulated using a large 4×4 unit cell with four layers of metal atoms and a vacuum of 15 Å to minimize interaction between periodically repeated images. A $4 \times 4 \times 1$ Monkhorst–Pack k-point grid⁴⁵ was employed for sampling the Brillouin zone. Dipole and quadrupole corrections to the energy were included using the modified Makov–Payne method.⁴⁶ Harris–Foulkes-type corrections for forces were included. Fractional occupancies of bands were allowed within a window of 0.10 eV using the first-order Methfessel–Paxton smearing method.⁴⁷ The bottom two Pt layers were fixed in their bulk positions. All structures were optimized to a force smaller than 0.02 eV/Å on each relaxed atom. Γ -point only, single-point energy calculations were performed for expanded surfaces and for periodic cluster models. Spin-polarization effects were taken into account for periodic cluster models. A combination of climbing-image nudged elastic band⁴⁸⁻⁴⁹ and dimer⁵⁰⁻⁵¹ methods was used for the transition state search. All minima and transition state structures were confirmed through dynamical

matrix calculations. For iSMS and eSMS calculations, the SCF energy convergence criterion was set to 1.0×10^{-8} eV.

5.4.2. Nonperiodic QM Calculations

Cluster-model calculations without periodic boundaries were performed using the TURBOMOLE 6.4 program package.⁵²⁻⁵⁵ Adsorbate atoms including water molecules were represented using all-electron basis sets of triple- ζ quality.⁵⁶⁻⁵⁷ Pt atoms were represented using relativistic small-core effective core potentials (ECPs) together with a triple- ζ quality basis set for the valence electrons.⁵⁸⁻⁵⁹ Electron exchange and correlation effects were accounted for using the PBE functional. The RI-J approximation with auxiliary basis sets was used to approximate Coulomb potentials.⁶⁰⁻⁶¹ For each QM cluster model, multiple spin states were tested using an SCF energy convergence criterion of 1.0×10^{-7} hartree and spherical grid m4.⁵⁸ For iSMS and eSMS calculations, the SCF energy convergence criterion and spherical grid were changed to 1.0×10^{-8} hartree and m5, respectively. These calculations were performed only for the lowest-energy spin state.

5.4.3. Implicit Solvation (iSMS)

For implicit solvation, COSMO^{14, 62-63} and COSMO-RS⁶⁴⁻⁶⁶ calculations were performed using radii-based cavities and a dielectric constant of infinity. The structures were first optimized in the iSMS calculations with all metal atoms fixed until the maximum force on each relaxed atom was smaller than 1.0×10^{-3} au. Only for optimized geometries, COSMO-RS calculations were performed using the COSMOtherm program.⁶⁶ Thermodynamic properties of water (solvent) were obtained from the COSMOtherm database, based on parametrization of the results of quantum chemical

COSMO calculations at the BP-TZVP level of theory. COSMO-RS input files for iSMS-optimized structures were generated from single-point COSMO calculations using B-P86 functional⁶⁷⁻⁶⁸ and TZVP basis set. All other settings are the same as described in section 5.4.2.

5.4.4. Explicit Solvation (eSMS)

QM calculations in a field of MM water molecules were performed using the periodic electrostatic embedded cluster method (PEECM)⁶⁹ with point charges taken from the TIP3P water model.⁷⁰ The periodic box used for these calculations is described in section 5.4.5. Charges on QM atoms were estimated using natural population analysis (NPA).⁷¹ ESP-fitted charges were initially used. However, considering their high computational cost,⁷² NPA charges were adopted. Approximations made in Eq. (5.8) and (5.9) were tested against QM calculations. These results are presented in section 5.5.3. All other settings are same as described in section 5.4.2.

5.4.5. Molecular Dynamics Simulations

MD simulations were performed using the DL_POLY 4.03 molecular simulation package.⁷³ The original 4×4 Pt (111) unit cell was expanded to a 16×20 lateral surface and more vacuum was added in Z-direction. The final box ($45.0 \text{ \AA} \times 48.7 \text{ \AA} \times 50.0 \text{ \AA}$) contained 1280 Pt atoms. Any additional adsorbates created by this expansion were deleted. The simulation box was filled with 2250 water molecules to obtain a liquid density of 0.83 g/cm^3 , approximately the density of saturated liquid water at 500 K. All Pt and adsorbate atoms were kept fixed, whereas the water molecules were constrained to TIP3P geometry using the SHAKE algorithm.⁷⁴ Simulations were performed in a canonical (NVT) ensemble with Berendsen thermostat⁷⁵ using a relaxation constant of

0.01 ps. Smoothed Particle Mesh Ewald (SPME) method⁷⁶ with a cutoff of 10 Å was employed for electrostatic interactions. The same cutoff was used for van der Waals interactions. A time step of 1 fs was used. The system was first equilibrated for 100 ps. Then, an ensemble of 10 000 MM conformations was generated by recording every 10th conformation from an additional 100 ps of simulation.

Force field parameters for water were taken from the TIP3P model. For the Pt–water interaction, the Spohr–Heinzinger potential⁷⁷ was implemented in the DL_POLY source code. Only van der Waals’ parameters for adsorbate (ethylene glycol) atoms were taken from the OPLS force field,⁷⁸⁻⁷⁹ whereas charges for these atoms were obtained from the QM calculations as described in section 5.4.4. For Pt atoms that are included in the QM cluster, NPA charges obtained from QM calculations were used; other Pt atoms were not assigned any charge. We note that there is hardly any charge transfer between liquid water and the metal surface and the computed charges on the metal atoms are very small.⁷² As a result, the Spohr–Heinzinger potential does in effect not contain any electrostatic interaction such that the electrostatic interaction computed by NPA charges on the metal atoms does not lead to overcounting of any interactions. We nevertheless had to include the NPA charges on the metal atoms to ensure overall charge neutrality of our reaction system. Lorentz–Berthelot mixing rules are used for Lennard–Jones interaction parameters between adsorbed ethylene glycol species and the TIP3P water molecules.

5.4.6. Implementation of iSMS and eSMS

The algorithm listed in section 5.3.4 has been implemented using a set of FORTRAN programs. Of particular importance are programs that calculate the SCF

energy and gradients for a given structure using the iSMS and eSMS methods. These programs replace standard SCF energy and gradient routines and may be called from any external optimizer without knowledge of implementation details. A modular approach has been adopted in program design such that a new QM or MM package can be integrated by simply including respective input/output file parsing routines. Using predefined templates and a set of keywords for the specific task, input files for all QM and MM programs are automatically generated. The job resource manager then executes the respective binaries in the order described in section 5.3.4. Synchronization of QM coordinates among all programs is guaranteed at all times. When calculations are finished, all output files are automatically processed to extract required information.

5.5. Results and Discussion

C–C cleavage in double-dehydrogenated ethylene glycol, with one H atom removed from each C atom, has been used as a model reaction for this study.



The choice of this reaction has been influenced by a number of factors. First, the focus of this study is to develop and validate a theoretical method to account for solvent effects on elementary processes occurring at metal surfaces relevant for liquid phase processing of lignocellulosic biomass model molecules. Although the eSMS formulation allows water molecules to be treated as part of the reaction coordinate, such a system is beyond the scope of this study. Second, FEP calculations with finite configuration space sampling require significant overlap in importance of initial and final state configurations. This can be achieved by splitting the reaction coordinate into a number of small FEP windows. A very high activation barrier or a geometrically complex reaction coordinate would

become computationally prohibitive. At the same time, if the activation barrier is too low, the PMF procedure might not be valid and it would be difficult to characterize the effect of water. Partial dehydrogenation of both C atoms ensures that all structures involved in the selected reaction coordinate bind to the Pt (111) surface sufficiently strongly resulting in a moderately high activation barrier. We avoided complete dehydrogenation which would result in a very small activation barrier. Finally, the initial state contains two –OH groups on adjacent C atoms, a characteristic feature of biomass-derived polyols, and thus serves well our long-term goal of modeling aqueous-phase processing of such molecules.

5.5.1. Convergence of eSMS

For practical applications, the eSMS energy function must converge for clusters of small size and predictable shape. For the iSMS method, we have previously shown that a two-layer QM cluster including metal atoms forming the adsorption site and their nearest neighbors should be sufficient.¹⁷ The results of a similar convergence test with explicit QM water molecules are presented here.

In its most stable configuration, CHOH-CHOH is adsorbed on a bridge site with each C atom binding to one Pt atom. A hydrogen bond is formed between the two –OH groups (Figure 5.2(a)). C–C cleavage results in formation of two CHOH fragments that are coadsorbed on the same slab. Multiple coadsorption sites were tested and the lowest-energy combination was found to involve two adjacent bridge sites (Figure 5.2(b)). In all cases, C atoms satisfy their tetrahedral bonding geometries.

For explicit solvation, seven water molecules of TIP3P geometry were “randomly” placed around the adsorbates. To avoid large changes in water–water and water–metal interaction, the same configuration of water molecules was used for both the

initial and final states. The original 4×4 unit cell was expanded to a 12×12 unit cell and any additional adsorbates and water molecules created by this expansion were removed. For this convergence test, it is necessary to disrupt the formation of a continuous hydrogen bonding network that cannot be reproduced in nonperiodic QM calculations described in section 5.4.2. Planewave calculations estimate $\Delta E_{\text{surface,rxn}}^{\text{water}} = 0.23$ eV and $\Delta E_{\text{surface,rxn}}^{\text{vacuum}} = 0.14$ eV. That is, the reaction becomes endothermic by 0.09 eV in the presence of water. These values are used as reference for analyzing the performance of the eSMS method for various QM clusters.

Next, QM clusters were carved out from the expanded slabs. We have considered four types of clusters in terms of size of their lateral surface area (Figure 5.3). For each type, 1–4 layers of Pt atoms were considered. Figure 5.4 confirms the smooth and rapid convergence of eSMS as a function of lateral size and depth of the QM clusters. Clusters of type “a” clearly fail to include some Pt atoms that are in direct vicinity to the adsorbate. These clusters are not useful regardless of their thickness. Two- and three-layer clusters of type “b” contain the same number of atoms as three- and four-layer clusters of type “a”, respectively. However, because all Pt atoms in close proximity to the adsorbate are now included, these clusters are able to meet a tolerance of ± 0.02 eV. All clusters of types “c” and “d” produce excellent agreement with the reference calculation.

Figure 5.4 also emphasizes the importance of long range metal interactions. When eSMS is not used, even the largest clusters fail to match the results of the periodic slab calculations and there is no smooth convergence pattern. This behavior is expected because it just illustrates the reasons why periodic models are commonly used for metallic systems. On the other hand, when these interactions are included using eSMS, all

four types of clusters show smooth convergence with increasing size clearly illustrating that the indirect effect of water molecules on energy differences of processes on a metal surface by changing the electron density of surface metal atoms is short ranged as required for eSMS.

5.5.2. Integration of Periodic and Nonperiodic QM Calculations

To test the integration of periodic (planewave basis) and nonperiodic (Gaussian-type basis) QM calculations, TURBOMOLE calculations have been performed for selected two-layer clusters with and without water molecules. All water molecules are assigned the same basis sets as other adsorbate atoms in the system. Figure 5.5 shows that, when using the eSMS method, results obtained from our integrated calculations are in good agreement with pure planewave calculations. We again see that the smallest cluster that is able to satisfy the specified tolerance in all cases is a 35-atom, two-layer cluster of type “b”. It agrees with all our previous conclusions, because (i) all metal atoms directly involved in bonding and their nearest neighbors are included and (ii) there are at least two layers of Pt atoms. These conclusions hold even when a smaller basis set is used. We have previously shown that the iSMS method also converges for small basis sets.¹⁷

5.5.3. Validation of Approximate Total QM/MM Energy Function

In order to test the effectiveness of fixed-charge approximation made in Eq. (5.8), we have compared the results obtained from Eq. (5.19) against *ab initio* QM calculations. As a test case, we have considered the initial state (CHOH-CHOH) adsorbed on a two-layer, 51-atom cluster (Figure 5.6). The simulation box contains a total of 1280 Pt atoms and 2250 TIP3P water molecules. This QM cluster is an intermediate between the

35- and 70-atom clusters (Figure 5.5). Although we have already demonstrated the usefulness of the 35-atom cluster for this particular reaction, considering that our long-term goal is modeling the aqueous phase reforming mechanism of ethylene glycol and glycerol, and noting that the 35-atom cluster may not be sufficient for some of the larger multidentate intermediates in these mechanisms, a larger 51-atom cluster was chosen for all further studies. This particular QM cluster satisfies all previously listed requirements for all elementary reactions in these mechanisms.

After filling the simulation box with water molecules, the system was equilibrated for 100 ps. The objective is to obtain a reasonable water conformation that can be used for evaluation of NPA (natural population analysis)⁷¹ charges on the QM atoms. Using the last water conformation from this simulation, periodic electrostatic embedded cluster method (PEECM)⁶⁹ calculations were performed and NPA charges for the QM atoms were determined. These charges were updated in the MM force field, and the system was again equilibrated for 100 ps. From the next 100 ps of MD simulation, 50 water conformations, 2 ps apart, were recorded.

For each of these 50 conformations, the QM energy was obtained from PEECM calculations. In other words, each sampled conformation was treated as a reference MM conformation. Equation (5.19) for this case reduces to

$$E_T(\mathbf{r}_{QM}, \mathbf{r}_{MM}^0) = \langle \Psi | H_{\text{eff}}(\mathbf{r}_{QM}, \mathbf{r}_{MM}^0) | \Psi \rangle + \left[E_{MM+QM/MM}^{\text{elec+vdW}}(\mathbf{r}_{QM}, \mathbf{r}_{MM}^0) \right]_{Q_i=0, i \in QM} \quad \dots(5.33)$$

Only those electrostatic and van der Waals interactions need to be included in the MM force field that are not accounted for by the PEECM calculations. No NPA fitted charges are required for the QM atoms. We then perturbed the QM atom geometry characteristic

of an FEP step and recalculated the QM energies for the same fixed ensemble of 50 conformations.

Total QM/MM energies for both initial and perturbed QM geometries were also estimated by application of Eq. (5.19); that is, making the fixed-charge approximation. PEECM calculations were performed only for one water conformation and the QM energy and NPA charges obtained from this calculation were used to approximate \tilde{E}_T for all other conformations. Figure 5.7 shows that the energy differences obtained using the fixed-charge approximation are in good agreement with those obtained from *ab initio* calculations. If the free energy difference is estimated from these data sets using the FEP procedure, the error is smaller than 5 meV (6%).

5.5.4. Optimization of Reactant, Product, and Transition States

Optimizations of reactant, product, and transition states were performed using the QM/MM-FEP algorithm described in section 5.3.4. Structures obtained from planewave calculations on the Pt (111) slab were used as starting points. Each optimization cycle started with a 200 ps MD simulation which includes 100 ps of equilibration. An ensemble of 10 000 MM water conformations was recorded in this step. The structures were then optimized in this fixed ensemble with all metal atoms fixed until the maximum force on each relaxed atom was smaller than 1.0×10^{-3} au. QM atom conformations and NPA charges thus obtained were used in the next cycle of MD sampling and QM atom optimization. All optimizations were carried out using the def2-SVP basis set and PBE functional.

Convergence of relative free energies over a number of optimization cycles is shown in Figure 5.8. There is a negligible effect of water on the transition state. The

products state is stabilized in water by 1.8 kJ/mol. The reactant state is most affected by the presence of water as it is stabilized by 9.3 kJ/mol. Structural changes observed during these optimizations are summarized in Table 5.1. These changes, however small, are consistent in all cases: C–Pt bond is shortened whereas C–O, C–H, and O–H bonds are elongated. Changes observed for C–O and O–H bonds are noticeably larger than for C–H bonds. The most significant effect of water is observed for the intramolecular hydrogen bond in the reactant state that is elongated by 0.24 Å. This change is caused by rotation of one –OH group (H of hydrogen bond) away from the other –OH group toward the surface, in a direction similar to the transition and product states. The torsional angle between the two –OH groups is changed by 28°.

For comparison, we also performed these optimizations using the iSMS method starting from the same initial structures. All optimizations were carried out using the def2-SVP basis set and PBE functional. Single-point energy calculations were performed for the optimized structures using TZVP basis set and B-P86 functional to generate input files for COSMO-RS. The reactant, product, and transition state structures were stabilized in the presence of water by 2.4, 0.3, and 0.3 kJ/mol, respectively. All bond length changes are negligible. The torsional angle between the two –OH groups is changed by only 2° and the resultant increase in the length of hydrogen bond is 0.03 Å. This inconsistency between iSMS and eSMS results is not surprising since such site-specific interactions are difficult to describe with implicit solvation models.

5.5.5. Free Energy Profile

With three states known on the reaction coordinate, a complete free energy profile was constructed by inserting intermediate states. To obtain a smooth potential energy

surface, atomic overlaps introduced by linear interpolation were removed. For this purpose, selective geometry optimizations were performed for these intermediate states by fixing both C atoms at the interpolated coordinates. O and H atoms of the adsorbates were relaxed for 20 steps. These optimizations were not pursued to convergence. Considering that the thermal energy ($k_B T$) at 500 K is 0.043 eV, more intermediate states were introduced where necessary to ensure that no two adjacent images differ in energy by more than this value. In the end, there were 41 intermediate states between the reactant and transition state and 34 intermediate states between the product and transition state. QM/MM-FEP calculations were performed for all such windows to obtain the complete free energy profile (Figure 5.9). A summary of our results that includes vibrational contributions to the free energy of the stationary points is presented in Table 5.2.

For eSMS-optimized structures, frequency calculations were performed using numerical gradients and central differences with a step size of 0.02 au. These calculations assumed nonequilibrium solvation, that is, the vibrations of the QM subsystem occur at a time scale that does not allow reorientation of the surrounding water environment. For all other cases reported in Table 5.2, gas-phase frequencies obtained from periodic-slab calculations were used to calculate vibrational contributions to the free energy.

Results obtained from both iSMS and eSMS are in good qualitative agreement. The reaction becomes more endothermic in the presence of water by about 10 kJ/mol. The activation barrier also increases by 10–20 kJ/mol. The effect of water in all cases can be traced back to a strong effect of water on the reactant state. Larger changes are

predicted in water when using explicit solvent molecules and can be attributed to larger structural changes, especially in hydrogen bonding.

5.5.6. Computational Efficiency

The total MD simulation time for the free energy profile shown in Figure 5.9 exceeds 25 ns. This is almost 3 orders of magnitude longer than any previously reported *ab initio* MD simulation for metal surfaces. The total computational cost to obtain the complete FEP profile (including QM/MM-FEP optimization) is however only about 25 times that of gas-phase planewave calculations for the structures (reactant, product, and transition state). This is a significant improvement since the effect of an aqueous environment is correctly captured at a computational cost that should be affordable, at least for those elementary reactions in a mechanism that are likely most affected by water.

5.6. Conclusions

Direct application of *ab initio* molecular dynamics (MD) methods for simulation of transition metal-catalyzed reactions in an aqueous environment is limited by the enormous computational cost of sampling the configuration space of such large and complex systems in a statistically relevant manner. Force field based MD simulations can adequately address the issue of configuration space sampling, but often fail to capture electronic structure changes associated with bond breaking and forming processes. Hybrid QM/MM methods offer a computationally efficient alternative and have been successfully demonstrated for numerous aqueous-phase reaction systems.

In this work, we have adopted the QM/MM-FEP method for simulation of chemical reactions at metal–water interfaces. The reaction process is modeled with our

eSMS methodology that combines computations on a periodic metal slab with calculations of a finite QM metal cluster placed in a large MM water box. Long range metal interactions are included by the periodic planewave calculations and all water effects are accounted for by the cluster model computations. Expressions for the PMF of the QM subsystem and gradient of this PMF have been derived within the QM/MM-FEP-eSMS framework. Geometry optimizations on this PMF surface are performed iteratively with sequential MD-sampling and QM atom optimization steps. A fixed-size ensemble of MM conformations is used to improve the precision of QM energy and gradient evaluations resulting in faster convergence. On-the-fly QM calculations are avoided by using the fixed-charge approximation for the QM/MM electrostatic interactions. We found this approximation to be very good for metallic systems. An overall speedup of multiple orders of magnitude is achieved compared to *ab initio* MD simulations.

We have demonstrated that this novel solvation scheme (eSMS) converges quickly both with size of QM cluster and basis set. Effectiveness of this new approach is illustrated by modeling the C–C bond cleavage reaction in dehydrogenated ethylene glycol at the Pt(111)/H₂O interface. Gas-phase structures of reactant, product and transition state are first optimized in water; then, the complete free energy profile for the reaction coordinate is obtained by inserting intermediate states and calculating free energy differences between adjacent states. It is shown that the reactant state is disproportionately stabilized in water, and the effect can be correlated with changes in intramolecular hydrogen bonding. Results obtained from an implicit solvation scheme are in good agreement.

5.7. References

1. Rossmeisl, J.; Logadottir, A.; Norskov, J. K. *Chem. Phys.* **2005**, *319*, 178–184.
2. D'Agostino, C.; Brett, G. L.; Miedziak, P. J.; Knight, D. W.; Hutchings, G. J.; Gladden, L. F.; Mantle, M. D. *Chem. -Eur. J.* **2012**, *18*, 14426–14433.
3. Roudgar, A.; Eikerling, M.; van Santen, R. *Phys. Chem. Chem. Phys.* **2010**, *12*, 614–620.
4. Hou, R. J.; Wang, T. F.; Lan, X. C. *Ind. Eng. Chem. Res.* **2013**, *52*, 13305–13312.
5. Hibbitts, D. D.; Loveless, B. T.; Neurock, M.; Iglesia, E. *Angew. Chem., Int. Ed.* **2013**, *52*, 12273–12278.
6. Okamoto, Y. *Chem. Phys. Lett.* **2005**, *405*, 79–83.
7. Okamoto, Y. *Chem. Phys. Lett.* **2006**, *429*, 209–213.
8. Iftimie, R.; Minary, P.; Tuckerman, M. E. *Proc. Natl. Acad. Sci. U.S.A.* **2005**, *102*, 6654–6659.
9. Mattsson, T. R.; Paddison, S. J. *Surf. Sci.* **2003**, *544*, L697–L702.
10. Otani, M.; Hamada, I.; Sugino, O.; Morikawa, Y.; Okamoto, Y.; Ikeshoji, T. *Phys. Chem. Chem. Phys.* **2008**, *10*, 3609–3612.
11. Yang, J.; Dauenhauer, P. J.; Ramasubramaniam, A. *J. Comput. Chem.* **2013**, *34*, 60–66.
12. Cramer, C. J.; Truhlar, D. G. *Chem. Rev.* **1999**, *99*, 2161–2200.
13. Tomasi, J.; Mennucci, B.; Cammi, R. *Chem. Rev.* **2005**, *105*, 2999–3093.
14. Klamt, A.; Schuurmann, G. *J. Chem. Soc., Perkin Trans. 2* **1993**, 799–805.
15. Jacob, T.; Goddard, W. A. *ChemPhysChem* **2006**, *7*, 992–1005.
16. Wang, H. F.; Liu, Z. P. *J. Phys. Chem. C* **2009**, *113*, 17502–17508.
17. Faheem, M.; Suthirakun, S.; Heyden, A. *J. Phys. Chem. C* **2012**, *116*, 22458–22462.
18. Behtash, S.; Lu, J. M.; Faheem, M.; Heyden, A. *Green Chem.* **2014**, *16*, 605–616.
19. Toney, M. F.; Howard, J. N.; Richer, J.; Borges, G. L.; Gordon, J. G.; Melroy, O. R.; Wiesler, D. G.; Yee, D.; Sorensen, L. B. *Nature* **1994**, *368*, 444–446.
20. Henderson, M. A. *Surf. Sci. Rep.* **2002**, *46*, 1–308.
21. Hodgson, A.; Haq, S. *Surf. Sci. Rep.* **2009**, *64*, 381–451.
22. Cao, D.; Lu, G. Q.; Wieckowski, A.; Wasileski, S. A.; Neurock, M. *J. Phys. Chem. B* **2005**, *109*, 11622–11633.
23. Zope, B. N.; Hibbitts, D. D.; Neurock, M.; Davis, R. J. *Science* **2010**, *330*, 74–78.
24. Senn, H. M.; Thiel, W. *Angew. Chem., Int. Ed.* **2009**, *48*, 1198–1229.
25. Meng, S.; Wang, E. G.; Gao, S. W. *Phys. Rev. B* **2004**, *69*, 195404.
26. Torrie, G. M.; Valleau, J. P. *J. Comput. Phys.* **1977**, *23*, 187–199.
27. Straatsma, T. P.; Berendsen, H. J. C. *J. Chem. Phys.* **1988**, *89*, 5876–5886.
28. Riccardi, D.; Schaefer, P.; Yang, Y.; Yu, H. B.; Ghosh, N.; Prat-Resina, X.; Konig, P.; Li, G. H.; Xu, D. G.; Guo, H.; Elstner, M.; Cui, Q. *J. Phys. Chem. B* **2006**, *110*, 6458–6469.
29. Kastner, J.; Senn, H. M.; Thiel, S.; Otte, N.; Thiel, W. *J. Chem. Theory Comput.* **2006**, *2*, 452–461.
30. Hu, H.; Yang, W. T. *Annu. Rev. Phys. Chem.* **2008**, *59*, 573–601.
31. Zwanzig, R. W. *J. Chem. Phys.* **1954**, *22*, 1420–1426.
32. Senn, H. M.; Thiel, W. *Top. Curr. Chem.* **2007**, *268*, 173–290.
33. Field, M. J.; Bash, P. A.; Karplus, M. *J. Comput. Chem.* **1990**, *11*, 700–733.

34. Zhang, Y. K.; Lee, T. S.; Yang, W. T. *J. Chem. Phys.* **1999**, *110*, 46–54.
35. Murphy, R. B.; Philipp, D. M.; Friesner, R. A. *Chem. Phys. Lett.* **2000**, *321*, 113–120.
36. Lu, Z. Y.; Yang, W. T. *J. Chem. Phys.* **2004**, *121*, 89–100.
37. Hu, H.; Lu, Z. Y.; Yang, W. T. *J. Chem. Theory Comput.* **2007**, *3*, 390–406.
38. Hu, H.; Lu, Z. Y.; Parks, J. M.; Burger, S. K.; Yang, W. T. *J. Chem. Phys.* **2008**, *128*, 034105.
39. Hu, H.; Yang, W. T. *J. Mol. Struct.: THEOCHEM* **2009**, *898*, 17–30.
40. Kresse, G.; Furthmuller, J. *Comput. Mater. Sci.* **1996**, *6*, 15–50.
41. Kresse, G.; Furthmuller, J. *Phys. Rev. B* **1996**, *54*, 11169–11186.
42. Kresse, G.; Joubert, D. *Phys. Rev. B* **1999**, *59*, 1758–1775.
43. Perdew, J. P.; Burke, K.; Ernzerhof, M. *Phys. Rev. Lett.* **1996**, *77*, 3865–3868.
44. Perdew, J. P.; Burke, K.; Ernzerhof, M. *Phys. Rev. Lett.* **1997**, *78*, 1396–1396 Erratum.
45. Monkhorst, H. J.; Pack, J. D. *Phys. Rev. B* **1976**, *13*, 5188–5192.
46. Makov, G.; Payne, M. C. *Phys. Rev. B* **1995**, *51*, 4014–4022.
47. Methfessel, M.; Paxton, A. T. *Phys. Rev. B* **1989**, *40*, 3616–3621.
48. Henkelman, G.; Uberuaga, B. P.; Jonsson, H. *J. Chem. Phys.* **2000**, *113*, 9901–9904.
49. Henkelman, G.; Jonsson, H. *J. Chem. Phys.* **2000**, *113*, 9978–9985.
50. Henkelman, G.; Jonsson, H. *J. Chem. Phys.* **1999**, *111*, 7010–7022.
51. Heyden, A.; Bell, A. T.; Keil, F. J. *J. Chem. Phys.* **2005**, *123*, 224101.
52. TURBOMOLE V6.4 2012, a development of University of Karlsruhe and Forschungszentrum Karlsruhe GmbH, 1989–2007, TURBOMOLE GmbH, since 2007.
53. Ahlrichs, R.; Bar, M.; Haser, M.; Horn, H.; Kolmel, C. *Chem. Phys. Lett.* **1989**, *162*, 165–169.
54. Treutler, O.; Ahlrichs, R. *J. Chem. Phys.* **1995**, *102*, 346–354.
55. Von Arnim, M.; Ahlrichs, R. *J. Comput. Chem.* **1998**, *19*, 1746–1757.
56. Schafer, A.; Horn, H.; Ahlrichs, R. *J. Chem. Phys.* **1992**, *97*, 2571–2577.
57. Schafer, A.; Huber, C.; Ahlrichs, R. *J. Chem. Phys.* **1994**, *100*, 5829–5835.
58. Eichkorn, K.; Weigend, F.; Treutler, O.; Ahlrichs, R. *Theor. Chem. Acc.* **1997**, *97*, 119–124.
59. Weigend, F.; Ahlrichs, R. *Phys. Chem. Chem. Phys.* **2005**, *7*, 3297–3305.
60. Eichkorn, K.; Treutler, O.; Ohm, H.; Haser, M.; Ahlrichs, R. *Chem. Phys. Lett.* **1995**, *240*, 283–290.
61. Weigend, F. *Phys. Chem. Chem. Phys.* **2006**, *8*, 1057–1065.
62. Klamt, A.; Jonas, V. *J. Chem. Phys.* **1996**, *105*, 9972–9981.
63. Schafer, A.; Klamt, A.; Sattel, D.; Lohrenz, J. C. W.; Eckert, F. *Phys. Chem. Chem. Phys.* **2000**, *2*, 2187–2193.
64. Klamt, A. *J. Phys. Chem.* **1995**, *99*, 2224–2235.
65. Klamt, A.; Jonas, V.; Burger, T.; Lohrenz, J. C. W. *J. Phys. Chem. A* **1998**, *102*, 5074–5085.
66. Klamt, A. *COSMO-RS: From Quantum Chemistry to Fluid Phase Thermodynamics and Drug Design*. Elsevier Science Ltd.: Amsterdam, The Netherlands, 2005.
67. Perdew, J. P. *Phys. Rev. B* **1986**, *33*, 8822–8824.
68. Becke, A. D. *Phys. Rev. A* **1988**, *38*, 3098–3100.
69. Burow, A. M.; Sierka, M.; Dobler, J.; Sauer, J. *J. Chem. Phys.* **2009**, *130*, 174710.
70. Jorgensen, W. L.; Chandrasekhar, J.; Madura, J. D.; Impey, R. W.; Klein, M. L. *J. Chem. Phys.* **1983**, *79*, 926–935.

71. Reed, A. E.; Weinstock, R. B.; Weinhold, F. *J. Chem. Phys.* **1985**, *83*, 735–746.
72. See Appendix B for comparison of invariability and computational cost of ESP-fitted and NPA charges.
73. Todorov, I. T.; Smith, W.; Trachenko, K.; Dove, M. T. *J. Mater. Chem.* **2006**, *16*, 1911–1918.
74. Smith, W.; Forester, T. R. *Comput. Phys. Commun.* **1994**, *79*, 63–77.
75. Berendsen, H. J. C.; Postma, J. P. M.; Vangunsteren, W. F.; Dinola, A.; Haak, J. R. *J. Chem. Phys.* **1984**, *81*, 3684–3690.
76. Essmann, U.; Perera, L.; Berkowitz, M. L.; Darden, T.; Lee, H.; Pedersen, L. G. *J. Chem. Phys.* **1995**, *103*, 8577–8593.
77. Spohr, E. *J. Phys. Chem.* **1989**, *93*, 6171–6180.
78. Jorgensen, W. L. *J. Phys. Chem.* **1986**, *90*, 1276–1284.
79. Geerke, D. P.; Van Gunsteren, W. F. *Mol. Phys.* **2007**, *105*, 1861–1881.

Table 5.1. Structural changes in the presence of water for reactant, product, and transition state.^a

Bond	Reactant	Product	Transition state
C-Pt	-0.036	-0.037	-0.022
C-C	+0.005		+0.024
C-O	+0.016	+0.030	+0.007
C-H	+0.002	+0.001	+0.002
O-H	+0.011	+0.001	+0.004
O-H (hydrogen bond)	+0.237		

^a Changes (Å) are measured after 4 cycles of QM/MM-FEP optimization relative to planewave-optimized structures on a Pt (111) slab. For multiple bonds of same type, only average changes are reported.

Table 5.2. Effect of water on reaction free energy and activation barrier.^a

	Activation barrier (eV)	Reaction energy (eV)
VASP – Pt (111) slab	+1.04	+0.05
eSMS (gas-phase structures)	+1.20	+0.12
eSMS (optimized in water)	+1.25	+0.15
iSMS (gas-phase structures)	+1.13	+0.15
iSMS (optimized in water)	+1.15	+0.16

^a For gas-phase and iSMS-optimized structures vibrational frequencies are calculated in the gas phase (as it is common for COSMO-RS calculations). For eSMS-optimized structures, vibrational frequencies are computed assuming molecular vibrations occur on a time scale that does not allow reorientation of the solvent molecules.

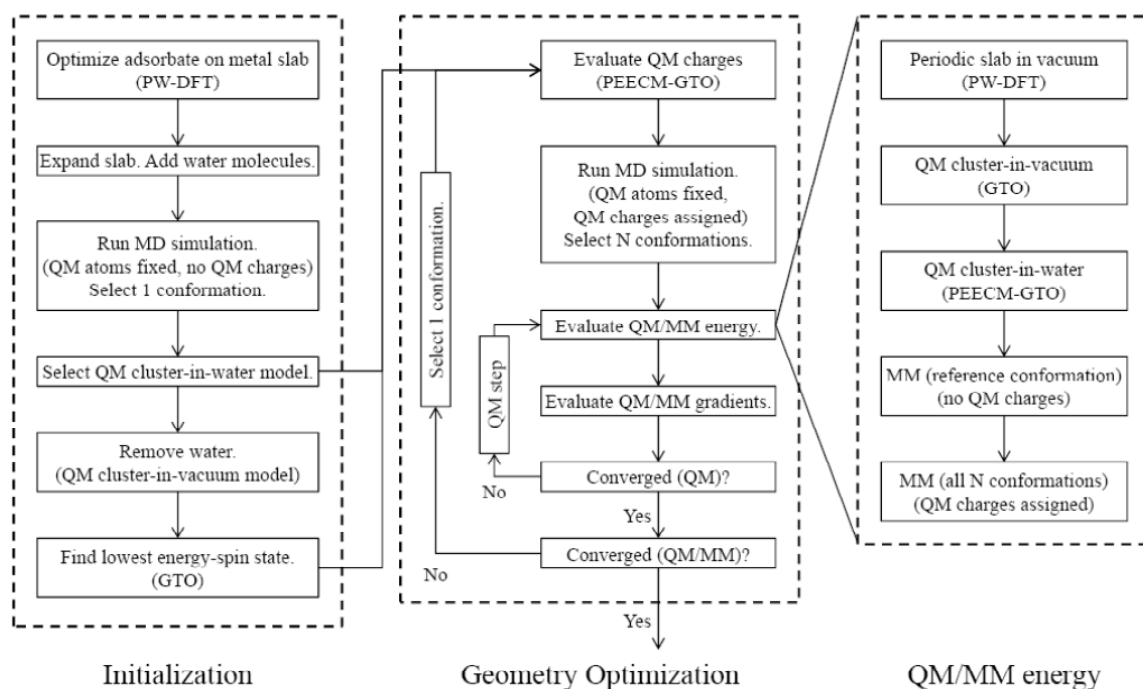


Figure 5.1. Algorithm for geometry optimization using eSMS method. Abbreviations used for QM methods are PW (planewave), GTO (Gaussian-type orbitals), and PEECM (periodic electrostatic embedded cluster method).

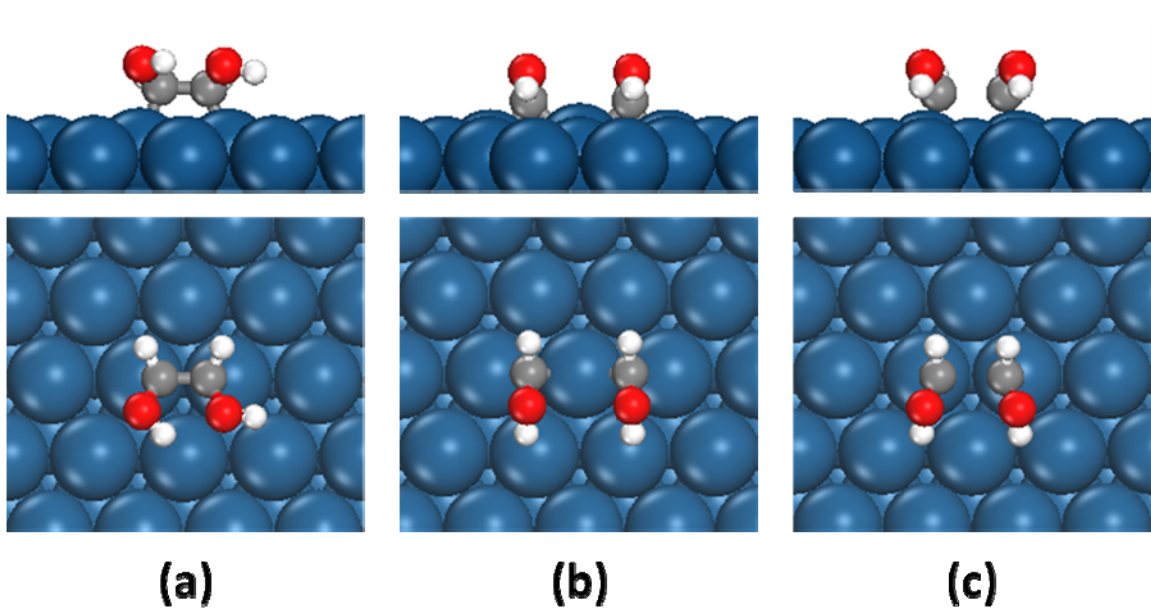


Figure 5.2. Side (upper panel) and top (lower panel) views of optimized structures on Pt (111) slab in vacuum: (a) reactant, (b) coadsorbed products, and (c) transition state for the reaction $\text{CHOH} - \text{CHOH} \rightarrow 2(\text{CHOH})$.

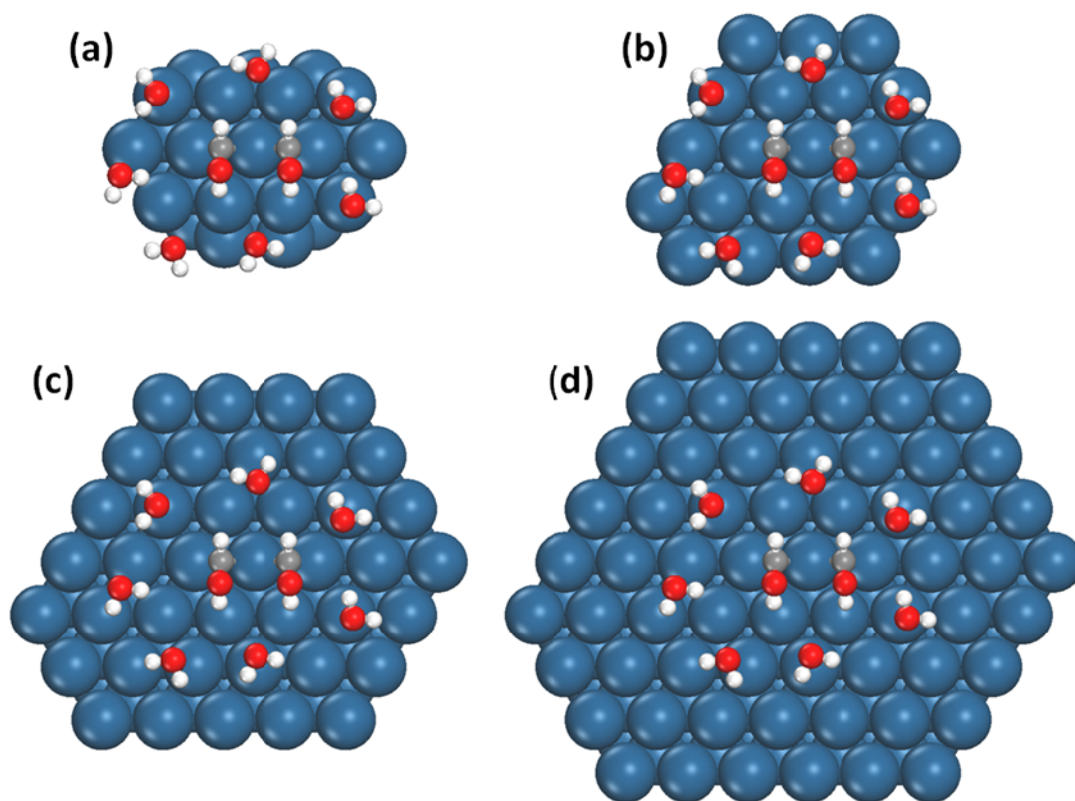


Figure 5.3. QM clusters selected for convergence test of eSMS with respect to cluster size: final state with 7 water molecules is shown. (a) Cluster contains Pt atoms directly bound to CHO species and their nearest neighbors. (b) Cluster contains all Pt atoms of cluster “a” plus addition rows of Pt atoms involved in screening the Pt atoms that form chemical bounds to CHO species. (c) Cluster contains all Pt atoms of cluster “b” plus an additional ring of Pt atoms. (d) Benchmark cluster model.

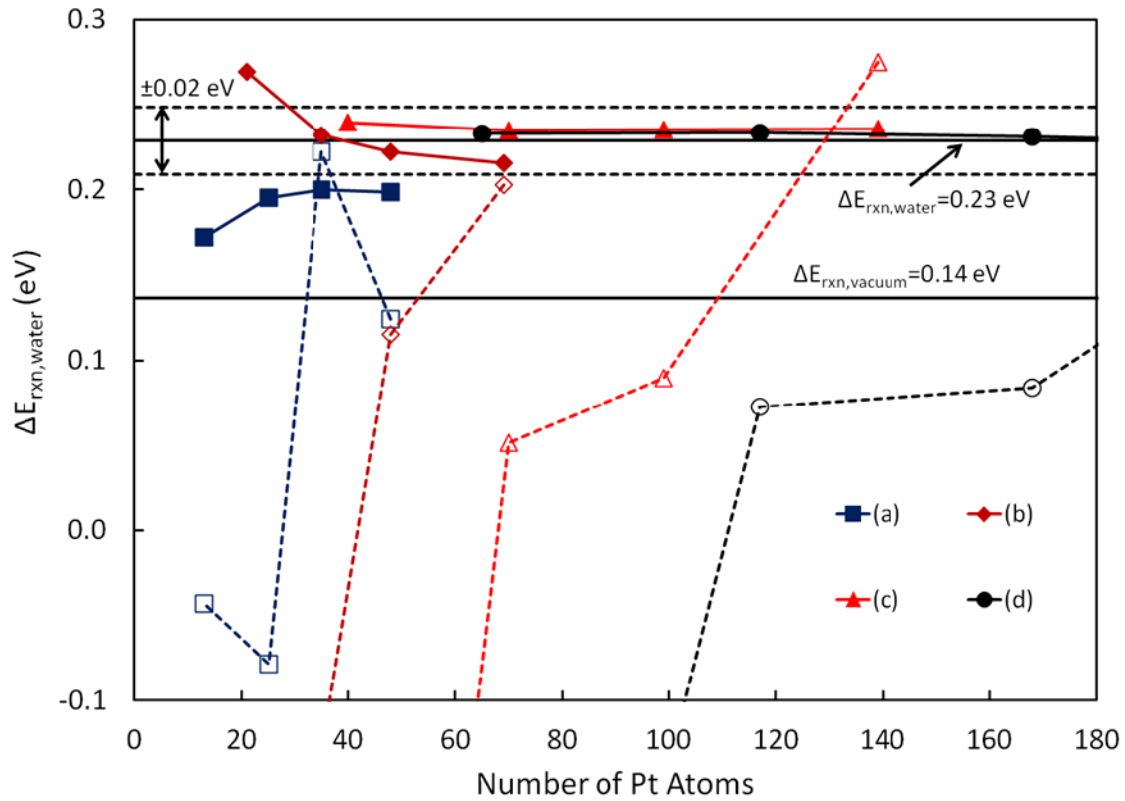


Figure 5.4. Convergence of eSMS with size of QM cluster (computed with VASP 5.2). Solid horizontal lines show reference values for $\Delta E_{\text{surface,rxn}}^{\text{water}}$ and $\Delta E_{\text{surface,rxn}}^{\text{vacuum}}$ for a $12 \times 12 \times 4$ Pt (111) slab. Dashed horizontal lines mark a tolerance of ± 0.02 eV about $\Delta E_{\text{surface,rxn}}^{\text{water}}$. Solid lines with filled markers are eSMS results for the four types of QM clusters shown in Figure 5.3. Dashed lines with hollow markers are corresponding results for $\Delta E_{\text{cluster,rxn}}^{\text{water}}$ without using eSMS. For each cluster type, 1–4 layer thick clusters are considered. 233-atom, 4-layer cluster of type “d” is not shown on this scale.

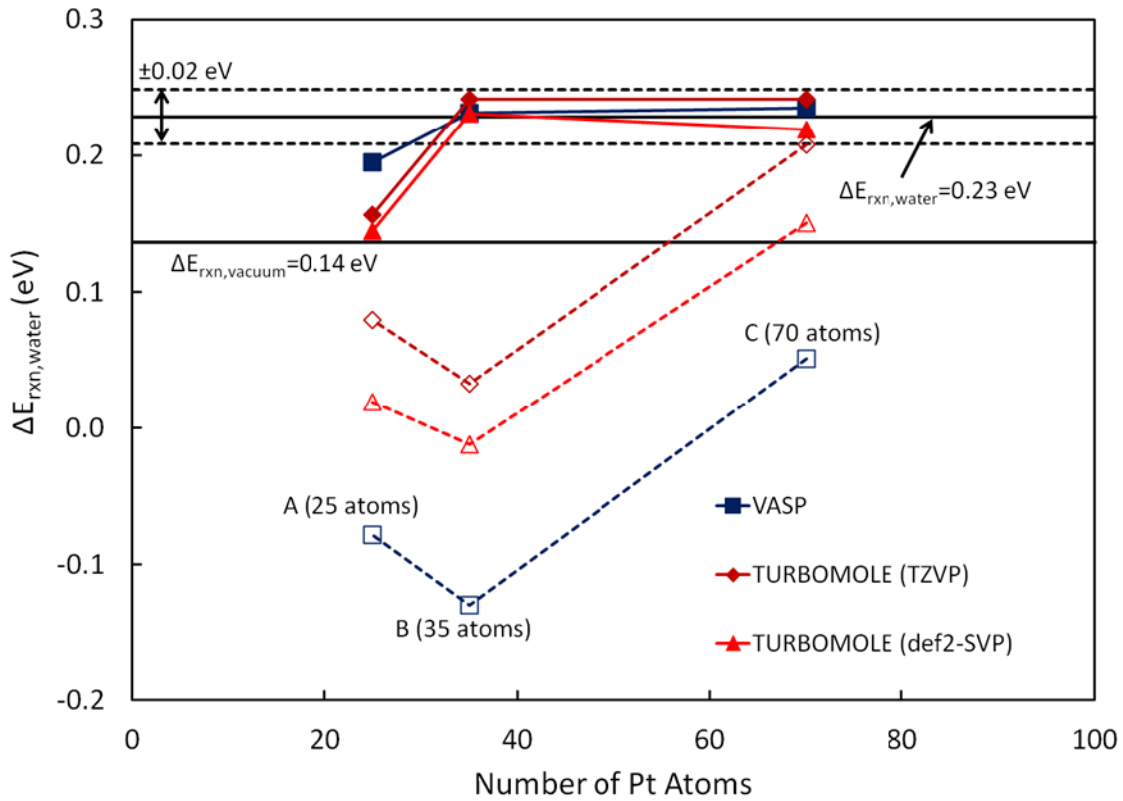


Figure 5.5. Convergence of eSMS with size of QM cluster (periodic planewave QM calculations integrated with nonperiodic QM calculations). Solid horizontal lines show reference values of $\Delta E_{\text{surface,rxn}}^{\text{water}}$ and $\Delta E_{\text{surface,rxn}}^{\text{vacuum}}$ for a $12 \times 12 \times 4$ Pt (111) slab. Dashed horizontal lines mark a tolerance of ± 0.02 eV around $\Delta E_{\text{surface,rxn}}^{\text{water}}$. Solid lines with filled markers are eSMS results for two layer clusters of types “a”, “b”, and “c”, as shown in Figure 5.3. Dashed lines with hollow markers are corresponding results for $\Delta E_{\text{cluster,rxn}}^{\text{water}}$ without using eSMS.

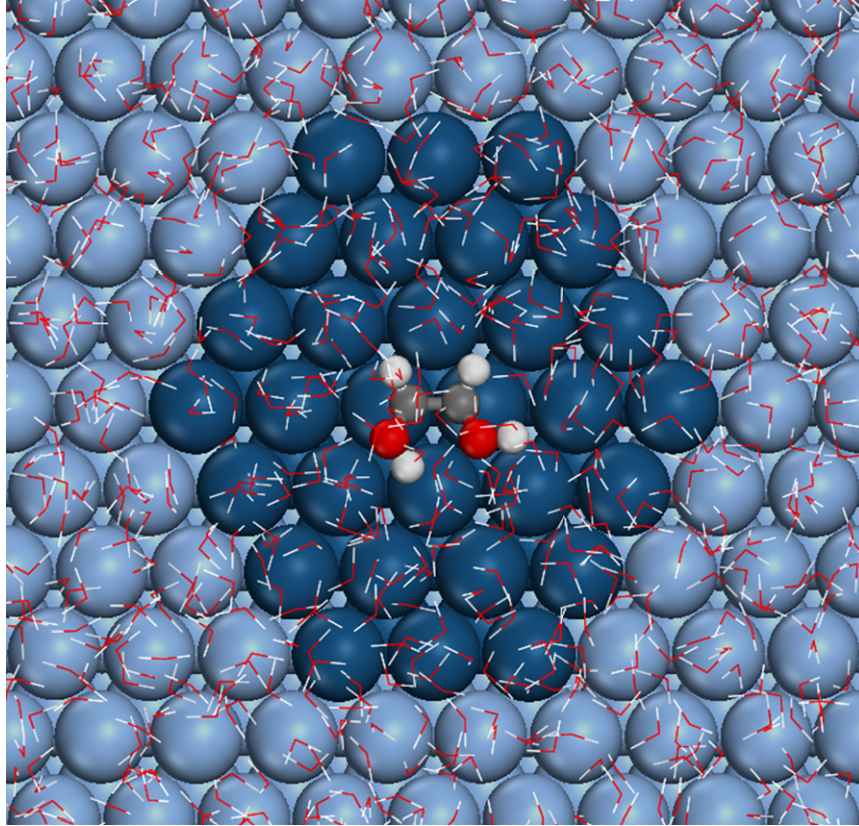


Figure 5.6. Initial state of dehydrogenated ethylene glycol on a two layer, 51-atom cluster with 2250 TIP3P water molecules. Pt-QM (dark blue), Pt-MM (light blue), C-QM (gray), O-QM (red), and H-QM (white) atoms are shown as solid spheres. MM water molecules are shown as lines with O (red) and H (white) vertices.

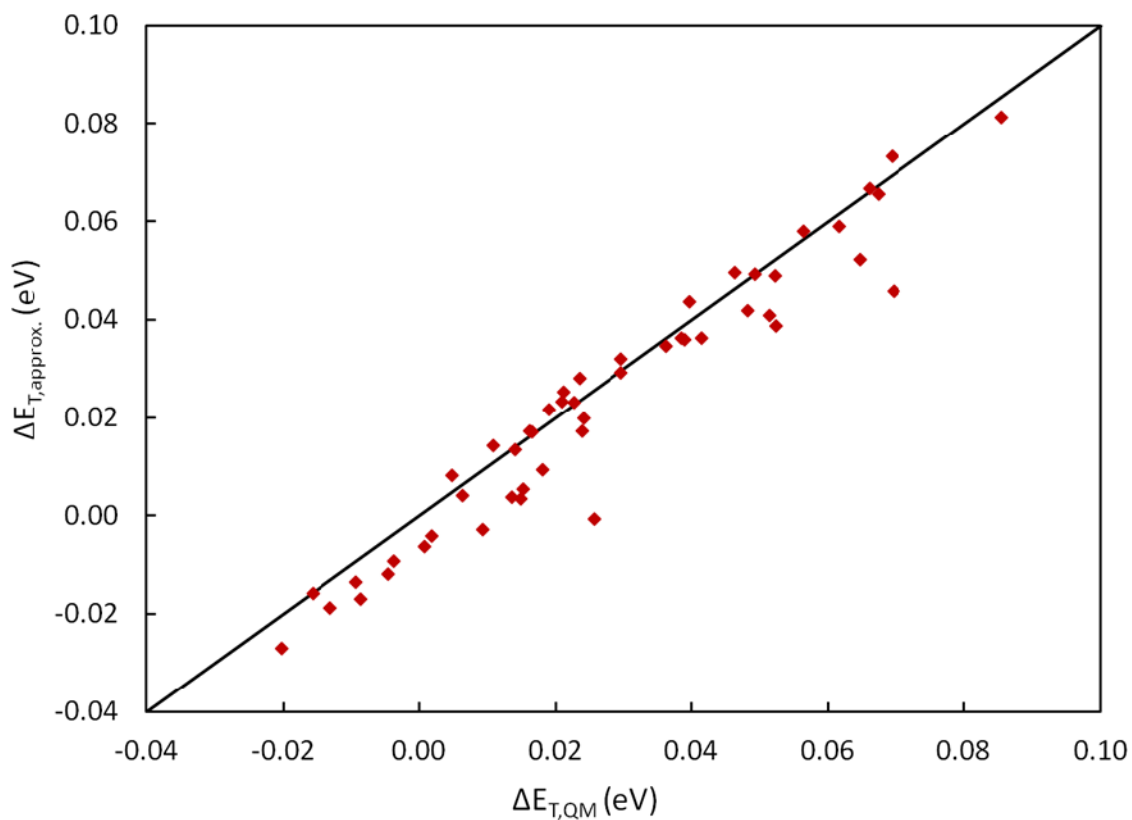


Figure 5.7. Validation of fixed-charge approximation. Difference between total QM/MM energies of 2 QM conformations is evaluated in an ensemble of 50 representative water conformations using exact QM calculations (X-axis) and with the assumption of fixed QM charges (Y-axis).

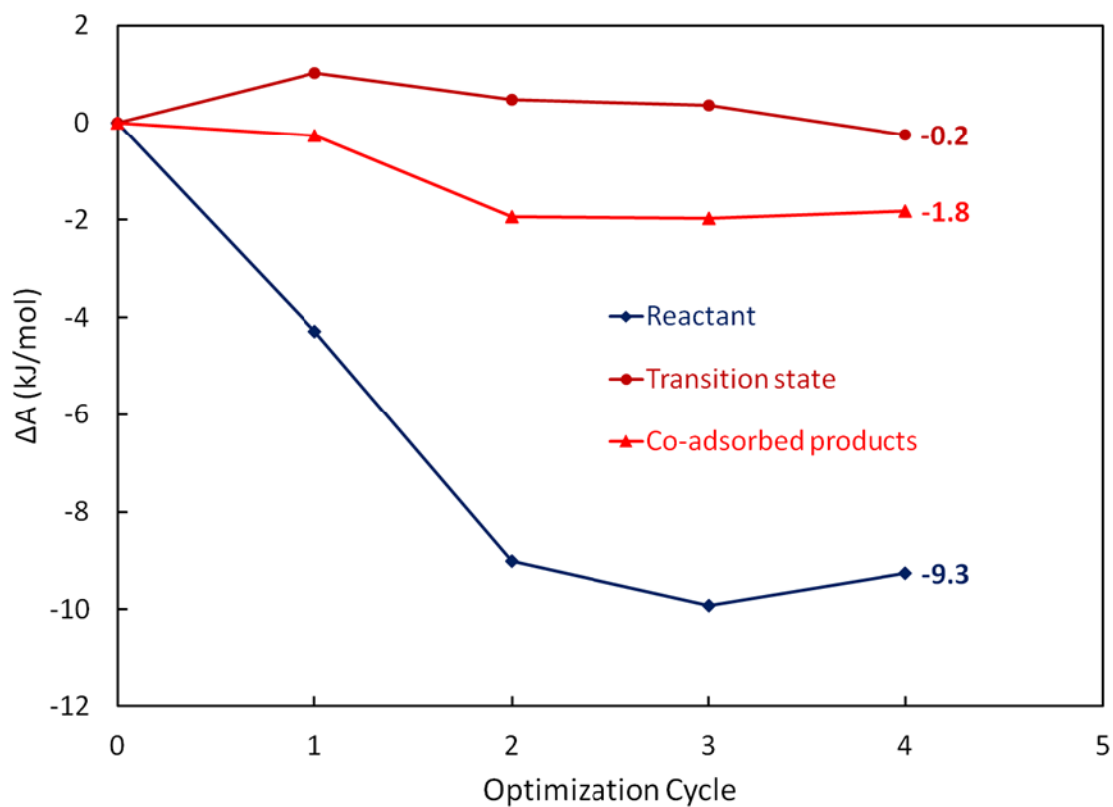


Figure 5.8. Liquid-phase optimization of reactant, product, and transition states using QM/MM-FEP. All free energies are relative to the respective initial states.

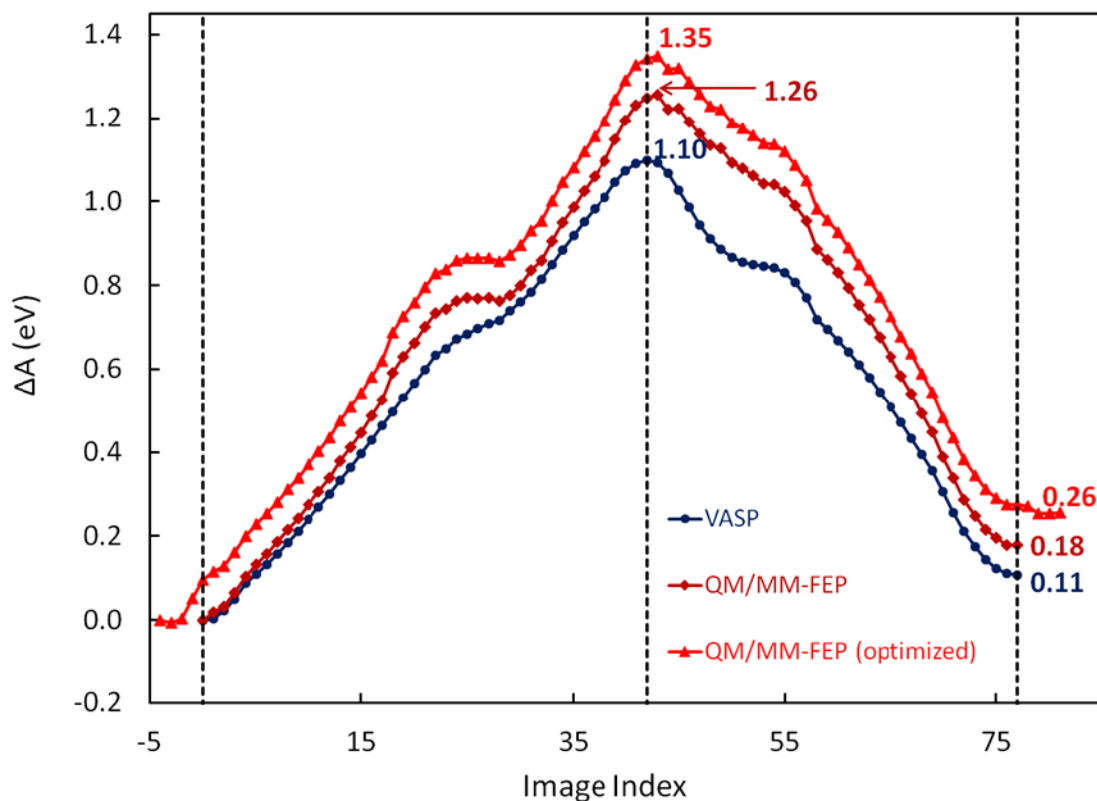


Figure 5.9. Free energy profile (without vibrational contributions to the partition function/free energy) for the reaction $\text{CHOH}-\text{CHOH} \rightarrow 2(\text{CHOH})$. Dashed vertical lines correspond to gas-phase structures of the reactant state (index = 0), transition state (index = 42), and product state (index = 77). For index 0 to 77 the QM/MM-FEP profile is calculated using the same structures as in the gas phase. Results of QM/MM-FEP optimization are included to the left of the gas phase reactant state (index < 0) and to the right of gas phase product state (index > 77). In addition, the gas phase transition state structure is replaced with the transition state structure obtained in liquid water and steps to the left and right are recalculated. The difference between the results depicted here and Table 5.2 originate from the inclusion of vibrational contributions in Table 5.2.

CHAPTER 6

ETHYLENE GLYCOL REFORMING ON Pt(111): FIRST-PRINCIPLES

MICROKINETIC MODELING IN VAPOR AND AQUEOUS PHASES

6.1. Summary

First-principles, periodic density functional theory (DFT) calculations and mean-field microkinetic modeling have been used to investigate the decomposition of ethylene glycol for hydrogen production on Pt(111) in vapor and aqueous phases. All dehydrogenated species derived from ethylene glycol ($C_2H_xO_2$, $x = 0-6$) and methanol (CH_yO , $y = 0-4$), and all elementary C–C, C–H, and O–H bond breaking steps are included in the microkinetic model. Reaction path analysis in vapor phase indicates that both initial C–H and O–H dehydrogenation steps are kinetically relevant at all temperatures (470–530 K). Initial O–H bond cleavage is reversible at low temperatures but accounts for an increasingly dominant fraction of the total reaction flux at higher temperatures. C–C bond scission is observed only after significant dehydrogenation ($x \leq 3$) and is more likely to happen in surface intermediates where one of the cleavage products is CO. The process is highly selective to the production of H_2 compared to methanol. For aqueous-phase model development, free energies of solvation were computed for all surface intermediates and transition states using a continuum solvation

Adapted with permission from Faheem, M.; Lu, J.; Heyden, A. *ACS Catal.* **2014**, Submitted for publication. © 2014 American Chemical Society.

approach. Our aqueous-phase microkinetic model predicts a 0.4 eV lower apparent activation energy and an order of magnitude larger turnover frequencies. Initial C–H bond cleavage becomes more important but the general trends are similar to the vapor phase, suggesting that the reaction chemistry is similar in both vapor and aqueous phases.

6.2. Introduction

The quest for alternative energy resources is driven by increasing global energy demands, rapidly depleting fossil fuel reserves, and environmental considerations. Utilization of lignocellulosic biomass as a renewable source of fuels and value-added chemicals has garnered significant interest in recent years and numerous chemical and catalytic strategies have been developed for biomass processing.¹⁻³ Biomass reforming for production of hydrogen (or syngas) is particularly attractive because the downstream technologies for conversion to liquid fuels and value-added chemicals are well-developed. Biomass-derived oxygenates are largely C₅- and C₆-sugars and their derivatives, and can be used for hydrogen production via aqueous-phase reforming (APR).⁴⁻⁶ The process is typically carried out at elevated temperatures (200–250 °C) using supported metal catalysts with Pt showing highest activity and selectivity toward desired products.⁷⁻⁸ Liquid phase is maintained by keeping the system pressure above the vapor pressure of water at the experimental temperature. Because of their high functionality, these oxygenated feeds are generally highly reactive and the conversion process is a complex reaction mechanism involving a myriad of reactions.² Understanding the mechanism and reaction pathways controlling these transformations is essential for rational catalyst design.

From a computational point of view, the number of possible elementary reactions and surface intermediates increases exponentially with the size of the molecule of interest. Ethylene glycol (EG) is the simplest model molecule of various biomass-derived polyols that contains all relevant C–C, C–O, C–H, and O–H bonds and has a C:O stoichiometry of 1:1 with –OH groups on adjacent C atoms. Ethylene glycol decomposes according to the following reaction:



This pathway implies cleavage of C–C, C–H, and O–H bonds. Water–gas shift (WGS) reaction is also favorable under typical APR conditions and CO produced by reaction (6.1) is largely removed as CO₂.⁹⁻¹⁰



Another possible pathway leads to formation of lower oxygenates and alkanes (for example, ethanol, acetaldehyde, and ethane) through C–O cleavage. Finally, CO and CO₂ can undergo hydrogenation to produce methanol.

Ethylene glycol reforming has been the subject of numerous experimental and computational studies.¹⁰⁻¹⁶ Kandoi et al.¹⁰ compared the kinetics of EG reforming over Pt in vapor and aqueous phases through microkinetic modeling based on a reduced mechanism of 7 lumped reactions. Brønsted–Evans–Polanyi-type correlations¹⁷⁻¹⁸ developed for monofunctional alcohols¹⁹⁻²⁰ were used to estimate activation barriers for bond cleavage steps. Microkinetic model parameters were then fitted to available experimental data.^{11, 21} Saliccioli and coworkers¹³⁻¹⁵ developed a detailed first-principles microkinetic model and successfully predicted intrinsic kinetic trends for Pt catalyzed vapor-phase EG decomposition. Christiansen and Vlachos¹⁶ developed a similar model

for Pt catalyzed vapor-phase steam reforming of EG by including water as a co-reactant. While these computational studies provide useful mechanistic insights, they fail to rigorously account for the influence of an aqueous environment on reaction kinetics and equilibria.

To address this lack of a fundamental understanding of the similarities and differences in the EG reforming chemistry in vapor and aqueous phases, we investigated in this study the mechanism of EG decomposition for hydrogen production on Pt (111) in both phases from first-principles calculations. First, we present a detailed vapor-phase microkinetic model similar to Saliccioli and Vlachos¹⁴ in order to establish a baseline for identification of most abundant surface intermediates, dominant reaction pathways, and general kinetic trends. Next, we reparametrize this model to account for the effect of an aqueous environment using a continuum solvation approach. The microkinetic model does not include any adjustable parameter to fit experimental data and no a priori assumption is made about relative importance of surface intermediates or elementary reactions. Model predicted apparent activation energy, reaction orders, and sensitivity coefficients are compared between vapor and aqueous phases revealing general trends in broad agreement with previous experimental and computational studies. We close with a remark on inclusion of dispersion effects for improving agreement with experimental data.

6.3. Computational Methods

6.3.1. Periodic Planewave DFT Calculations

Periodic DFT calculations were performed using the Vienna *Ab Initio* Simulation Package (VASP 5.2).²² A planewave basis set with a cutoff energy of 400 eV was used to

solve the Kohn–Sham equations. Ionic core potentials were described using the projector augmented wave (PAW) method.²³ Electron exchange and correlation effects were included within the generalized gradient approximation (GGA) using the functional proposed by Perdew, Burke, and Ernzerhof (PBE).²⁴⁻²⁵ Fractional occupancies of bands were allowed within a window of 0.10 eV using a first-order Methfessel–Paxton smearing method.²⁶ All self-consistent field (SCF) calculations were converged to 1.0×10^{-7} eV. The total energy of fcc-Pt bulk was minimized using a $17 \times 17 \times 17$ Monkhorst–Pack k-mesh.²⁷ The calculated equilibrium lattice constant (3.976 Å) is in reasonable agreement with the experimental value (3.92 Å).

Using supercell approach, Pt (111) surface was constructed as a large 4×4 unit cell with four layers of Pt atoms and a vacuum of 15 Å to minimize interaction between periodically repeated images. For all slab calculations, the bottom two Pt layers were fixed at their bulk positions. A $4 \times 4 \times 1$ Monkhorst–Pack k-mesh was employed for sampling the Brillouin zone. Dipole and quadrupole corrections to the energy were included using a modified Makov–Payne method.²⁸ Harris–Foulkes-type corrections for forces were taken into account. Geometry optimizations were stopped when the force on each relaxed atom was smaller than 0.02 eV/Å. A two-step procedure was adopted for all transition state searches. First, an approximate reaction coordinate between the reactant and product states was constructed as a series of intermediate images. After optimizing this chain with the climbing-image nudged elastic band method,²⁹ the image closest to the likely transition state was used as an initial guess for the dimer method.³⁰⁻³¹ All minima and transition state structures were confirmed through dynamical matrix calculations based on numerical second derivatives of the energy.

6.3.2. Implicit Solvation

In this study, the influence of an aqueous environment on reaction kinetics and equilibria is explored using our recently developed iSMS method.³² The principal idea of this approach is to account for the long range metal interactions within the framework of DFT calculations using a periodic slab model in the absence of solvent, and to include the effect of solvent as a localized perturbation of free energy differences that can be described using a cluster model embedded in an implicit solvent. The free energy of an adsorbed intermediate on a “periodic” metal slab in solvent, $G_{\text{surface+adsorbate}}^{\text{liquid}}$, is then obtained using a simple subtraction scheme

$$G_{\text{surface+adsorbate}}^{\text{liquid}} = E_{\text{surface+adsorbate}}^{\text{vacuum}} + G_{\text{cluster+adsorbate}}^{\text{liquid}} - E_{\text{cluster+adsorbate}}^{\text{vacuum}} \quad \dots(6.3)$$

where $E_{\text{surface+adsorbate}}^{\text{vacuum}}$ is the planewave DFT energy for the periodic slab in vacuum, $G_{\text{cluster+adsorbate}}^{\text{liquid}}$ is the free energy in solvent (without explicitly including vibrational contributions) for a metal cluster constructed by removing selected metal atoms from the periodic slab model and removing the periodic boundary conditions, and $E_{\text{cluster+adsorbate}}^{\text{vacuum}}$ is the DFT energy of the same cluster in the absence of solvent. Convergence properties of iSMS with respect to the size of the metal cluster and the basis set have previously been published.³² In this study, we have used a two-layer, 51-atom, Pt (111) cluster to calculate the free energies of solvation for all surface intermediates and transition states. Vibrational contributions to the free energy were included using gas-phase frequencies obtained from periodic slab calculations assuming that the structure of an adsorbed moiety does not change significantly in solvent.

The TURBOMOLE 6.4 program package³³⁻³⁴ was used for nonperiodic cluster calculations. All-electron basis sets of triple- ζ quality were used for adsorbate atoms (C,

O, and H).³⁵ Relativistic small-core effective core potentials (ECPs) were used for Pt atoms and only their valence electrons were represented using triple- ζ quality basis sets.³⁶ Electron exchange and correlation effects were accounted for using the B-P86 functional³⁷⁻³⁸ as required by the parametrization of the implicit solvation model used in this study. The RI-J approximation with auxiliary basis sets was used to approximate Coulomb potentials.³⁹ For all nonperiodic structures, multiple spin states were tested using an SCF convergence criterion of 1.0×10^{-7} hartree and spherical grid m4.⁴⁰ Only for the lowest-energy spin state, COSMO⁴¹⁻⁴² calculations were performed using radii-based cavities and a dielectric constant of infinity. For these calculations, SCF convergence criterion and spherical grid were changed to 1.0×10^{-8} hartree and m5, respectively. Free energies of solvation were computed using COSMO-RS.⁴³ Thermodynamic properties of water (solvent) were obtained from the COSMOtherm database,⁴⁴ based on parametrization of the results of quantum chemical COSMO calculations at the BP-TZVP level of theory.

6.4. Model Development

6.4.1. Microkinetic Modeling

A mean-field microkinetic model was developed for reaction pathway analysis under realistic process conditions. All dehydrogenated species derived from ethylene glycol ($C_2H_xO_2$, $x = 0-6$) and methanol (CH_yO , $y = 0-4$), and all elementary C-C, C-H, and O-H bond breaking steps were included. We note here that C-O bond scission in EG leads to formation of ethanol and ultimately ethane. However, experimental studies of EG reforming over Pt have shown only trace amounts of these products.^{10, 21} We confirmed this overall conclusion by computing activation barriers for C-O cleavage in selected

surface intermediates. These barriers were found to be significantly higher than the barriers for C–C cleavage in the same intermediates. For these reasons, C–O bond scissions are not included in the microkinetic model. In addition, considering the low levels of CO reported in the product stream,⁹⁻¹⁰ we assume that the WGS reaction approaches equilibrium at all temperatures and the CO concentration in the effluent stream is 500 ppm. Elementary reactions pertaining to the WGS mechanism are not explicitly considered.

All reactions were assumed to be reversible. The net rate of a reaction *i* is given by

$$r_i = k_{f,i} \prod_{j=1, n_j < 0}^{j=N} C_j^{-n_j} - k_{r,i} \prod_{j=1, n_j > 0}^{j=N} C_j^{n_j} \quad \dots(6.4)$$

where $k_{f,i}$ and $k_{r,i}$ are the forward and reverse reaction rate constants, respectively. Index *j* loops over all *N* species involved in the reaction, and the corresponding concentration C_j equals either a fractional surface coverage (θ_j) or a gas-phase partial pressure (P_j). The stoichiometric coefficient n_j is negative for reactants and positive for products. For all surface reactions, forward rate constants were calculated using harmonic transition state theory.⁴⁵

$$k_{f,i} = \frac{\gamma k_B T}{h} \exp\left(\frac{-\Delta G_i^\ddagger}{k_B T}\right) \quad \dots(6.5)$$

Here, ΔG_i^\ddagger is the free energy of activation, *T* is the absolute temperature, and k_B and *h* are respectively the Boltzmann and Planck constants. The transmission coefficient γ was assumed to be 1.0 for all cases. Zero-point energies and (harmonic) vibrational partition

functions were calculated using vibrational frequencies (ν_i) derived from planewave DFT calculations.

$$E_{zpv} = \sum_i \frac{h\nu_i}{2}, \quad q_{vib} = \prod_i \left[1 - \exp\left(\frac{-h\nu_i}{k_B T}\right) \right]^{-1} \quad \dots(6.6)$$

We note here that the top two Pt layers were relaxed during geometry optimization but fixed for frequency calculations. This procedure reduces the accuracy of low-frequency modes that are coupled with the metal atoms. Considering that the harmonic approximation is least accurate for small wavenumbers, we shifted all (real) frequencies for adsorbed intermediates and transition states below 100 cm^{-1} to 100 cm^{-1} . These low-frequency modes thus cancel out for surface reactions and have no effect on reaction free energies and activation barriers. This adjustment is not required for gas-phase molecules because the translational and rotational degrees of freedom are projected out and the respective partition functions are rigorously included using statistical mechanics.⁴⁶

Adsorption was assumed to be a nonactivated process and collision theory was used to calculate the forward rate constants.

$$k_{f,i} = \frac{S\sigma}{N\sqrt{2\pi M_i k_B T}} \quad \dots(6.7)$$

Here, N/S is the number of catalytic sites per unit surface area and M_i is the molecular weight of the adsorbate. The sticking probability σ was assumed to be 1.0 for all cases. Equation (6.7) thus gives an upper limit for the adsorption rate constant. As we will show later, the rates of adsorption–desorption processes are many orders of magnitude faster than the rates of surface reactions and these processes may be assumed to be in

equilibrium. To ensure thermodynamic consistency, reverse rate constants were always calculated from the thermodynamic equilibrium constants (K_{eq}).

$$K_{eq,i} = \exp\left(\frac{-\Delta G_i}{k_B T}\right); \quad k_{r,i} = \frac{k_{f,i}}{K_{eq,i}} \quad \dots(6.8)$$

where ΔG_i is the Gibbs free energy of reaction.

With all rate parameters known, a microkinetic model was developed as a system of ordinary differential equations. At steady state, the fractional coverage of a surface intermediate is given by

$$\frac{d\theta_j}{dt} = \sum_i v_{j,i} r_i = 0 \quad \dots(6.9)$$

where index i loops over all reactions. In addition, the total number of sites is conserved.

$$\sum_j n_j \theta_j = 1 \quad \dots(6.10)$$

A complete list of number of sites assigned to each species (n_j) is provided in Appendix C. All microkinetic simulations were initialized with a clean Pt surface and solved as a system of differential algebraic equations using the BzzMath library⁴⁷ to obtain steady state fractional surface coverages and turnover frequencies (TOFs). Although significantly slower than a nonlinear solver,⁴⁸ this approach offers higher numerical stability and is essentially independent of the initial guess.

6.4.2. Adsorbate–Adsorbate Lateral Interactions

It is well known that at high CO coverage on Pt (111), adsorbed CO molecules destabilize the binding strength of each other resulting in a decrease of the adsorption energy.⁴⁹⁻⁵⁰ Preliminary results of a vapor-phase microkinetic model showed that if these

lateral interactions are not considered, the surface is completely poisoned by CO. That is, adsorbate–adsorbate interactions must be included in the microkinetic model to better describe the state and condition of the catalytic surface in a realistic reaction environment. In order to obtain coverage dependent adsorption energies of CO and H, DFT calculations were performed at various surface coverages on a $3 \times 3 \times 4$ Pt (111) slab. Possible permutations of coadsorbed species were taken into account and all such configurations were Boltzmann-averaged at 500 K. More information about this data set is provided in Appendix C. For CO–CO, H–H, and CO–H lateral interactions, we used the functional form proposed by Grabow et al.⁵⁰ For all other surface intermediates and transition states, destabilization due to CO and H was assumed to be similar¹⁴ and the corresponding parameters were derived from DFT calculations with coadsorbed EG. Finally, destabilization of surface intermediates due to interactions among them was described by the same parameters as used for CO–CO interaction. We note here that the value of this parameter is not significant since the coverage of these species is very small compared to CO and H. A summary of all adsorbate–adsorbate interaction parameters is shown in Table 6.1.

6.5. Results and Discussion

6.5.1. Dehydrogenation of $C_2H_xO_2$ and CH_yO Species

Energetics of all dehydrogenated species derived from ethylene glycol ($C_2H_xO_2$, $x = 0–6$) and methanol (CH_yO , $y = 0–4$) have been systematically investigated in this study. Binding modes for the most stable adsorption geometries of all intermediates are provided in Appendix C. Reaction energies and activation barriers for all surface reactions are listed in Table 6.2. Adsorption energies are listed in Table 6.3.

Ethylene glycol binds to the Pt(111) surface through one of the –OH groups which points to the other –OH group forming an intramolecular hydrogen bond. This adsorption geometry is different from the one reported by Saliccioli et al.⁵¹ who found that both oxygen atoms bind to adjacent top sites of Pt. The calculated adsorption energies are however in good agreement (–0.46 eV calculated in this work versus –0.49 eV previously reported). Both carbon atoms are far from the surface and must overcome steric hindrance of the –OH groups and H atoms to allow for C–Pt interaction. As a result, the barrier for C–C cleavage in EG is very high (2.07 eV) and initial dehydrogenation of EG is necessary.

Two possibilities exist for initial dehydrogenation of EG on Pt(111). DFT calculations predict that initial C–H bond scission is thermodynamically favored ($\Delta E_{\text{rxn}} = -0.48 \text{ eV}$) over initial O–H bond scission ($\Delta E_{\text{rxn}} = +0.40 \text{ eV}$). However, in the most stable adsorption configuration, the H atom from the –OH group is already in close proximity to the surface, whereas an α -H atom can come close to the surface only after significant rotation of the –CH₂OH group. As a result, the transition state for initial O–H scission is predicted to be 0.12 eV lower than that for initial C–H scission. This difference in activation barriers is small and we can expect both pathways to be competitive.

Thermodynamic analysis of all subsequent dehydrogenation steps reveals a similar trend. C–H bond scission is always exothermic and thermodynamically favored over O–H bond scission in the same surface moiety. After initial dehydrogenation, EG-derived species bind strongly to the surface in a manner that unsaturated C atoms satisfy their tetrahedral bonding geometry. Unsaturated O atoms, if present, bind to the surface

to complete a total of two bonds. The only exception is the aldehyde ($-\text{CHO}$) group which can leave the surface and bind through an O atom (for example, in COH-CHO). Among equally dehydrogenated intermediates, species that bind through a C atom ($-\text{CHOH}$ group) are more stable than the species that bind through an O atom ($-\text{CH}_2\text{O}$ group). Formation of an intramolecular hydrogen bond (for example, in CHOH-CHOH) is energetically favorable. Deeper dehydrogenation results in stronger adsorption and lower barrier for C–C cleavage reactions. Previous computational studies have reported similar observations.^{13, 51}

There are two possible $\text{C}_2\text{H}_5\text{O}_2$ intermediates. After initial C–H scission, the barrier for α -H abstraction in $\text{CHOH-CH}_2\text{OH}$ to $\text{COH-CH}_2\text{OH}$ (0.37 eV) is similar to that for β -H abstraction to CHOH-CHOH (0.35 eV), although the latter is slightly thermodynamically favored. After initial O–H scission, abstraction of α -H in $\text{CH}_2\text{O-CH}_2\text{OH}$ to $\text{CHO-CH}_2\text{OH}$ (glycolaldehyde) requires a very small barrier of 0.11 eV compared to 0.34 eV for abstraction of β -H to $\text{CH}_2\text{O-CHOH}$. Cleavage of O–H bonds in either $\text{C}_2\text{H}_5\text{O}_2$ species is highly unfavorable compared to C–H bond scission.

There are five possible $\text{C}_2\text{H}_4\text{O}_2$ intermediates. The lowest activation barrier (0.05 eV) at this level of dehydrogenation is observed for decomposition of $\text{CH}_2\text{O-CHOH}$ to CHO-CHOH (from the initial O–H bond scission pathway). Decomposition of glycolaldehyde on the same pathway requires a considerably higher activation energy (0.37 eV). For the initial C–H bond scission pathway, the lowest barrier (0.20 eV) is observed for O–H bond cleavage in $\text{COH-CH}_2\text{OH}$ to produce $\text{CO-CH}_2\text{OH}$. This is the first species in this reaction mechanism where the barrier for C–C cleavage is low enough to be competitive with the dehydrogenation reactions. In addition, the

pathways through initial C–H and O–H bond scissions start to merge at this level of dehydrogenation.

Among the five possible $C_2H_3O_2$ intermediates, the most plausible dehydrogenation steps are C–H bond scission in CHO-CHOH (barrier = 0.27 eV) and O–H bond scission in COH-CHOH (barrier = 0.41 eV), both leading to the same product, CO-CHOH. Decomposition of CO-CH₂OH to CO-CH₂O has a comparable barrier (0.45 eV). This is followed by a small barrier (0.16 eV) for decomposition to CO-CHO. Removal of the last H atom from CO-CHO has almost the same barrier as C–C bond cleavage in this intermediate, with the latter being the thermodynamically preferred pathway by about 0.6 eV. C–C bond cleavage in completely dehydrogenated CO-CO occurs without an activation barrier.

Methanol also binds to the Pt(111) surface through the –OH group. The calculated adsorption energy of –0.27 eV is comparable to the previously reported value of –0.33 eV.⁵² While the –CH₃ group is initially far from the surface, unlike ethylene glycol, there is no steric hindrance and α -H atoms can easily come close to the metal. As a result, the barriers for C–H cleavage are smaller than the barriers for O–H cleavage in all methanol-derived surface intermediates. As before, species that bind through carbon are energetically more stable than the species that bind through oxygen.

6.5.2. Vapor-Phase Microkinetic Model

A detailed vapor-phase microkinetic model was developed to establish a baseline for identification of the most abundant surface intermediates, dominant reaction pathways, and general kinetic trends. The feed stream consisted of 10 mole percent EG at a total pressure of 1 bar. Conversion of EG was assumed to be 1% to simulate differential

reactor operation. The WGS reaction was assumed in equilibrium and the CO concentration in the effluent stream was fixed at 500 ppm. In the overall reforming reaction, 1 mole of EG is converted to 5 moles of H₂. All turnover frequencies (TOFs) reported in this work are based on a rate of EG consumption per second and should be multiplied by 300 for comparison with the experimental data of Kandoi et al.¹⁰ (which are reported based on a H₂ production rate per minute).

Reference simulations for the determination of the most abundant surface intermediates were performed over a temperature range of 470 K to 530 K (Figure 6.1). CO* and H* are the most abundant adsorbates over this entire temperature range. The coverage of CO* is 41% at 470 K and only slightly decreases to 38% at 530 K. The coverage of H* is more sensitive to temperature and decreases from 45% at 470 K to 35% at 530 K. A small coverage of COH* (~ 0.6%) is observed at lower temperatures but quickly disappears as the temperature is increased. Coverage of all other adsorbates is negligible. The predicted turnover rates are generally an order of magnitude smaller than the experimental data.¹⁰ Given the uncertainty associated with DFT-predicted binding energies, the possibility of more active catalytic sites (for example, edges and corners), and a rudimentary description of adsorbate–adsorbate interactions, this level of disagreement between model-predicted and experimental TOFs is acceptable.

Table 6.4 shows a comparison of the model-predicted apparent activation energy and reaction orders with previously reported data. Both CO and H have a poisoning effect on the catalyst as evidenced by negative reaction orders of -0.58 and -0.84, respectively. For these simulations, the CO or H₂ gases were co-fed at concentrations indicated in Figure 6.2A and B, respectively. An increase in EG pressure has a positive effect on

the overall TOF (Figure 6.2C). The predicted reaction order (1.0) however differs from the observed fractional order (0.4). The DFT-predicted equilibrium constant for EG adsorption is very small compared to the equilibrium constants for CO adsorption and H₂ dissociation. As a result, the coverage of C₂H_xO₂ intermediates is much smaller than the available free sites at all temperatures and increases proportionally with increase in EG partial pressure without significantly decreasing the availability of free sites; thus, leading to an apparent first order effect on the overall TOF. For the same reason, the predicted apparent activation energy is higher than the reported values. As we will show later, initial steps in this mechanism are rate limiting. Therefore, the apparent activation energy is strongly correlated to the energy of these transition states relative to gas-phase ethylene glycol. A large positive free energy of EG adsorption (Table 6.3) shifts these transition states upwards on a free energy scale (Figure 6.3) resulting in a higher overall activation energy. In section 6.5.4, we discuss a possible solution to this problem by inclusion of dispersion effects on adsorption energies.

The inhibiting effect of total pressure is correctly predicted (Figure 6.2D). These simulations were performed by varying the total pressure while maintaining the fixed feed composition and conversion of 1%. While an increase in EG partial pressure increases the reaction rate, site blocking due to increased partial pressures of CO and H₂ becomes more significant, resulting in an overall negative reaction order (-0.13) with respect to total pressure. Figure 6.2D shows that this effect is even more pronounced at higher total pressures (reaction order changes to -0.7).

An analysis of steady state reaction fluxes can provide useful insights into the reaction mechanism and dominant pathways under realistic reaction environments. Figure

6.3 shows the fraction of the overall reaction flux passing through various pathways in vapor-phase EG reforming at 500 K. The dominant mechanism for EG decomposition is through initial O–H bond cleavage which is in agreement with TPD experiments.¹³ While initial C–H bond scission is irreversible, the relatively small reverse barrier for initial O–H bond scission causes this reaction to be nearly in equilibrium and to have a considerable rate in the reverse direction. Altogether both initial C–H and O–H bond scission pathways contribute significantly to the overall rate of EG decomposition. Partial equilibrium (PE) analysis⁵³ indicates that the reversibility of the initial O–H bond breaking reaction decreases at higher temperatures. The PE ratio (ϕ_i) is defined as the ratio of the forward reaction rate ($r_{f,i}$) to the sum of forward and reverse ($r_{r,i}$) reaction rates.

$$\phi_i = \frac{|r_{f,i}|}{|r_{f,i}| + |r_{r,i}|} \quad \dots(6.11)$$

A PE ratio is 1.0 for an irreversible reaction in the forward direction and 0.5 for a reaction where the forward and reverse reaction rates are equal. Initial C–H bond scission has a PE ratio of 1.0 over the temperature range explored in this study. In contrast, at lower temperatures the PE ratio for the initial O–H bond cleavage reaction is only slightly larger than 0.5 (computed PE ratio is 0.56 at 470 K, 0.63 at 500 K, and 0.73 at 530 K). As this reaction becomes irreversible at higher temperatures, the contribution of the initial O–H bond scission pathway to the overall rate of the EG decomposition increases (Figure 6.4A).

In the reaction pathway through initial O–H bond scission, the reaction flux largely passes through a deep dehydrogenation of the α -carbon to CHO-CH₂OH

(glycolaldehyde) and CO-CH₂OH. In the reaction pathway through initial C–H bond scission, β-H abstraction to CHOH-CHOH occurs first, followed by C–H cleavage to COH-CHOH and subsequent O–H cleavage to CO-CHOH. C–C cleavage is observed only after one side of the EG molecule is completely dehydrogenated (that is, only in C₂H_xO₂ intermediates with x ≤ 3). Many C–C cleavage pathways are active at 500 K as shown by their relative contributions in Figure 6.3 (CO-CH₂OH: 28%, CO-CHOH: 24%, CO-CO: 22%, CO-CHO: 15%, and CO-CH₂O: 9%). The reforming mechanism shows a very high selectivity toward complete decomposition of ethylene glycol to carbon monoxide and hydrogen. In comparison, hydrogenation of CO to produce methanol is 2–5 orders of magnitude slower. Only at higher H₂ partial pressures (> 0.5 bar) did we observe more methanol than hydrogen production.

We used Campbell’s degree of rate control⁵⁴ and degree of thermodynamic rate control⁵⁵⁻⁵⁶ analyses to identify rate-controlling elementary steps and surface intermediates.

$$X_{RC,i} = \left[\frac{\partial \ln(r)}{\partial \left(\frac{-G_i^{0,TS}}{k_B T} \right)} \right]_{G_{j \neq i}^{0,TS}, G_m^0} ; \quad X_{TRC,n} = \left[\frac{\partial \ln(r)}{\partial \left(\frac{-G_n^0}{k_B T} \right)} \right]_{G_{m \neq n}^0, G_i^{0,TS}} \quad \dots(6.12)$$

Here, $X_{RC,i}$ is the degree of rate control for elementary reaction i , $X_{TRC,n}$ is the degree of thermodynamic rate control for adsorbate n , r is the overall rate of reaction, $G_i^{0,TS}$ is the free energy of transitions state i , and G_n^0 is the free energy of adsorbate n . Results of these sensitivity analyses are summarized in Table 6.5. Along the dominant pathway for the EG decomposition, initial O–H bond scission and subsequent α-H abstraction to glycolaldehyde are the most kinetically relevant steps and collectively account for 75–

85% of the overall degree of rate control. Along the pathway through initial C–H scission, only the first dehydrogenation step shows an appreciable sensitivity coefficient. C–C cleaving reactions have no effect on the overall TOF. These observations are consistent with previous experimental and computational studies.¹³⁻¹⁴ The degree of thermodynamic rate control is substantial only for H*, CO*, and COH*. All these species have a poisoning effect on the catalyst such that destabilizing their adsorption increases the overall reaction rate.

6.5.3. Aqueous-Phase Microkinetic Model

To account for an aqueous environment, free energies of solvation obtained from COSMO-RS calculations were used to reparametrize the microkinetic model. For an adsorption–desorption process

$$\Delta G_L = \Delta G_G + G_{\text{ads}}(\text{solv}) - G_{\text{Pt}}(\text{solv}) \quad \dots(6.13)$$

where the subscripts G and L refer to the vapor/gas and liquid/aqueous phases, respectively. $G_{\text{ads}}(\text{solv})$ and $G_{\text{Pt}}(\text{solv})$ are the free energies of solvation for a Pt cluster with and without an adsorbate, respectively. Similarly, for a surface reaction

$$\Delta G_L = \Delta G_G + G_{\text{FS}}(\text{solv}) - G_{\text{IS}}(\text{solv}) \quad \dots(6.14)$$

$$\Delta G_L^\ddagger = \Delta G_G^\ddagger + G_{\text{TS}}(\text{solv}) - G_{\text{IS}}(\text{solv}) \quad \dots(6.15)$$

where the subscripts IS, FS, and TS stand for initial, final, and transition states, respectively.

Aqueous-phase reforming is simulated for the same set of process conditions as previously described for the vapor phase. The only difference is that the total pressure used to calculate free energies of solvation for adsorbed intermediates and transition

states now additionally includes the saturation pressure of water at the simulation temperature, e.g., $P_{\text{H}_2\text{O}} = 26.4$ bar at 500 K.

Figure 6.5 illustrates the effect of temperature on the coverage of the most abundant surface intermediates and overall TOFs. As in the vapor phase, CO^* and H^* are the dominant surface species. The CO^* coverage however has increased (46–51%) and the H^* coverage has significantly decreased (23–30%). Adsorption energies reported in Table 6.3 show that adsorbed ethylene glycol, methanol, and CO are stabilized in water, whereas adsorbed hydrogen is destabilized. The larger equilibrium constant for EG adsorption results in an order of magnitude larger overall TOFs (Figure 6.4B). This positive effect of an aqueous environment on the reaction rate is in agreement with experimental data. Shabaker et al.²¹ reported a H_2 production TOF of 7.0 min^{-1} at 498 K for aqueous-phase reforming of ethylene glycol over 3.43% Pt/ Al_2O_3 . From the experimental data of Kandoi et al.,¹⁰ the corresponding TOF at 498 K for vapor-phase reforming of ethylene glycol over 3.0% Pt/ Al_2O_3 is estimated to be $2\text{--}3 \text{ min}^{-1}$.

The dependence of the overall TOF on the total system pressure and partial pressures of EG, CO, and H_2 in aqueous-phase reforming is shown in Figure 6.6 and summarized in Table 6.4. As before, the model-predicted ethylene glycol order (1.0) differs from the experimentally observed fractional order (0.3–0.5). The CO order is practically unchanged whereas the hydrogen order is now reduced to -0.47 (from -0.84 in vapor-phase reforming). As before the total system pressure has a strong inhibiting effect on the rate of EG decomposition.

Figure 6.4A compares the contribution of initial C–H and O–H scission pathways to the total rate of ethylene glycol decomposition in both phases. In vapor-phase

reforming, the relative contribution of the two pathways changes with temperature because the initial O–H cleavage reaction moves from partial equilibrium to irreversibility. Similar PE analysis in aqueous phase reveals that, because of a significantly lower H* coverage, this reaction is already far from equilibrium (computed PE ratio is 0.90 at 470 K, 0.95 at 500 K, and 0.97 at 530 K). As a result, the relative contribution of the two pathways is nearly constant at all temperatures. Decomposition through initial C–H bond scission becomes more important in aqueous phase which can be explained by a significant stabilization of this transition state in water. Table 6.2 shows that the free energy barrier for initial C–H bond cleavage is reduced from 0.83 eV in vapor phase to 0.75 eV in water. On the other hand, the free energy barrier for initial O–H bond cleavage is almost unaffected (0.71 eV and 0.70 eV in vapor and aqueous phases, respectively). As a result, the effect of water on the rate of initial C–H bond scission is considerably larger than that on initial O–H bond scission at all temperatures (Figure 6.4B).

Figure 6.7 illustrates the fraction of the overall reaction flux passing through various pathways in aqueous-phase EG reforming at 500 K. Table 6.5 summarizes the results of a similar sensitivity analysis as described earlier. All surface intermediates and elementary reactions identified to be significant in this case are the same as previously determined from the analysis of the vapor-phase microkinetic model. Noting that the relative fluxes through various elementary steps are also generally comparable, it can be concluded that the reaction chemistry of EG reforming is similar in both vapor and aqueous phases. This confirms the observation of Kandoi et al.¹⁰ that similar values of

kinetic parameters can be used to describe the vapor- and aqueous-phase reforming data suggesting a similar reaction mechanism in both phases.

6.5.4. Dispersion Effects

The microkinetic model presented in this work is generally able to reproduce experimentally observed kinetic trends. However, the disagreement between a model-predicted first order and previously reported fractional order with respect to ethylene glycol partial pressure requires further investigation. As Shabaker et al.²¹ pointed out, a fractional order for ethylene glycol suggests that the coverage of EG-derived surface intermediates is significant under experimental conditions and there is competition for available free sites. Microkinetic simulations however predict that the coverage of all such intermediates is negligible. The origin of this discrepancy can be traced to a large positive free energy and a very small equilibrium constant for EG adsorption (Table 6.3). When adsorbed on a Pt (111) surface, saturated oxygenates like ethylene glycol and methanol do not form true chemical bonds to the metal. For such weakly chemisorbed systems dispersion forces attain an increased relative importance.⁵⁷ These effects are not properly described by standard GGA functionals like PBE and the predicted adsorption energies are greatly underestimated.

To address this problem, we calculated the dispersion-corrected adsorption energy for ethylene glycol using the PBE-D3 method.⁵⁸ A separate Pt (111) slab was constructed for these calculations to account for a smaller equilibrium lattice constant (3.927 Å). Table 6.3 shows that the adsorption energy of ethylene glycol increases by 0.68 eV after dispersion effects are included. To maintain overall thermodynamic

consistency, PBE-D3 calculations were also performed for all other gas-phase species (CO, H₂, and methanol).

Table 6.6 summarizes the predictions of vapor- and aqueous-phase microkinetic models when dispersion-corrected adsorption energies are used. The ethylene glycol order is still positive but now smaller than 1.0 in both phases. Negative reaction orders with respect to total pressure and partial pressures of carbon monoxide and hydrogen are correctly captured. Also, the overestimation of the apparent activation energy has largely been corrected. CO* and H* are still the most dominant surface species and their coverages have increased from previous calculations reducing the availability of free sites. The coverage of ethylene glycol is on the order of 1% (an increase of 6–7 orders of magnitude). While the qualitative agreement with some experimental data is improved (as a result of a significant increase in ethylene glycol coverage but only a modest decrease in the availability of free sites), overall turnover frequencies are now over-predicted by 3–4 orders of magnitude. Thus, PBE-D3 likely overestimates adsorption energies and “true” adsorption energies are in between those computed by PBE and PBE-D3. Next, we observe that the effect of an aqueous environment on the mechanism of EG reforming is independent of DFT functional and relative fluxes through various pathways remain largely unaffected and previous conclusions about the solvent effect on reforming rates remain applicable. Finally, the O–H and C–H bond scission steps remain the most rate controlling steps; although, CO and H₂ product desorption also become partially rate controlling particularly in an aqueous environment.

6.6. Conclusions

Mechanisms of Pt catalyzed vapor- and aqueous-phase ethylene glycol reforming for hydrogen production were systematically investigated using first-principles calculations. Detailed microkinetic models were developed to provide insights into the surface chemistry under realistic process conditions. The vapor-phase microkinetic model was parametrized using harmonic transition state theory and DFT-derived reaction energies and activation barriers. This model confirms that the dominant pathway for ethylene glycol decomposition is through initial O–H dehydrogenation, although the pathway through initial C–H cleavage remains kinetically relevant at all temperatures. A sensitivity analysis shows that only early dehydrogenation steps are rate determining. C–C bond cleavage occurs only after a significant dehydrogenation and almost exclusively in those intermediates where one of the cleavage products is CO. The reforming mechanism is highly selective toward complete decomposition to H₂ and CO and alternative pathways are not active except at higher hydrogen partial pressures (> 0.5 bar).

The aqueous-phase microkinetic model was parameterized using our continuum solvation approach (iSMS). This model predicts that an aqueous environment lowers the apparent activation energy and increases the rate of decomposition. While the pathway through initial O–H bond scission remains dominant in aqueous-phase reforming, disproportionate stabilization of the transition state for initial C–H bond breaking results in larger contribution of this pathway to the total rate of decomposition. The dominant surface intermediates and rate controlling steps remain unchanged from vapor-phase

reforming and the relative reaction fluxes through various pathways are comparable, indicating that the reforming chemistry on platinum is similar in both phases.

6.7. References

1. Huber, G. W.; Dumesic, J. A. *Catal. Today* **2006**, *111*, 119–132.
2. Huber, G. W.; Iborra, S.; Corma, A. *Chem. Rev.* **2006**, *106*, 4044–4098.
3. Tanksale, A.; Beltramini, J. N.; Lu, G. M. *Renewable Sustainable Energy Rev.* **2010**, *14*, 166–182.
4. Cortright, R. D.; Davda, R. R.; Dumesic, J. A. *Nature* **2002**, *418*, 964–967.
5. Davda, R. R.; Dumesic, J. A. *Chem. Commun.* **2004**, 36–37.
6. Kirilin, A. V.; Tokarev, A. V.; Kustov, L. M.; Salmi, T.; Mikkola, J. P.; Murzin, D. Y. *Appl. Catal., A* **2012**, *435*, 172–180.
7. Davda, R. R.; Shabaker, J. W.; Huber, G. W.; Cortright, R. D.; Dumesic, J. A. *Appl. Catal., B* **2003**, *43*, 13–26.
8. Davda, R. R.; Shabaker, J. W.; Huber, G. W.; Cortright, R. D.; Dumesic, J. A. *Appl. Catal., B* **2005**, *56*, 171–186.
9. Davda, R. R.; Dumesic, J. A. *Angew. Chem., Int. Ed.* **2003**, *42*, 4068–4071.
10. Kandoi, S.; Greeley, J.; Simonetti, D.; Shabaker, J.; Dumesic, J. A.; Mavrikakis, M. *J. Phys. Chem. C* **2011**, *115*, 961–971.
11. Shabaker, J. W.; Huber, G. W.; Davda, R. R.; Cortright, R. D.; Dumesic, J. A. *Catal. Lett.* **2003**, *88*, 1–8.
12. Huber, G. W.; Shabaker, J. W.; Evans, S. T.; Dumesic, J. A. *Appl. Catal., B* **2006**, *62*, 226–235.
13. Saliccioli, M.; Yu, W. T.; Barteau, M. A.; Chen, J. G. G.; Vlachos, D. G. *J. Am. Chem. Soc.* **2011**, *133*, 7996–8004.
14. Saliccioli, M.; Vlachos, D. G. *ACS Catal.* **2011**, *1*, 1246–1256.
15. Saliccioli, M.; Vlachos, D. G. *ACS Catal.* **2012**, *2*, 306–306 Erratum.
16. Christiansen, M. A.; Vlachos, D. G. *Appl. Catal., A* **2012**, *431*, 18–24.
17. Norskov, J. K.; Bligaard, T.; Logadottir, A.; Bahn, S.; Hansen, L. B.; Bollinger, M.; Bengaard, H.; Hammer, B.; Sljivancanin, Z.; Mavrikakis, M.; Xu, Y.; Dahl, S.; Jacobsen, C. J. H. *J. Catal.* **2002**, *209*, 275–278.
18. Jones, G.; Bligaard, T.; Abild-Pedersen, F.; Norskov, J. K. *J. Phys.: Condens. Matter* **2008**, *20*, 064239.
19. Alcalá, R.; Mavrikakis, M.; Dumesic, J. A. *J. Catal.* **2003**, *218*, 178–190.
20. Greeley, J.; Mavrikakis, M. *J. Am. Chem. Soc.* **2004**, *126*, 3910–3919.
21. Shabaker, J. W.; Davda, R. R.; Huber, G. W.; Cortright, R. D.; Dumesic, J. A. *J. Catal.* **2003**, *215*, 344–352.
22. Hafner, J. *Comput. Phys. Commun.* **2007**, *177*, 6–13.
23. Kresse, G.; Joubert, D. *Phys. Rev. B* **1999**, *59*, 1758–1775.
24. Perdew, J. P.; Burke, K.; Ernzerhof, M. *Phys. Rev. Lett.* **1996**, *77*, 3865–3868.
25. Perdew, J. P.; Burke, K.; Ernzerhof, M. *Phys. Rev. Lett.* **1997**, *78*, 1396–1396 Erratum.
26. Methfessel, M.; Paxton, A. T. *Phys. Rev. B* **1989**, *40*, 3616–3621.

27. Monkhorst, H. J.; Pack, J. D. *Phys. Rev. B* **1976**, *13*, 5188–5192.
28. Makov, G.; Payne, M. C. *Phys. Rev. B* **1995**, *51*, 4014–4022.
29. Henkelman, G.; Uberuaga, B. P.; Jonsson, H. *J. Chem. Phys.* **2000**, *113*, 9901–9904.
30. Henkelman, G.; Jonsson, H. *J. Chem. Phys.* **1999**, *111*, 7010–7022.
31. Heyden, A.; Bell, A. T.; Keil, F. J. *J. Chem. Phys.* **2005**, *123*, 224101.
32. Faheem, M.; Suthirakun, S.; Heyden, A. *J. Phys. Chem. C* **2012**, *116*, 22458–22462.
33. TURBOMOLE V6.4 2012, a development of University of Karlsruhe and Forschungszentrum Karlsruhe GmbH, 1989–2007, TURBOMOLE GmbH, since 2007.
34. Ahlrichs, R.; Bar, M.; Haser, M.; Horn, H.; Kolmel, C. *Chem. Phys. Lett.* **1989**, *162*, 165–169.
35. Schafer, A.; Huber, C.; Ahlrichs, R. *J. Chem. Phys.* **1994**, *100*, 5829–5835.
36. Weigend, F.; Ahlrichs, R. *Phys. Chem. Chem. Phys.* **2005**, *7*, 3297–3305.
37. Perdew, J. P. *Phys. Rev. B* **1986**, *33*, 8822–8824.
38. Becke, A. D. *Phys. Rev. A* **1988**, *38*, 3098–3100.
39. Weigend, F. *Phys. Chem. Chem. Phys.* **2006**, *8*, 1057–1065.
40. Eichkorn, K.; Weigend, F.; Treutler, O.; Ahlrichs, R. *Theor. Chem. Acc.* **1997**, *97*, 119–124.
41. Klamt, A.; Schuurmann, G. *J. Chem. Soc., Perkin Trans. 2* **1993**, 799–805.
42. Schafer, A.; Klamt, A.; Sattel, D.; Lohrenz, J. C. W.; Eckert, F. *Phys. Chem. Chem. Phys.* **2000**, *2*, 2187–2193.
43. Klamt, A. *J. Phys. Chem.* **1995**, *99*, 2224–2235.
44. Klamt, A. *COSMO-RS: From Quantum Chemistry to Fluid Phase Thermodynamics and Drug Design*. Elsevier Science Ltd.: Amsterdam, The Netherlands, 2005.
45. Pechukas, P. *Annu. Rev. Phys. Chem.* **1981**, *32*, 159–177.
46. McQuarrie, D. A. *Statistical Mechanics*. University Science Books: Sausalito, CA, 2000.
47. Buzzi-Ferraris, G.; Manenti, F. BzzMath: Library Overview and Recent Advances in Numerical Methods. In *Computer Aided Chemical Engineering*, Bogle, I. D. L.; Fairweather, M., Eds. Elsevier: 2012; Vol. 30, pp 1312–1316.
48. Rubert-Nason, P.; Mavrikakis, M.; Maravelias, C. T.; Grabow, L. C.; Biegler, L. T. *AIChE J.* **2014**, *60*, 1336–1346.
49. Kandoi, S.; Greeley, J.; Sanchez-Castillo, M. A.; Evans, S. T.; Gokhale, A. A.; Dumesic, J. A.; Mavrikakis, M. *Top. Catal.* **2006**, *37*, 17–28.
50. Grabow, L. C.; Hvolbaek, B.; Norskov, J. K. *Top. Catal.* **2010**, *53*, 298–310.
51. Saliccioli, M.; Chen, Y.; Vlachos, D. G. *J. Phys. Chem. C* **2010**, *114*, 20155–20166.
52. Greeley, J.; Mavrikakis, M. *J. Am. Chem. Soc.* **2002**, *124*, 7193–7201.
53. Mhadeshwar, A. B.; Vlachos, D. G. *Catal. Today* **2005**, *105*, 162–172.
54. Campbell, C. T. *J. Catal.* **2001**, *204*, 520–524.
55. Stegelmann, C.; Andreasen, A.; Campbell, C. T. *J. Am. Chem. Soc.* **2009**, *131*, 8077–8082.
56. Stegelmann, C.; Andreasen, A.; Campbell, C. T. *J. Am. Chem. Soc.* **2009**, *131*, 13563–13563
Erratum.
57. Klimes, J.; Michaelides, A. *J. Chem. Phys.* **2012**, *137*, 120901.
58. Grimme, S.; Antony, J.; Ehrlich, S.; Krieg, H. *J. Chem. Phys.* **2010**, *132*, 154104.

Table 6.1. Lateral interaction parameters used in the microkinetic model.

Adsorbate Pair	Lateral Interaction (eV)
CO-CO	$1.0916(\theta_{\text{CO}} - 0.0296)$
H-H	$0.1414(\theta_{\text{H}} - 0.0227)$
CO-H	$(0.3185 + 0.3850\sqrt{\theta_{\text{CO}}^* \theta_{\text{H}}^*})\theta_{\text{H}}^*$
X-X ^a	$1.0916\theta_{\text{X}}$
X-CO	$0.1086\theta_{\text{CO}}$
X-H	$0.0211\theta_{\text{H}}$

^a X stands for all surface intermediates and transition states excluding CO and H.

Table 6.2. Energetics (eV) of surface reactions in the limit of zero coverage.

ID	Reaction	Zero-point Corrected		Vapor Phase (500 K)		Aqueous Phase (500 K)	
		ΔE^\ddagger	ΔE_{rxn}	ΔG^\ddagger	ΔG_{rxn}	ΔG^\ddagger	ΔG_{rxn}
CC01	$\text{CH}_2\text{OHCH}_2\text{OH}^{**} \rightarrow 2\text{CH}_2\text{OH}^*$	2.07	-0.20	2.10	-0.20	1.98	-0.21
CC02	$\text{CHOHCH}_2\text{OH}^{**} \rightarrow \text{CHOH}^* + \text{CH}_2\text{OH}^*$	1.34	-0.15	1.30	-0.18	1.24	-0.11
CC03	$\text{CH}_2\text{OCH}_2\text{OH}^{**} + * \rightarrow \text{CH}_2\text{O}^{**} + \text{CH}_2\text{OH}^*$	1.39	-0.37	1.39	-0.43	1.44	-0.32
CC04	$\text{COHCH}_2\text{OH}^{***} \rightarrow \text{COH}^* + \text{CH}_2\text{OH}^* + *$	1.42	-0.31	1.35	-0.38	1.34	-0.45
CC05	$\text{CHOHCHOH}^{**} \rightarrow 2\text{CHOH}^*$	1.02	-0.12	1.02	-0.09	1.06	+0.02
CC06	$\text{CHOCH}_2\text{OH}^{***} \rightarrow \text{CHO}^* + \text{CH}_2\text{OH}^* + *$	1.23	-0.59	1.22	-0.74	1.21	-0.70
CC07	$\text{CHOHCH}_2\text{O}^{**} + * \rightarrow \text{CHOH}^* + \text{CH}_2\text{O}^{**}$	0.80	-0.23	0.79	-0.28	0.76	-0.23
CC08	$\text{CH}_2\text{OCH}_2\text{O}^{**} + 2* \rightarrow 2\text{CH}_2\text{O}^{**}$	0.61	-0.38	0.56	-0.45	0.39	-0.45
CC09	$\text{COCH}_2\text{OH}^{**} \rightarrow \text{CO}^* + \text{CH}_2\text{OH}^*$	0.66	-0.92	0.63	-0.95	0.69	-0.89
CC10	$\text{COHCHOH}^{**} \rightarrow \text{COH}^* + \text{CHOH}^*$	1.12	-0.23	1.09	-0.25	1.03	-0.27
CC11	$\text{COHCH}_2\text{O}^{**} + * \rightarrow \text{COH}^* + \text{CH}_2\text{O}^{**}$	1.05	-0.35	1.03	-0.39	1.02	-0.42
CC12	$\text{CHOCHOH}^{***} \rightarrow \text{CHO}^* + \text{CHOH}^* + *$	0.96	-0.51	0.90	-0.60	0.90	-0.56
CC13	$\text{CHOCH}_2\text{O}^{***} \rightarrow \text{CHO}^* + \text{CH}_2\text{O}^{**}$	0.45	-0.72	0.46	-0.84	0.48	-0.78
CC14	$\text{COCHOH}^{**} \rightarrow \text{CO}^* + \text{CHOH}^*$	0.41	-0.97	0.39	-0.97	0.46	-0.93
CC15	$\text{COCH}_2\text{O}^{**} + * \rightarrow \text{CO}^* + \text{CH}_2\text{O}^{**}$	0.31	-0.82	0.32	-0.84	0.33	-0.85

Table 6.2 continued

ID	Reaction	Zero-point Corrected		Vapor Phase (500 K)		Aqueous Phase (500 K)	
		ΔE^\ddagger	ΔE_{rxn}	ΔG^\ddagger	ΔG_{rxn}	ΔG^\ddagger	ΔG_{rxn}
CC16	COHCOH** → 2COH*	1.08	-0.48	1.06	-0.48	1.01	-0.58
CC17	COHCHO** → COH*+CHO*	0.95	-0.64	0.87	-0.72	0.79	-0.80
CC18	CHOCHO**** → 2CHO*+2*	0.91	-0.94	0.79	-1.14	0.78	-1.11
CC19	COCO** → CO*+COH*	0.64	-0.98	0.58	-1.00	0.58	-1.05
CC20	COCHO*** → CO*+CHO*+*	0.44	-1.30	0.38	-1.41	0.38	-1.39
CC21	COCO** → 2CO*	0.02	-1.76	0.03	-1.76	0.05	-1.76
CH01	CH ₂ OHCH ₂ OH***+* → CHOCH ₂ OH**+H*	0.75	-0.48	0.83	-0.40	0.75	-0.39
CH02	CHOHCH ₂ OH**+2* → COHCH ₂ OH***+H*	0.37	-0.41	0.38	-0.36	0.40	-0.29
CH03	CHOHCH ₂ OH**+* → CHOHCHOH**+H*	0.35	-0.47	0.37	-0.46	0.34	-0.43
CH04	CH ₂ OCH ₂ OH**+2* → CHOCH ₂ OH***+H*	0.11	-0.69	0.10	-0.64	0.07	-0.52
CH05	CH ₂ OCH ₂ OH**+* → CHOHCH ₂ O***+H*	0.34	-0.57	0.33	-0.53	0.37	-0.39
CH06	COHCH ₂ OH*** → COHCHOH**+H*	0.65	-0.51	0.64	-0.51	0.47	-0.47
CH07	CHOHCHOH**+* → COHCHOH**+H*	0.54	-0.45	0.58	-0.41	0.61	-0.33
CH08	CHOCH ₂ OH*** → COCH ₂ OH**+H*	0.37	-0.83	0.27	-0.90	0.31	-0.88
CH09	CHOCH ₂ OH***+* → CHOCHOH***+H*	0.55	-0.52	0.46	-0.52	0.45	-0.43

Table 6.2 continued

ID	Reaction	Zero-point Corrected		Vapor Phase (500 K)		Aqueous Phase (500 K)	
		ΔE^\ddagger	ΔE_{rxn}	ΔG^\ddagger	ΔG_{rxn}	ΔG^\ddagger	ΔG_{rxn}
CH10	$\text{CHOHCH}_2\text{O}^{**+*} \rightarrow \text{COHCH}_2\text{O}^{**} + \text{H}^*$	0.56	-0.44	0.57	-0.45	0.55	-0.43
CH11	$\text{CHOHCH}_2\text{O}^{**+2*} \rightarrow \text{CHOCHOH}^{***} + \text{H}^*$	0.05	-0.64	0.06	-0.63	0.05	-0.57
CH12	$\text{CH}_2\text{OCH}_2\text{O}^{**+2*} \rightarrow \text{CHOCH}_2\text{O}^{***} + \text{H}^*$	0.19	-0.58	0.21	-0.57	0.19	-0.58
CH13	$\text{COHCHOH}^{**+*} \rightarrow \text{COHCOH}^{**} + \text{H}^*$	0.71	-0.31	0.73	-0.33	0.67	-0.32
CH14	$\text{COCH}_2\text{OH}^{**+*} \rightarrow \text{COCHOH}^{**} + \text{H}^*$	0.59	-0.38	0.61	-0.36	0.68	-0.26
CH15	$\text{CHOCHOH}^{***} \rightarrow \text{COCHOH}^{**} + \text{H}^*$	0.27	-0.70	0.21	-0.74	0.19	-0.71
CH16	$\text{CHOCHOH}^{***} \rightarrow \text{COHCHO}^{**} + \text{H}^*$	0.34	-0.44	0.33	-0.45	0.34	-0.39
CH17	$\text{COHCH}_2\text{O}^{**+*} \rightarrow \text{COHCHO}^{**} + \text{H}^*$	0.14	-0.63	0.16	-0.63	0.18	-0.53
CH18	$\text{CHOCH}_2\text{O}^{***} \rightarrow \text{COCH}_2\text{O}^{**} + \text{H}^*$	0.14	-1.07	0.14	-1.10	0.17	-1.00
CH19	$\text{CHOCH}_2\text{O}^{***+2*} \rightarrow \text{CHOCHO}^{****} + \text{H}^*$	0.00	-0.70	0.04	-0.65	0.07	-0.57
CH20	$\text{COCHOH}^{**+*} \rightarrow \text{COCOH}^{**} + \text{H}^*$	0.49	-0.56	0.50	-0.53	0.48	-0.50
CH21	$\text{COHCHO}^{**+*} \rightarrow \text{COCOH}^{**} + \text{H}^*$	0.29	-0.81	0.30	-0.82	0.30	-0.82
CH22	$\text{COCH}_2\text{O}^{**+2*} \rightarrow \text{COCHO}^{***} + \text{H}^*$	0.16	-0.43	0.18	-0.39	0.18	-0.36
CH23	$\text{CHOCHO}^{****} \rightarrow \text{COCHO}^{***} + \text{H}^*$	0.10	-0.80	0.08	-0.84	0.10	-0.79
CH24	$\text{COCHO}^{***} \rightarrow \text{COCO}^{**} + \text{H}^*$	0.39	-0.71	0.36	-0.75	0.38	-0.70

Table 6.2 continued

ID	Reaction	Zero-point Corrected		Vapor Phase (500 K)		Aqueous Phase (500 K)	
		ΔE^\ddagger	ΔE_{rxn}	ΔG^\ddagger	ΔG_{rxn}	ΔG^\ddagger	ΔG_{rxn}
CH25	$\text{CH}_3\text{OH}^{*+*} \rightarrow \text{CH}_2\text{OH}^* + \text{H}^*$	0.46	-0.43	0.48	-0.38	0.48	-0.31
CH26	$\text{CH}_3\text{O}^* + 2^* \rightarrow \text{CH}_2\text{O}^{**} + \text{H}^*$	0.08	-0.56	0.17	-0.50	0.17	-0.46
CH27	$\text{CH}_2\text{OH}^{*+*} \rightarrow \text{CHOH}^* + \text{H}^*$	0.37	-0.43	0.40	-0.38	0.41	-0.30
CH28	$\text{CH}_2\text{O}^{**} \rightarrow \text{CHO}^* + \text{H}^*$	0.34	-0.92	0.32	-0.96	0.33	-0.90
CH29	$\text{CHOH}^{*+*} \rightarrow \text{COH}^* + \text{H}^*$	0.34	-0.57	0.36	-0.57	0.32	-0.63
CH30	$\text{CHO}^{*+*} \rightarrow \text{CO}^* + \text{H}^*$	0.15	-1.16	0.21	-1.10	0.24	-1.07
OH01	$\text{CH}_2\text{OHCH}_2\text{OH}^{***} \rightarrow \text{CH}_2\text{OCH}_2\text{OH}^{**} + \text{H}^*$	0.63	+0.40	0.71	+0.48	0.70	+0.39
OH02	$\text{CH}_2\text{OCH}_2\text{OH}^{***} \rightarrow \text{CH}_2\text{OCH}_2\text{O}^{**} + \text{H}^*$	0.53	+0.23	0.58	+0.27	0.69	+0.41
OH03	$\text{CHOHCH}_2\text{OH}^{**} + 2^* \rightarrow \text{CHOCH}_2\text{OH}^{***} + \text{H}^*$	0.73	+0.18	0.75	+0.23	0.73	+0.26
OH04	$\text{CHOHCH}_2\text{OH}^{***} \rightarrow \text{CHOHCH}_2\text{O}^{**} + \text{H}^*$	0.89	+0.30	0.94	+0.35	0.97	+0.39
OH05	$\text{CHOCH}_2\text{OH}^{***} \rightarrow \text{CHOCH}_2\text{O}^{***} + \text{H}^*$	0.75	+0.35	0.79	+0.34	0.80	+0.36
OH06	$\text{CHOHCH}_2\text{O}^{**} + 2^* \rightarrow \text{CHOCH}_2\text{O}^{***} + \text{H}^*$	0.95	+0.23	0.94	+0.23	0.95	+0.23
OH07	$\text{COHCH}_2\text{OH}^{***} \rightarrow \text{COCH}_2\text{OH}^{**} + \text{H}^*$	0.20	-0.24	0.19	-0.30	0.12	-0.34
OH08	$\text{COHCH}_2\text{OH}^{***} \rightarrow \text{COHCH}_2\text{O}^{**} + \text{H}^*$	0.52	+0.26	0.57	+0.25	0.58	+0.25
OH09	$\text{CHOHCHOH}^{**} + 2^* \rightarrow \text{CHOCHOH}^{***} + \text{H}^*$	0.60	+0.12	0.64	+0.17	0.67	+0.26

Table 6.2 continued

ID	Reaction	Zero-point Corrected		Vapor Phase (500 K)		Aqueous Phase (500 K)	
		ΔE^\ddagger	ΔE_{rxn}	ΔG^\ddagger	ΔG_{rxn}	ΔG^\ddagger	ΔG_{rxn}
OH10	$\text{COCH}_2\text{OH}^{***} \rightarrow \text{COCH}_2\text{O}^{***} + \text{H}^*$	0.45	+0.11	0.52	+0.14	0.59	+0.25
OH11	$\text{COHCH}_2\text{O}^{***} \rightarrow \text{COCH}_2\text{O}^{***} + \text{H}^*$	0.11	-0.39	0.13	-0.42	0.19	-0.34
OH12	$\text{CHOCHOH}^{***} + 2^* \rightarrow \text{CHOCHO}^{****} + \text{H}^*$	0.80	+0.17	0.80	+0.20	0.73	+0.22
OH13	$\text{COHCHOH}^{**} + ^* \rightarrow \text{COCHOH}^{**} + \text{H}^*$	0.41	-0.12	0.41	-0.16	0.41	-0.12
OH14	$\text{COHCHOH}^{**} + ^* \rightarrow \text{COHCHO}^{**} + \text{H}^*$	0.71	+0.14	0.72	+0.13	0.69	+0.20
OH15	$\text{COCHOH}^{**} + 2^* \rightarrow \text{COCHO}^{***} + \text{H}^*$	0.54	+0.07	0.62	+0.11	0.62	+0.14
OH16	$\text{COHCHO}^{**} + 2^* \rightarrow \text{COCHO}^{***} + \text{H}^*$	0.41	-0.19	0.44	-0.18	0.43	-0.18
OH17	$\text{COHCOH}^{**} + ^* \rightarrow \text{COCOH}^{**} + \text{H}^*$	0.47	-0.36	0.50	-0.35	0.49	-0.30
OH18	$\text{COCOH}^{**} + ^* \rightarrow \text{COCO}^{**} + \text{H}^*$	0.43	-0.08	0.45	-0.12	0.45	-0.06
OH19	$\text{CH}_3\text{OH}^{**} + ^* \rightarrow \text{CH}_3\text{O}^{**} + \text{H}^*$	0.65	+0.36	0.72	+0.36	0.75	+0.43
OH20	$\text{CH}_2\text{OH}^{**} + 2^* \rightarrow \text{CH}_2\text{O}^{**} + \text{H}^*$	0.61	+0.22	0.67	+0.25	0.69	+0.28
OH21	$\text{CHOH}^{**} + ^* \rightarrow \text{CHO}^{**} + \text{H}^*$	0.36	-0.27	0.35	-0.34	0.29	-0.33
OH22	$\text{COH}^{**} + ^* \rightarrow \text{CO}^{**} + \text{H}^*$	0.53	-0.86	0.55	-0.87	0.63	-0.77

Table 6.3. Energetics (eV) of adsorption reactions in the limit of zero coverage.

ID	Reaction	Zero-point Corrected ΔE_{rxn}		Vapor Phase ΔG_{rxn} (500 K)		Aqueous Phase ΔG_{rxn} (500 K)	
		PBE	PBE-D3	PBE	PBE-D3	PBE	PBE-D3
AD01	$\text{CH}_2\text{OHCH}_2\text{OH} + 2^* \rightarrow \text{CH}_2\text{OHCH}_2\text{OH}^{**}$	-0.46	-1.14	+0.58	-0.07	+0.52	-0.13
AD02	$\text{CH}_3\text{OH} + ^* \rightarrow \text{CH}_3\text{OH}^*$	-0.27	-0.69	+0.65	+0.21	+0.58	+0.15
AD03	$\text{CO} + ^* \rightarrow \text{CO}^*$	-1.79	-2.02	-0.98	-1.22	-1.00	-1.25
AD04	$\text{H}_2 + 2^* \rightarrow 2\text{H}^*$	-0.96	-1.06	-0.40	-0.49	-0.32	-0.41

Table 6.4. Kinetic properties at 500 K for vapor- and aqueous-phase reforming of ethylene glycol over Pt (111).

Property	Vapor Phase		Aqueous Phase	
	Model	Literature	Model	Literature
Apparent activation energy (eV)	1.52	0.83 ^a , 1.35 ^b , 0.59 ^c	1.15	1.04 ^d
Carbon monoxide order	-0.58	-0.4 ^a , -0.4 ^b , -0.54 ^c	-0.61	
Hydrogen order	-0.84		-0.47	-0.5 ^d
Ethylene glycol order	1.0	0.4 ^a , 0.05 ^b , 0.38 ^c	1.0	0.3-0.5 ^d
Total pressure order	-0.13	-0.10 ^a , -0.02 ^b , -0.26 ^c	-1.89	-2.5 ^d

^a Experimental data¹⁰

^b Model predictions¹⁰

^c Model predictions¹⁴

^d Experimental data²¹

Table 6.5. Sensitivity analysis for vapor- and aqueous-phase reforming of ethylene glycol over Pt (111).

	Vapor Phase			Aqueous Phase		
	425 K	500 K	525 K	425 K	500 K	525 K
Degree of rate control						
$\text{CH}_2\text{OHCH}_2\text{OH}^{**+*} \rightarrow \text{CHOHCH}_2\text{OH}^{**} + \text{H}^*$	0.23	0.16	0.14	0.26	0.26	0.27
$\text{CH}_2\text{OHCH}_2\text{OH}^{**+*} \rightarrow \text{CH}_2\text{OCH}_2\text{OH}^{**} + \text{H}^*$	0.19	0.35	0.51	0.66	0.69	0.70
$\text{CH}_2\text{OCH}_2\text{OH}^{**} + 2^* \rightarrow \text{CHOCH}_2\text{OH}^{***} + \text{H}^*$	0.56	0.47	0.34	0.07	0.04	0.03
$\text{CH}_2\text{OCH}_2\text{OH}^{**+*} \rightarrow \text{CHOHCH}_2\text{O}^{**} + \text{H}^*$	0.02	0.01	0.01			
Degree of thermodynamic rate control						
H^*	-1.04	-0.83	-0.66	-0.68	-0.53	-0.44
CO^*	-0.50	-0.44	-0.39	-0.44	-0.39	-0.36
COH^*	-0.09	-0.02	-0.01	-0.21	-0.09	-0.03

Table 6.6. Summary of vapor- and aqueous-phase microkinetic model predictions with dispersion effects included.

Property	Vapor Phase	Aqueous Phase
Apparent activation energy (eV)	1.04	0.85
Carbon monoxide order	-0.45	-0.32
Hydrogen order	-1.01	-0.67
Ethylene glycol order	0.63	0.24
Total pressure order	-0.48	-0.34
Surface coverage at 500 K		
CO*	48%	57%
H*	43%	32%
*	7%	7%
CH ₂ OHCH ₂ OH**	0.4%	0.9%

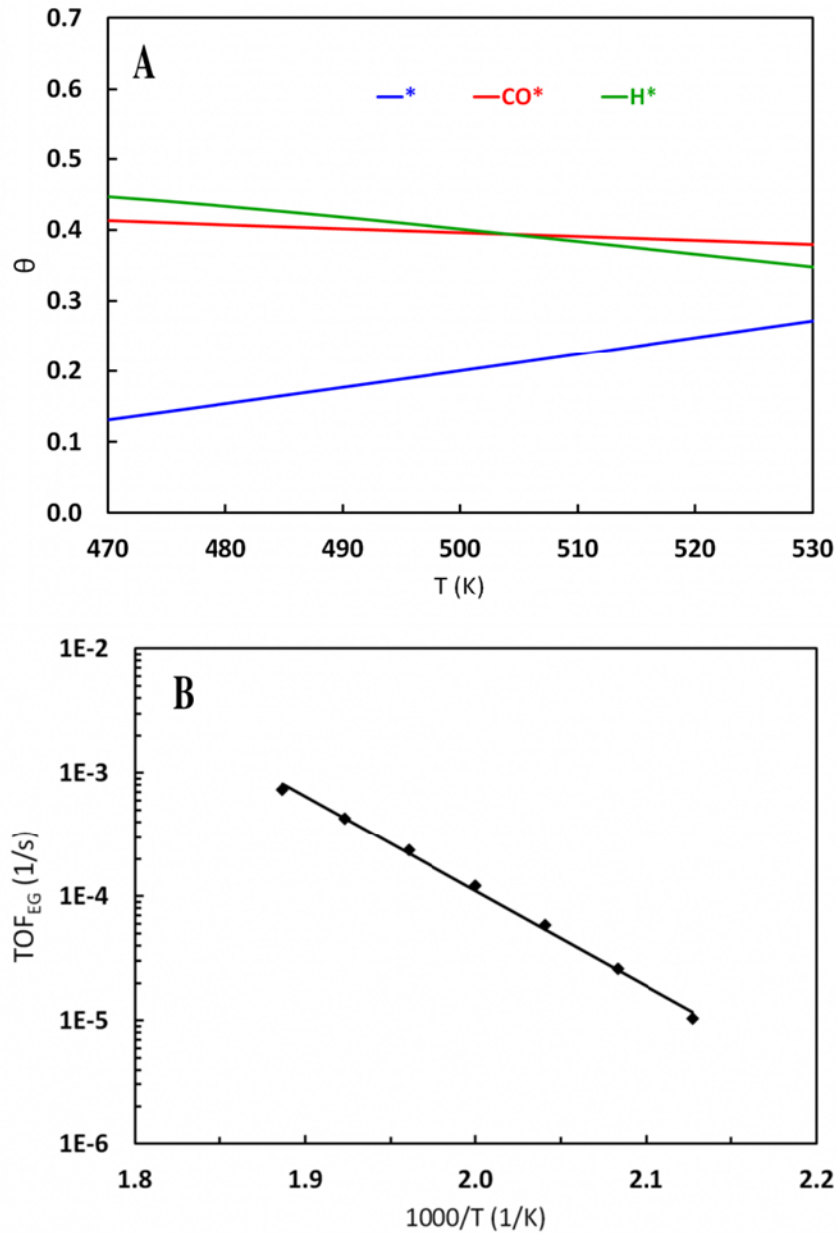


Figure 6.1. Effect of temperature on coverage of most abundant surface intermediates (A), and overall turnover frequency (B) in vapor-phase reforming of ethylene glycol over Pt (111).

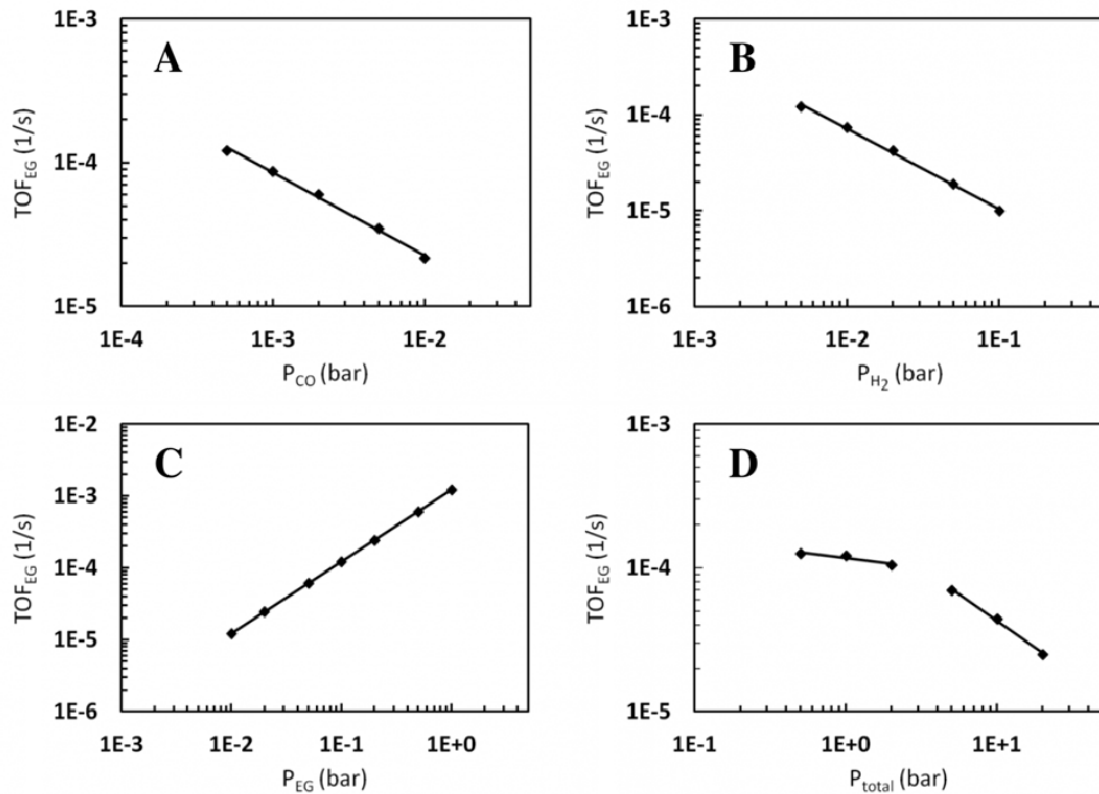


Figure 6.2. Effect of carbon monoxide partial pressure (A), hydrogen partial pressure (B), ethylene glycol partial pressure (C), and total pressure (D) on overall turnover frequency in vapor-phase reforming of ethylene glycol over Pt (111) at 500 K.

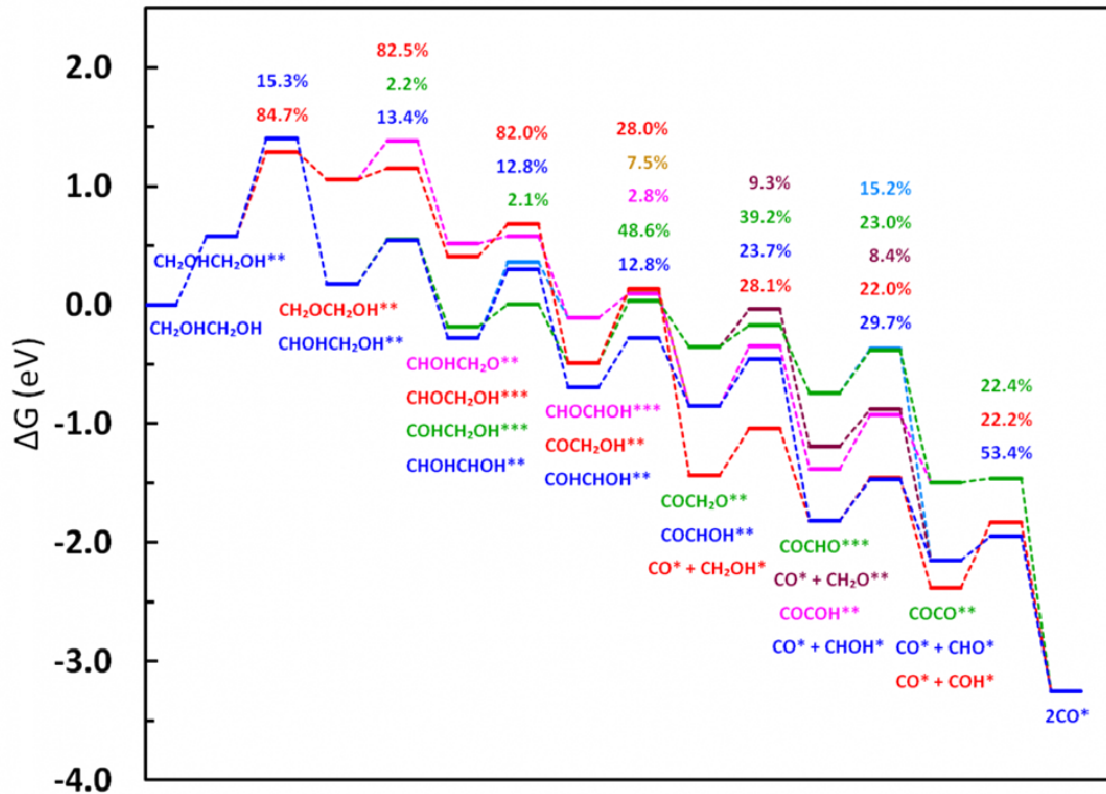


Figure 6.3. Free energy diagram at 500 K for vapor-phase reforming of ethylene glycol over Pt in the limit of zero coverage. Species labels show surface intermediates sorted (top to bottom) in order of increasing stability. Percent labels show fraction of the overall reaction flux passing through different pathways and are sorted (top to bottom) in order of increasing stability of respective transition states. Only those pathways are labeled that contribute more than 2% of the overall reaction flux. Excess hydrogen atoms are adsorbed on separate slabs and omitted from labels for simplicity.

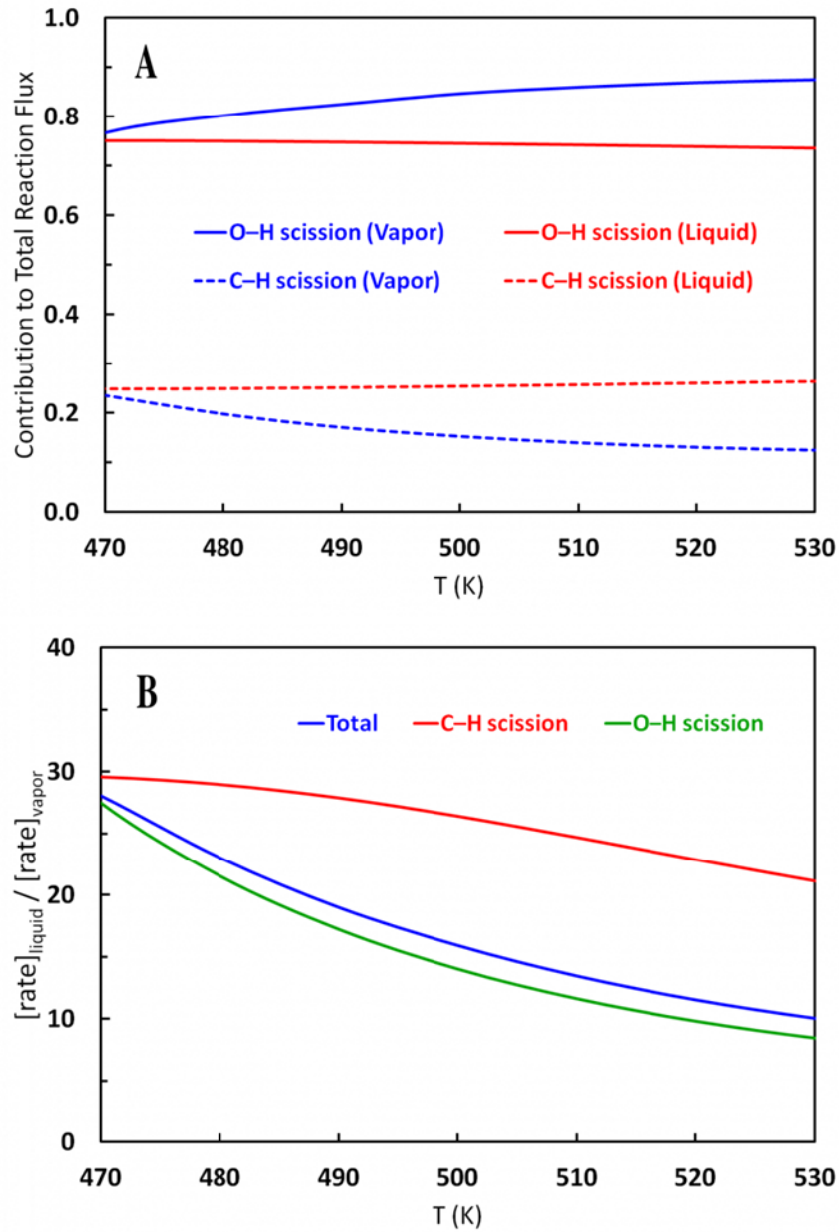


Figure 6.4. Comparison of vapor- and aqueous-phase reforming of ethylene glycol over Pt (111). (A) Contribution of initial C–H and O–H scission pathways to total rate of ethylene glycol decomposition. (B) Ratio of reaction rates in aqueous and vapor phases.

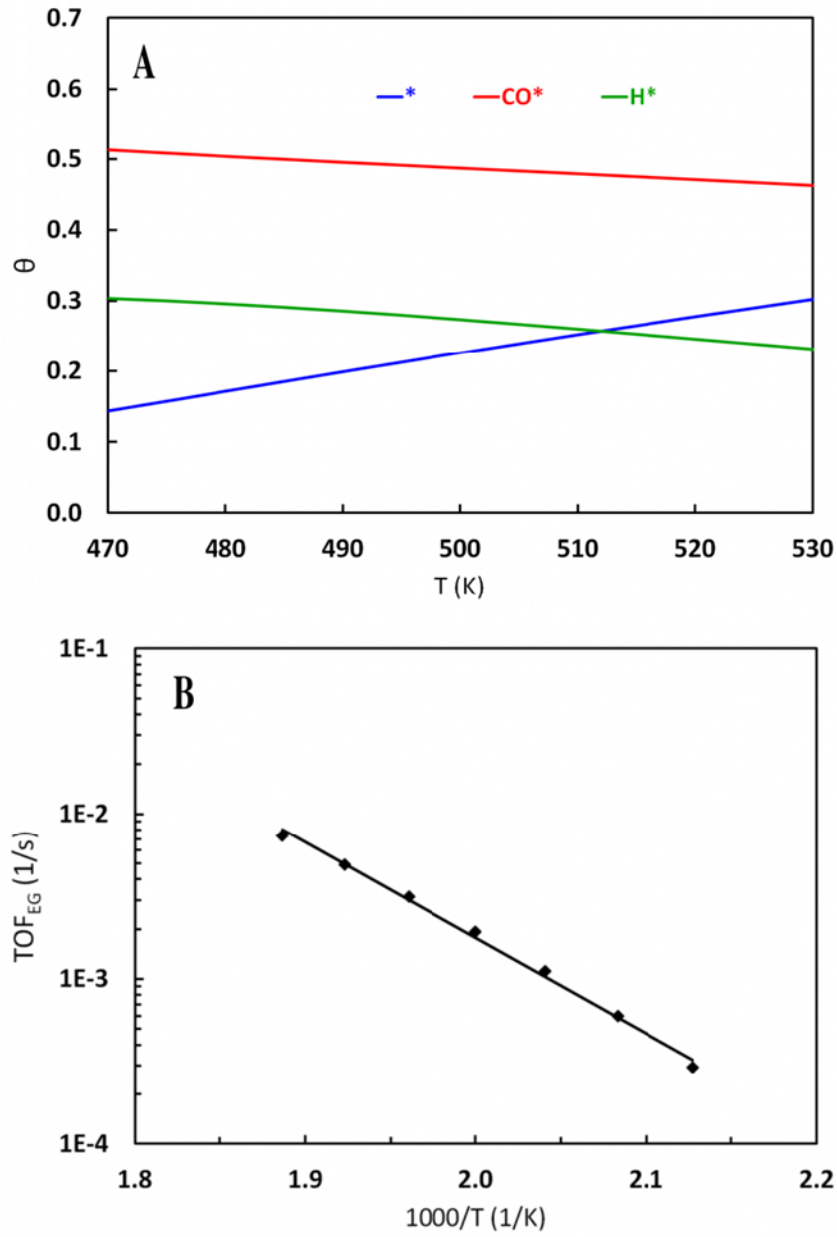


Figure 6.5. Effect of temperature on surface coverages of most abundant intermediates (A) and overall turnover frequency (B) in aqueous-phase reforming of ethylene glycol over Pt (111).

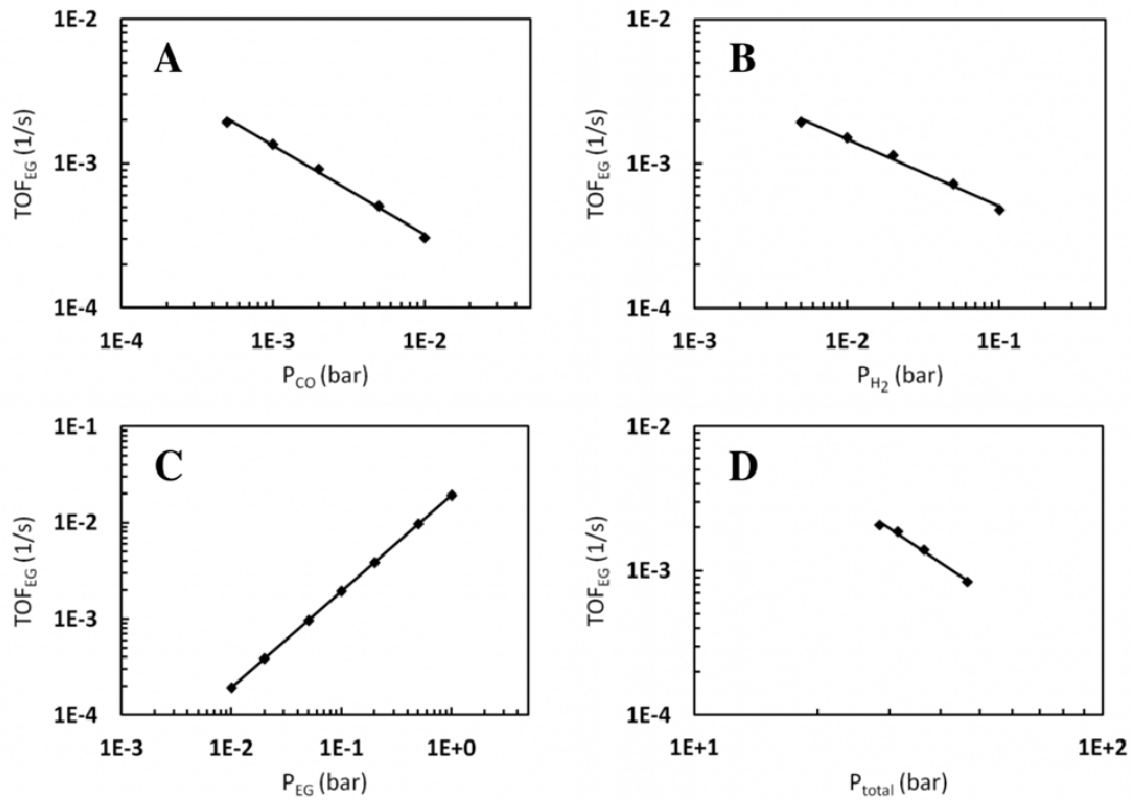


Figure 6.6. Effect of carbon monoxide partial pressure (A), hydrogen partial pressure (B), ethylene glycol partial pressure (C), and total pressure (D) on overall turnover frequency in aqueous-phase reforming of ethylene glycol over Pt (111) at 500 K.

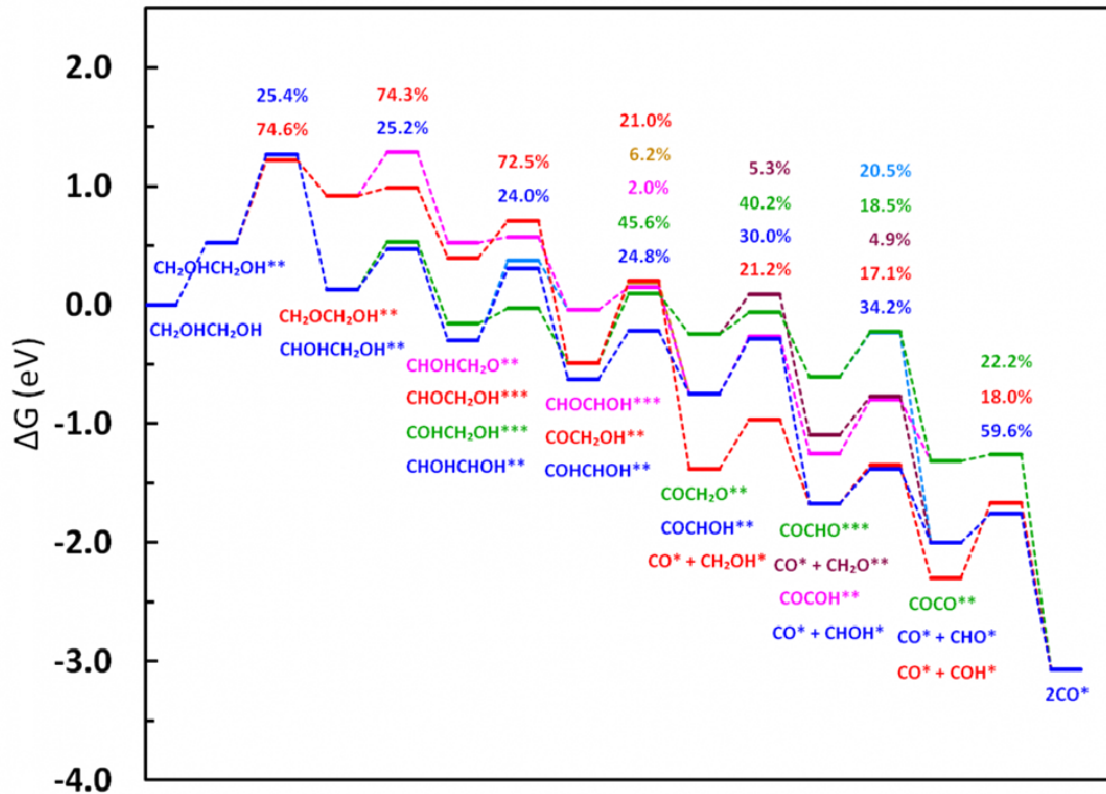


Figure 6.7. Free energy diagram at 500 K for aqueous-phase reforming of ethylene glycol over Pt in the limit of zero coverage. Species labels show surface intermediates sorted (top to bottom) in order of increasing stability. Percent labels show fraction of the overall reaction flux passing through different pathways and are sorted (top to bottom) in order of increasing stability of respective transition states. Only those pathways are labeled that contribute more than 2% of the overall reaction flux. Excess hydrogen atoms are adsorbed on separate slabs and omitted from labels for simplicity.

CHAPTER 7

CONCLUSIONS AND FUTURE RESEARCH DIRECTIONS

7.1. Conclusions

The catalytic conversion of biomass to fuels and chemicals is a promising strategy to ease the growing concerns surrounding global warming and long term sustainability of a fossil fuel economy. Aqueous-phase processing of lignocellulosic biomass derived oxygenated hydrocarbons over supported transition metal catalysts for production of hydrogen and targeted molecular weight alkanes is particularly attractive. Rational catalyst design for such processes has however been hindered by an inadequate understanding of heterogeneous catalysis in an aqueous environment.

This dissertation presented a case study for the application of first-principles calculations for systematic investigation of complex reaction pathways at a metal–water interface. In the first part of this dissertation, novel QM/MM methods were developed to account for the effects of an aqueous environment on reaction moieties adsorbed on a metal slab. Specifically, periodic planewave DFT calculations were integrated with a nonperiodic continuum solvation model (implicit solvation) and with molecular dynamics simulations (explicit solvation). Both approaches were systematically validated against the results of *ab initio* QM calculations. The main conclusions drawn from this part of the work are:

- (1) The effect of water on the bonding characteristics of transition metal surfaces with adsorbates is short ranged. As a result, adsorption energies in water can be evaluated by a combination of periodic DFT calculations in vacuum and properly chosen cluster model calculations in solvent.
- (2) The QM cluster must include all metal atoms forming the adsorption site and their nearest neighbors (in surface plane as well as in the next layer). Convergence is achieved for small metal clusters and basis sets.
- (3) Carbon monoxide binds more strongly to Pt (111) and Pd (111) in water leading to a red shift in CO stretching frequency. This is due to an indirect electronic effect of water on the metal atoms forming the adsorption site and can be explained by an increased π back-donation from the metal surface to the adsorbed CO molecule.
- (4) C–C bond scission in dehydrogenated ethylene glycol is hindered in water and can be explained by changes in intramolecular hydrogen bonding. Both implicit and explicit solvation schemes are in good agreement. An explicit solvation scheme is able to account for site-specific interactions and predicts larger structural changes in water.
- (5) The computational cost of implicit solvation is comparable to planewave (vacuum) calculations whereas explicit solvation (QM/MM-FEP) is 1–2 orders of magnitude more expensive.

In the second part of this dissertation, reaction pathways in Pt catalyzed ethylene glycol reforming in vapor and aqueous phases were systematically investigated. The main conclusions drawn from this part of the work are:

- (1) Initial dehydrogenation steps are rate controlling in the ethylene glycol decomposition over Pt (111). The dominant pathway is always through initial O–H scission, but the pathway through initial C–H scission also remains kinetically relevant at all temperatures. The reforming mechanism is highly selective toward complete decomposition to H₂ and CO.
- (2) C–C bond cleavage reactions are not rate limiting, occur only after a significant dehydrogenation and almost exclusively in those intermediates where one of the cleavage products is CO.
- (3) An aqueous environment increases the rate of decomposition by lowering the activation energy. The initial C–H cleaving transition state is disproportionately stabilized in water, resulting in a larger contribution of this pathway to the total reaction flux. However, the pathway through initial O–H bond cleavage remains dominant.
- (4) The dominant surface intermediates and rate controlling elementary steps are the same in both vapor and aqueous phases. Reaction fluxes through various pathways and respective sensitivity coefficients are also comparable, indicating that the reforming chemistry on platinum is similar in both phases.

A three-step procedure can be envisioned for simulating complex heterogeneously catalyzed reaction networks in aqueous environments:

- (1) Planewave DFT calculations (complete reaction network)
- (2) Implicit solvation (complete reaction network) and microkinetic modeling to perform a preliminary screening to identify those surface intermediates and

elementary reactions that are kinetically important and most sensitive to an aqueous environment.

- (3) Explicit solvation (important elementary steps) to refine the description of the liquid phase.

7.2. Future Research Directions

Development and validation of new computational approaches for simulating chemical reactions at metal–water interfaces have been the primary focus of this dissertation. Other areas of interest identified from this work include:

- (1) The QM/MM-FEP method (Chapter 5) is currently limited to surface reactions. Adsorption of a molecule from the gas phase on to a metal slab would require creation or annihilation of atoms during these simulations and is not achievable in the current development. Considering that these effects can be relatively easily described using a thermodynamic integration (TI) approach, a QM/MM-TI method is needed for simulating adsorption–desorption processes.
- (2) As pointed out in section 2.3, an alternative pathway for ethylene glycol decomposition proceeds through selective cleavage of C–O bonds and leads to the formation of alkanes. Considering that the effects of an aqueous environment are likely stronger on a heterolytic bond cleavage (C–O) compared to a homolytic bond cleavage (C–C), this pathway should be explored to obtain insights into the selectivity challenges in vapor and aqueous phases.
- (3) Linear scaling relationships are widely used for estimating adsorbate binding energies and activation barriers for reactions at metal–gas interfaces. It may be possible to identify similar general descriptors in aqueous phase.

APPENDIX A

SUPPLEMENTARY INFORMATION FOR CHAPTER 4

Table A.1. Results from periodic-slab calculations (vacuum) for CO on Pd (111) and Pt (111) with PBE functional.

	$\Delta\nu_{\text{C-O}}$ (cm^{-1})	E_{ads} (kcal / mol)	$\Delta L_{\text{C-O}}$ (\AA)	$\Delta L_{\text{C-M}}$ (\AA)
Pd (111)/top	2027	-32.26	115.77	186.89
Pd (111)/fcc	1766	-47.38	119.28	207.13
Pd (111)/hcp	1771	-46.83	119.31	207.01
Pt (111)/top	2053	-39.16	115.79	184.98
Pt (111)/fcc	1745	-42.58	119.73	210.97
Pt (111)/hcp	1754	-41.55	119.62	211.08

Table A.2. Results from iSMS calculations (water) for CO on Pd (111) and Pt (111) with PBE functional.

	N_{metal}	$\Delta\nu_{\text{C-O}}$ (cm^{-1})	G_{ads} (kcal/mol)	$\Delta L_{\text{C-O}}$ (pm)	$\Delta L_{\text{C-M}}$ (pm)
Pd (111)/top	19	2025	-31.53	115.93	186.36
Pd (111)/fcc	24	1717	-48.79	120.21	206.11
Pd (111)/hcp	22	1716	-49.25	120.31	205.77
Pt (111)/top	19	2132	-38.93	115.73	184.81
Pt (111)/fcc	24	1696	-44.04	120.61	210.05
Pt (111)/hcp	22	1706	-42.92	120.51	209.82

Table A.3. Results from iSMS calculations (vacuum/water) for CO on Pd (111) and Pt (111) with PBE0 functional.

	N_{metal}	$\Delta v_{\text{C-O}}$ (cm^{-1})	$E_{\text{ads}}/G_{\text{ads}}$ (kcal / mol)	$\Delta L_{\text{C-O}}$ (pm)	$\Delta L_{\text{C-M}}$ (pm)
Calculations in vacuum					
Pd (111)/top	19	2140	-39.13	114.28	185.42
Pt (111)/top	19	2161	-57.31	114.28	183.54
Calculations in water					
Pd (111)/top	19	2096	-39.24	114.48	184.90
Pt (111)/top	19	2132	-59.31	114.29	183.39

APPENDIX B

SUPPLEMENTARY INFORMATION FOR CHAPTER 5

Table B.1. ESP-fitted and NPA charges for a 51-atom, Pt (111) cluster.

Atom ^a	Charge (au) ^b	
	ESP-fitted	NPA
Pt-1	0.0008 ± 0.027	0.0773 ± 0.008
Pt-2	-0.0001 ± 0.027	0.0823 ± 0.009
Pt-3	-0.0066 ± 0.030	0.0785 ± 0.007
Pt-4	0.0209 ± 0.018	-0.0940 ± 0.005
Pt-5	-0.0124 ± 0.025	0.0769 ± 0.007
Pt-6	0.0036 ± 0.022	0.0853 ± 0.006
Pt-7	0.0048 ± 0.018	-0.0269 ± 0.005
Pt-8	0.0009 ± 0.020	-0.0280 ± 0.004
Pt-9	0.0027 ± 0.023	0.0839 ± 0.006
Pt-10	-0.0115 ± 0.028	0.0956 ± 0.010
Pt-11	0.0327 ± 0.018	-0.0464 ± 0.005
Pt-12	-0.0464 ± 0.015	-0.0004 ± 0.004
Pt-13	0.0278 ± 0.023	-0.0459 ± 0.005
Pt-14	-0.0119 ± 0.029	0.0927 ± 0.010
Pt-15	0.0060 ± 0.024	0.0321 ± 0.008
Pt-16	0.0145 ± 0.019	-0.0448 ± 0.005
Pt-17	0.0130 ± 0.020	-0.0449 ± 0.005

Table B.1 continued

Atom ^a	Charge (au) ^b	
	ESP-fitted	NPA
Pt-18	0.0005 ± 0.026	0.0315 ± 0.006
Pt-19	-0.0134 ± 0.026	0.0930 ± 0.010
Pt-20	-0.0049 ± 0.024	0.0737 ± 0.007
Pt-21	-0.0118 ± 0.026	0.0916 ± 0.008
Pt-22	-0.0204 ± 0.046	-0.0544 ± 0.041
Pt-23	0.0162 ± 0.056	0.0390 ± 0.037
Pt-24	-0.0135 ± 0.048	-0.0487 ± 0.040
Pt-25	0.0123 ± 0.046	-0.0009 ± 0.033
Pt-26	-0.0156 ± 0.082	-0.0280 ± 0.025
Pt-27	0.0036 ± 0.064	-0.0212 ± 0.020
Pt-28	0.0077 ± 0.047	-0.0004 ± 0.030
Pt-29	-0.0005 ± 0.046	-0.0066 ± 0.034
Pt-30	-0.0281 ± 0.095	-0.0297 ± 0.030
Pt-31	0.0281 ± 0.086	-0.0487 ± 0.027
Pt-32	-0.0149 ± 0.081	-0.0260 ± 0.026
Pt-33	-0.0115 ± 0.052	-0.0165 ± 0.035
Pt-34	-0.0075 ± 0.053	-0.0409 ± 0.042
Pt-35	0.0115 ± 0.081	-0.0189 ± 0.023
Pt-36	-0.0054 ± 0.088	-0.0542 ± 0.025
Pt-37	0.0108 ± 0.076	-0.0474 ± 0.022
Pt-38	0.0126 ± 0.083	-0.0165 ± 0.029
Pt-39	-0.0184 ± 0.045	-0.0509 ± 0.038
Pt-40	0.0055 ± 0.054	0.0030 ± 0.033
Pt-41	-0.0196 ± 0.097	-0.0297 ± 0.034
Pt-42	0.0040 ± 0.089	-0.0491 ± 0.027

Table B.1 continued

Atom ^a	Charge (au) ^b	
	ESP-fitted	NPA
Pt-43	0.0008 ± 0.076	-0.0227 ± 0.028
Pt-44	0.0042 ± 0.067	0.0035 ± 0.041
Pt-45	0.0126 ± 0.043	0.0008 ± 0.030
Pt-46	0.0149 ± 0.086	-0.0160 ± 0.028
Pt-47	0.0070 ± 0.084	-0.0183 ± 0.031
Pt-48	0.0165 ± 0.073	0.0039 ± 0.045
Pt-49	-0.0175 ± 0.047	-0.0364 ± 0.038
Pt-50	0.0222 ± 0.046	0.0118 ± 0.034
Pt-51	-0.0268 ± 0.040	-0.0431 ± 0.031

^a Atoms 1–21 are in 2nd layer; atoms 22–51 are in top layer (exposed to water).

^b Average charges and standard deviations are computed using 50 representative water configurations, 2 ps apart.

Average time required for charge analysis using converged wavefunctions:

ESP-fitted charges: 52 minutes 37 seconds (±12.3 seconds)

NPA charges: 1 minute 6 seconds (±0.4 seconds)

APPENDIX C

SUPPLEMENTARY INFORMATION FOR CHAPTER 6

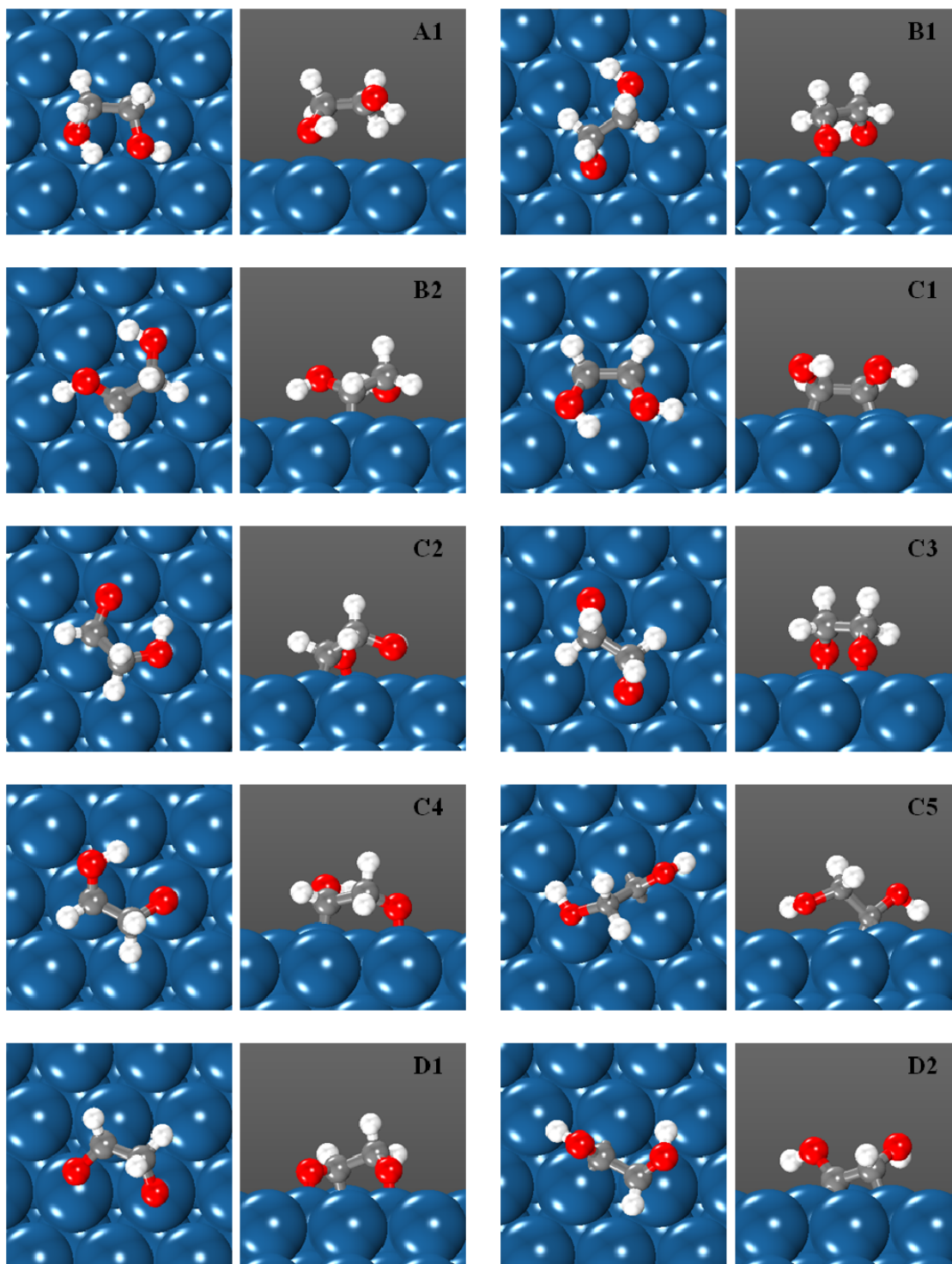
Table C.1. Binding modes and number of occupied surface sites for all surface intermediates.

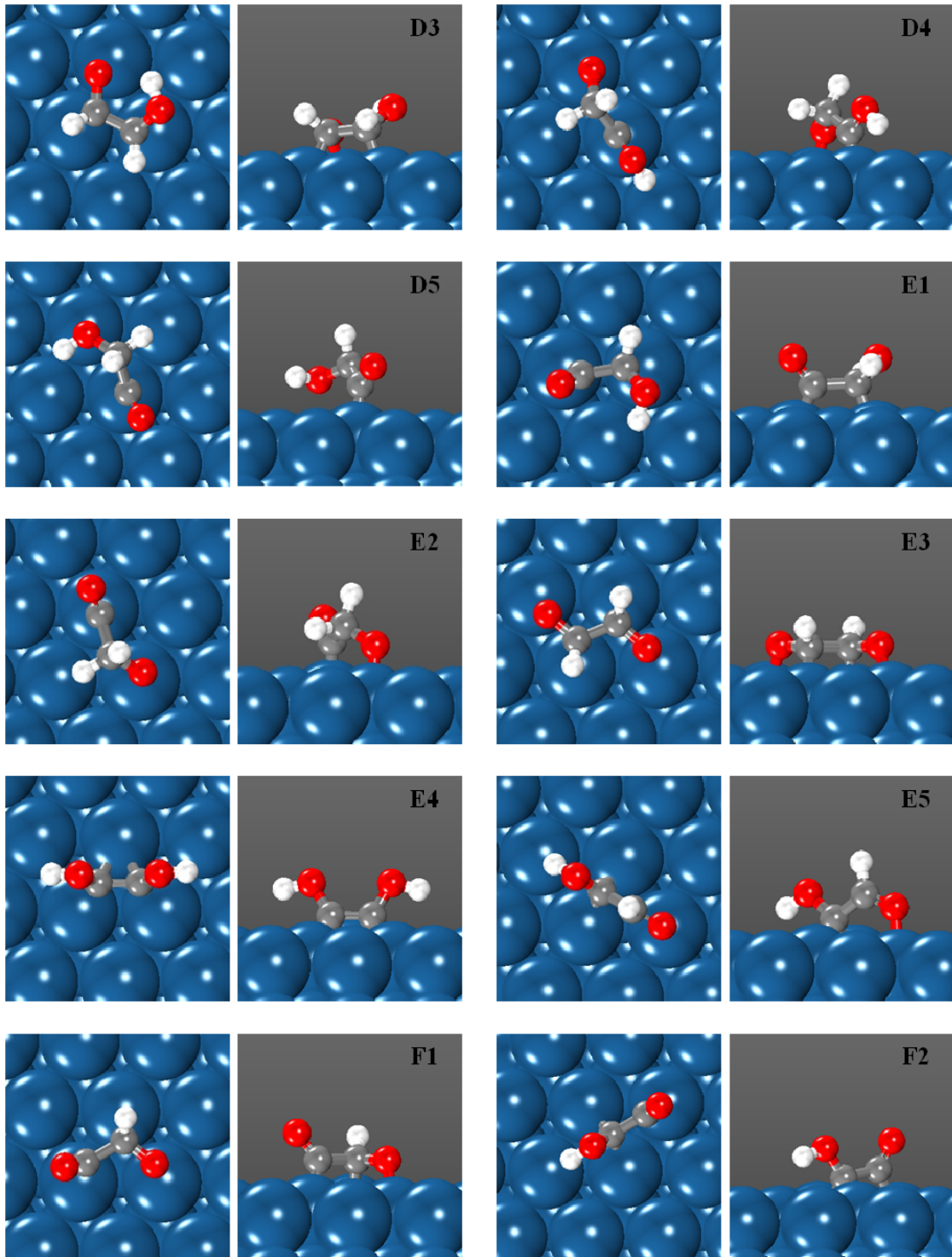
ID	Surface Intermediate	Binding Mode	N_{site}
A1	CH ₂ OHCH ₂ OH	O	2
B1	CH ₂ OCH ₂ OH	O	2
B2	CHOHCH ₂ OH	C	2
C1	CHOHCHOH	C, C	2
C2	CHOCH ₂ OH	C, O	3
C3	CH ₂ OCH ₂ O	O, O	2
C4	CHOHCH ₂ O	C, O	2
C5	COHCH ₂ OH	C _{bridge}	3
D1	CHOCH ₂ O	C, O, O	3
D2	COHCHOH	C, C _{bridge}	2
D3	CHOCHOH	C, C, O	3
D4	COHCH ₂ O	C, O	2
D5	COCH ₂ OH	C	2
E1	COCHOH	C, C	2
E2	COCH ₂ O	C, O	2
E3	CHOCHO	C, C, O, O	4
E4	COHCOH	C _{bridge} , C _{bridge}	2
E5	COHCHO	C _{bridge} , O	2

Table C.1 continued

ID	Surface Intermediate	Binding Mode	N_{site}
F1	COCHO	C, C, O	3
F2	COCOH	C, C _{bridge}	2
G1	COCO	C, C	2
H1	CH ₃ OH	O	1
I1	CH ₃ O	O	1
I2	CH ₂ OH	C	1
J1	CH ₂ O	C, O	2
J2	CHOH	C _{bridge}	1
K1	CHO	C	1
K2	COH	C _{fcc}	1
L1	CO	C _{fcc}	1
M1	H	H _{fcc}	1

Top and side views of most stable structures for all surface intermediates. Identification codes (side views) are listed in Table C.1.





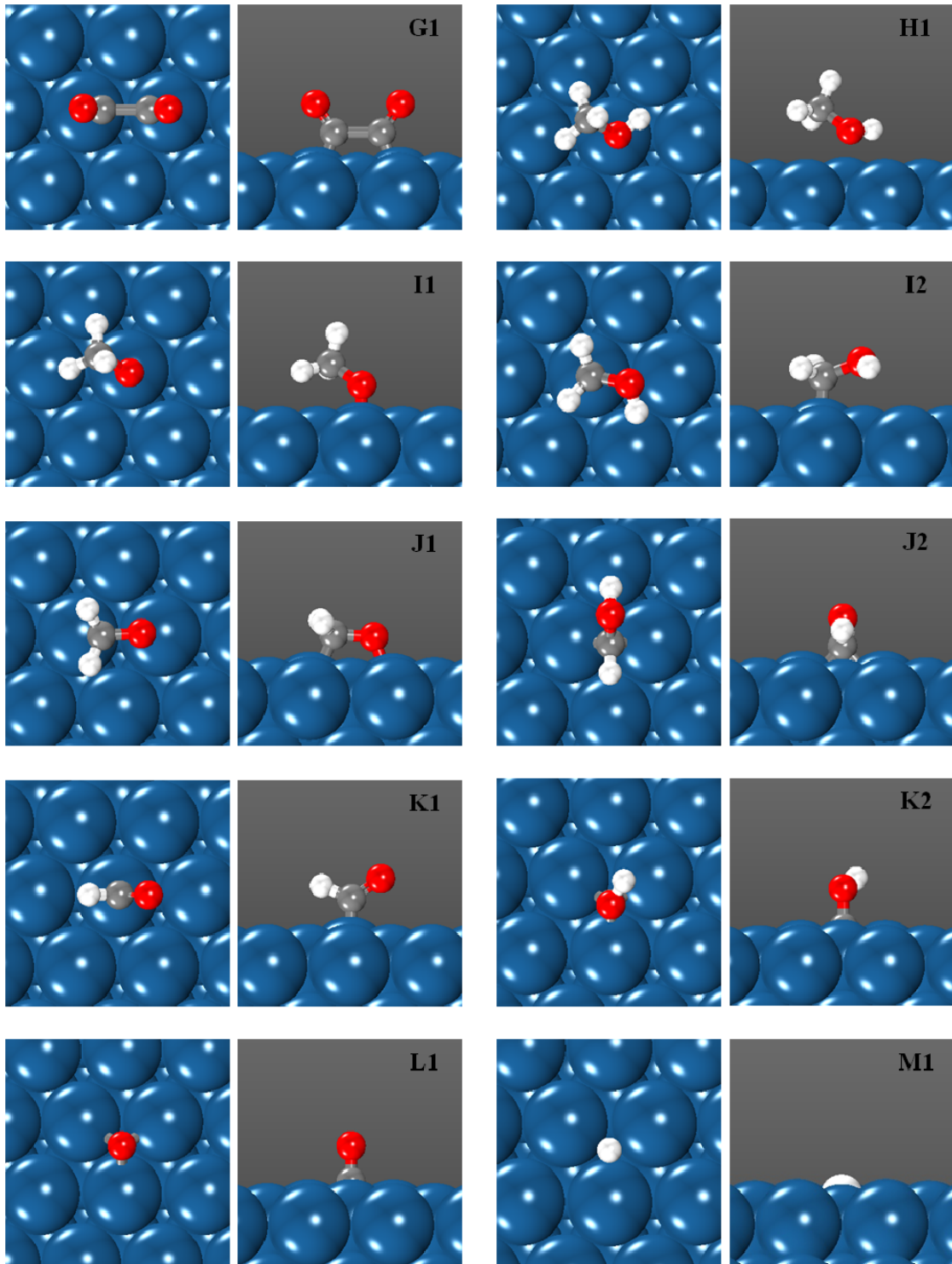


Table C.2. Imaginary frequencies and transition state bond lengths for all surface reactions included in the microkinetic model.

ID	Reaction	ν (cm ⁻¹)	TS Bond length (Å)
CC01	CH ₂ OHCH ₂ OH ** → 2CH ₂ OH *	493 <i>i</i>	2.18
CC02	CHOHCH ₂ OH ** → CHOH * + CH ₂ OH *	281 <i>i</i>	2.43
CC03	CH ₂ OCH ₂ OH ** + * → CH ₂ O ** + CH ₂ OH *	686 <i>i</i>	2.03
CC04	COHCH ₂ OH *** → COH * + CH ₂ OH * + *	455 <i>i</i>	2.09
CC05	CHOHCHOH ** → 2CHOH *	655 <i>i</i>	2.11
CC06	CHOCH ₂ OH *** → CHO * + CH ₂ OH * + *	680 <i>i</i>	1.99
CC07	CHOHCH ₂ O ** + * → CHOH * + CH ₂ O **	474 <i>i</i>	2.14
CC08	CH ₂ OCH ₂ O ** + 2* → 2CH ₂ O **	344 <i>i</i>	2.17
CC09	COCH ₂ OH ** → CO * + CH ₂ OH *	370 <i>i</i>	2.38
CC10	COHCHOH ** → COH * + CHOH *	624 <i>i</i>	2.11
CC11	COHCH ₂ O ** + * → COH * + CH ₂ O **	505 <i>i</i>	2.20
CC12	CHOCHOH *** → CHO * + CHOH * + *	747 <i>i</i>	1.94
CC13	CHOCH ₂ O *** → CHO * + CH ₂ O **	552 <i>i</i>	2.02
CC14	COCHOH ** → CO * + CHOH *	567 <i>i</i>	2.03
CC15	COCH ₂ O ** + * → CO * + CH ₂ O **	429 <i>i</i>	2.09
CC16	COHCOH ** → 2COH *	268 <i>i</i>	1.84
CC17	COHCHO ** → COH * + CHO *	568 <i>i</i>	2.01
CC18	CHOCHO **** → 2CHO * + 2*	691 <i>i</i>	1.77
CC19	COCOH ** → CO * + COH *	618 <i>i</i>	1.96
CC20	COCHO *** → CO * + CHO * + *	511 <i>i</i>	1.84
CC21	COCO ** → 2CO *	423 <i>i</i>	1.89
CH01	CH ₂ OHCH ₂ OH ** + * → CHOHCH ₂ OH ** + H *	880 <i>i</i>	1.48
CH02	CHOHCH ₂ OH ** + 2* → COHCH ₂ OH *** + H *	762 <i>i</i>	1.44
CH03	CHOHCH ₂ OH ** + * → CHOHCHOH ** + H *	570 <i>i</i>	1.66
CH04	CH ₂ OCH ₂ OH ** + 2* → CHOCH ₂ OH *** + H *	546 <i>i</i>	1.57

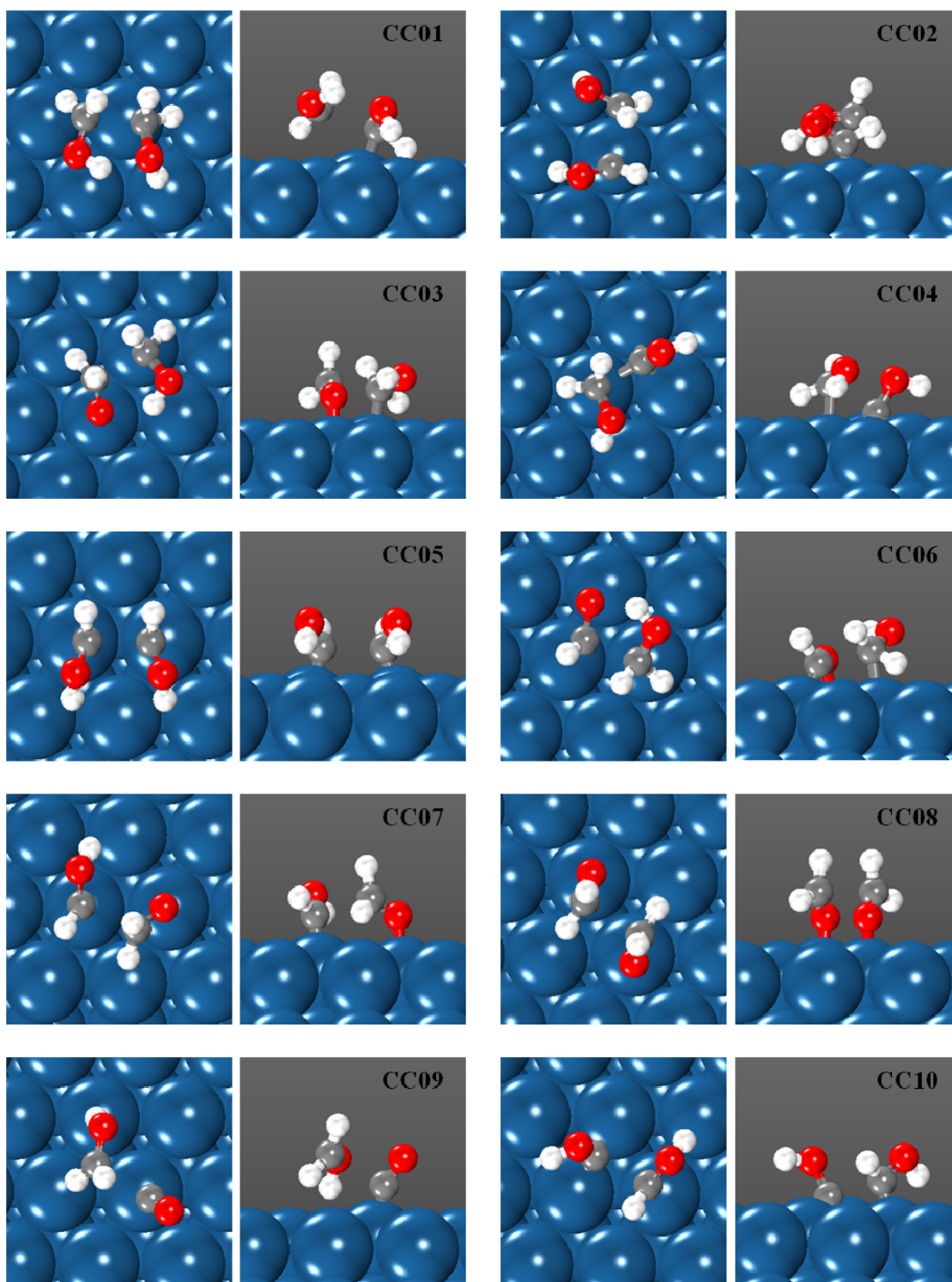
Table C.2 continued

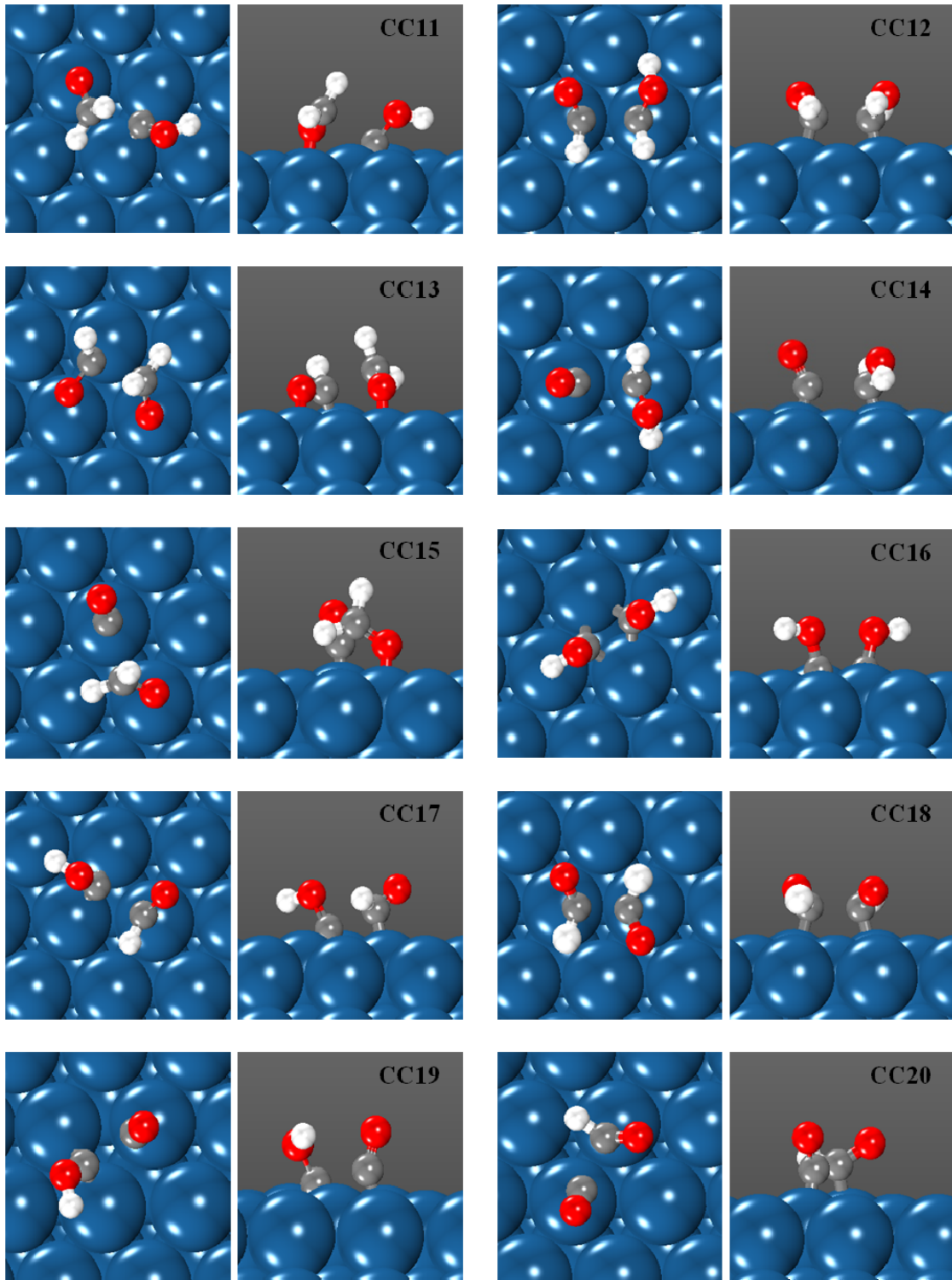
ID	Reaction	ν (cm ⁻¹)	TS Bond length (Å)
CH05	CH ₂ OCH ₂ OH ^{**+*} → CHOCH ₂ O ^{**+H*}	727i	1.66
CH06	COHCH ₂ OH ^{***} → COHCHOH ^{**+H*}	769i	1.54
CH07	CHOHCHOH ^{**+*} → COHCHOH ^{**+H*}	775i	1.51
CH08	CHOCH ₂ OH ^{***} → COCH ₂ OH ^{**+H*}	475i	1.33
CH09	CHOCH ₂ OH ^{***+*} → CHOCHOH ^{***+H*}	873i	1.52
CH10	CHOHCH ₂ O ^{**+*} → COHCH ₂ O ^{**+H*}	970i	1.45
CH11	CHOHCH ₂ O ^{**+2*} → CHOCHOH ^{***+H*}	611i	1.57
CH12	CH ₂ OCH ₂ O ^{**+2*} → CHOCH ₂ O ^{***+H*}	594i	1.60
CH13	COHCHOH ^{**+*} → COHCOH ^{**+H*}	1024i	1.43
CH14	COCH ₂ OH ^{**+*} → COCHOH ^{**+H*}	697i	1.53
CH15	CHOCHOH ^{***} → COCHOH ^{**+H*}	600i	1.45
CH16	CHOCHOH ^{***} → COHCHO ^{**+H*}	739i	1.57
CH17	COHCH ₂ O ^{**+*} → COHCHO ^{**+H*}	709i	1.53
CH18	CHOCH ₂ O ^{***} → COCH ₂ O ^{**+H*}	200i	1.35
CH19	CHOCH ₂ O ^{***+2*} → CHOCHO ^{****+H*}	582i	1.56
CH20	COCHOH ^{**+*} → COCOH ^{**+H*}	826i	1.54
CH21	COHCHO ^{**+*} → COCOH ^{**+H*}	262i	1.36
CH22	COCH ₂ O ^{**+2*} → COCHO ^{***+H*}	677i	1.59
CH23	CHOCHO ^{****} → COCHO ^{***+H*}	437i	1.39
CH24	COCHO ^{***} → COCO ^{**+H*}	465i	1.39
CH25	CH ₃ OH ^{*+*} → CH ₂ OH ^{*+H*}	798i	1.63
CH26	CH ₃ O ^{*+2*} → CH ₂ O ^{**+H*}	604i	1.59
CH27	CH ₂ OH ^{*+*} → CHOH ^{*+H*}	743i	1.66
CH28	CH ₂ O ^{**} → CHO ^{*+H*}	156i	1.44
CH29	CHOH ^{*+*} → COH ^{*+H*}	241i	1.51
CH30	CHO ^{*+*} → CO ^{*+H*}	243i	1.60

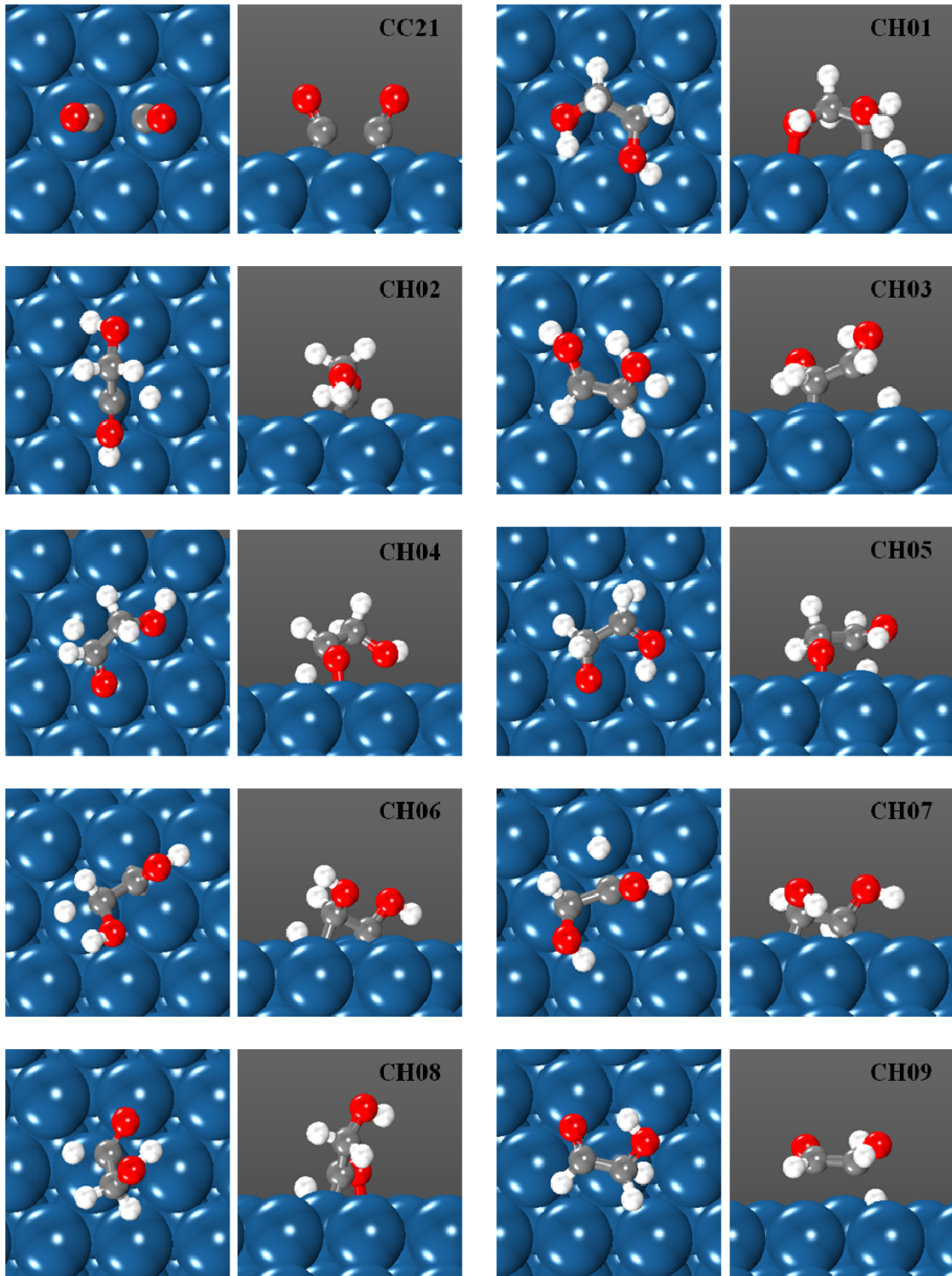
Table C.2 continued

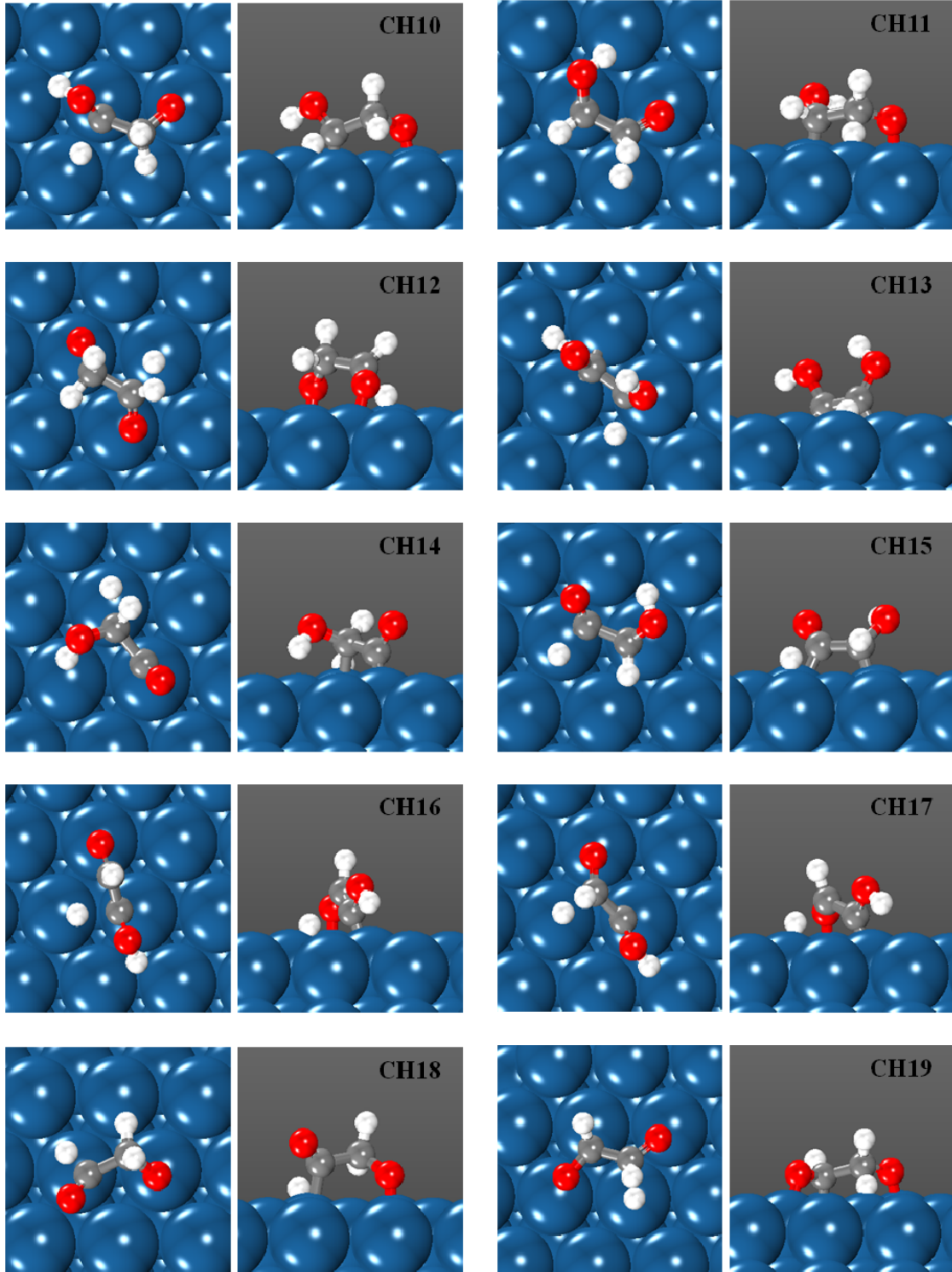
ID	Reaction	ν (cm ⁻¹)	TS Bond length (Å)
OH01	CH ₂ OHCH ₂ OH ^{**+*} → CH ₂ OCH ₂ OH ^{**+H*}	381 <i>i</i>	1.36
OH02	CH ₂ OCH ₂ OH ^{**+*} → CH ₂ OCH ₂ O ^{**+H*}	372 <i>i</i>	1.69
OH03	CHOHCH ₂ OH ^{**+2*} → CHOCH ₂ OH ^{***+H*}	290 <i>i</i>	1.58
OH04	CHOHCH ₂ OH ^{**+*} → CHO _H CH ₂ O ^{**+H*}	990 <i>i</i>	1.62
OH05	CHOCH ₂ OH ^{***+*} → CHOCH ₂ O ^{***+H*}	677 <i>i</i>	1.34
OH06	CHOHCH ₂ O ^{**+2*} → CHOCH ₂ O ^{***+H*}	448 <i>i</i>	1.57
OH07	COHCH ₂ OH ^{***} → COCH ₂ OH ^{**+H*}	757 <i>i</i>	1.35
OH08	COHCH ₂ OH ^{***} → COHCH ₂ O ^{**+H*}	356 <i>i</i>	1.70
OH09	CHOHCHOH ^{**+2*} → CHOCHOH ^{***+H*}	420 <i>i</i>	1.45
OH10	COCH ₂ OH ^{**+*} → COCH ₂ O ^{**+H*}	396 <i>i</i>	1.36
OH11	COHCH ₂ O ^{**+*} → COCH ₂ O ^{**+H*}	1028 <i>i</i>	1.44
OH12	CHOCHO _H ^{***+2*} → CHOCHO ^{****+H*}	391 <i>i</i>	1.46
OH13	COHCHOH ^{**+*} → COCHOH ^{**+H*}	1049 <i>i</i>	1.53
OH14	COHCHOH ^{**+*} → COHCHO ^{**+H*}	210 <i>i</i>	1.57
OH15	COCHOH ^{**+2*} → COCHO ^{***+H*}	829 <i>i</i>	1.46
OH16	COHCHO ^{**+2*} → COCHO ^{***+H*}	1141 <i>i</i>	1.27
OH17	COHCOH ^{**+*} → COCOH ^{**+H*}	921 <i>i</i>	1.34
OH18	COCOH ^{**+*} → COCO ^{**+H*}	878 <i>i</i>	1.26
OH19	CH ₃ OH ^{*+*} → CH ₃ O ^{*+H*}	293 <i>i</i>	1.71
OH20	CH ₂ OH ^{*+2*} → CH ₂ O ^{**+H*}	555 <i>i</i>	1.57
OH21	CHOH ^{*+*} → CHO ^{*+H*}	500 <i>i</i>	1.57
OH22	COH ^{*+*} → CO ^{*+H*}	1517 <i>i</i>	1.31

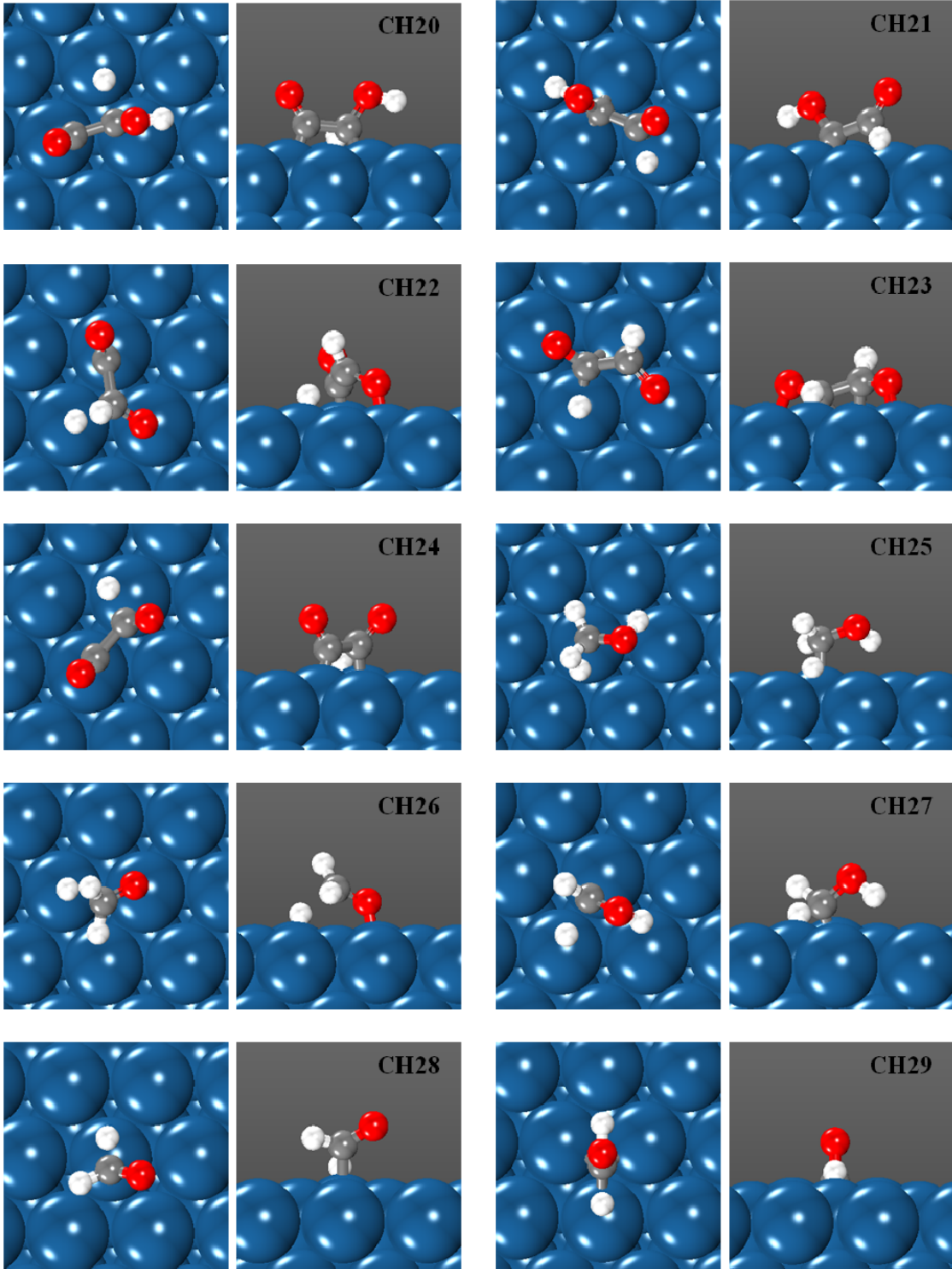
Top and side views of transition state structures for all surface reactions. Identification codes (side views) are listed in Table C.2.

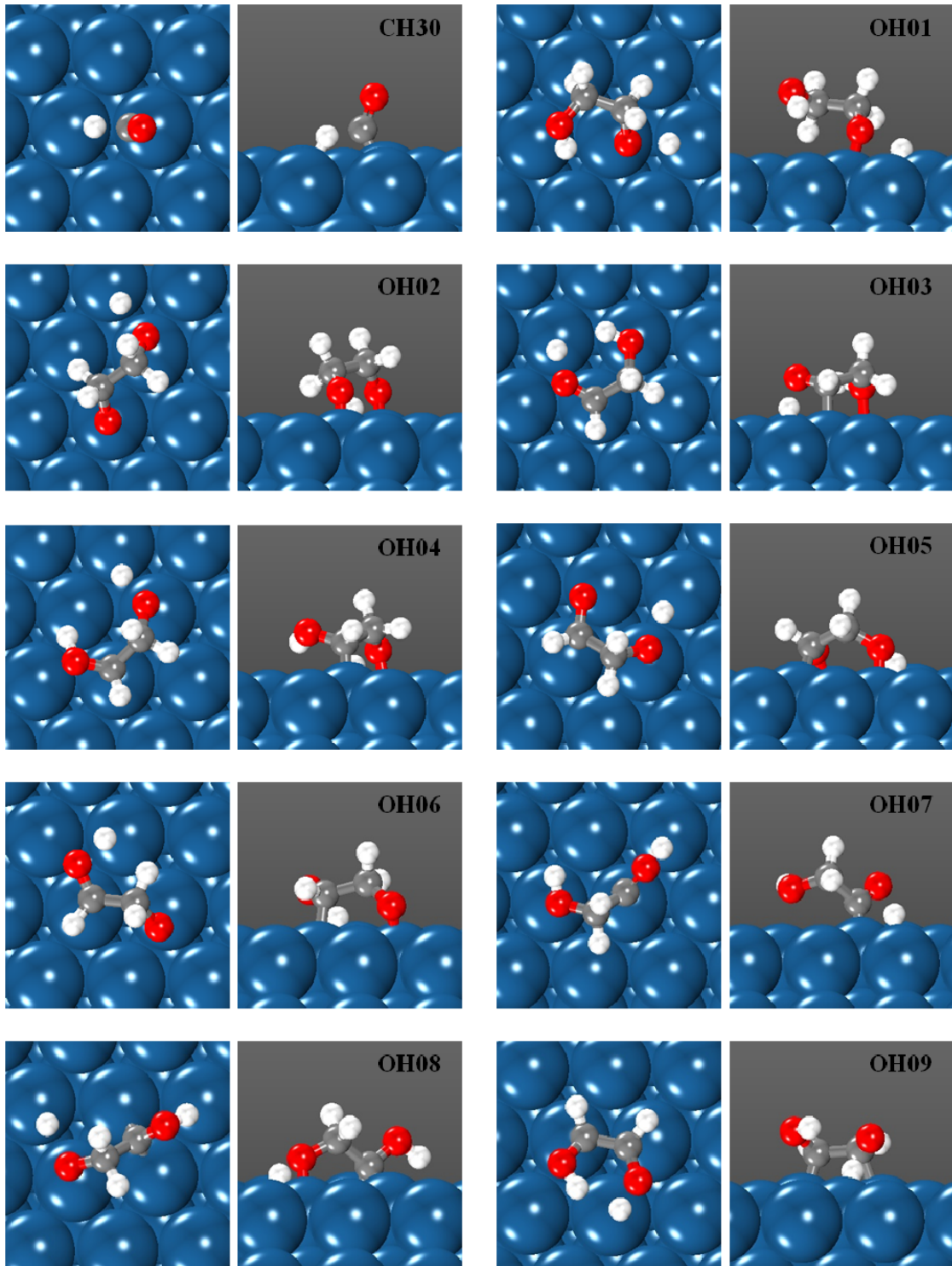


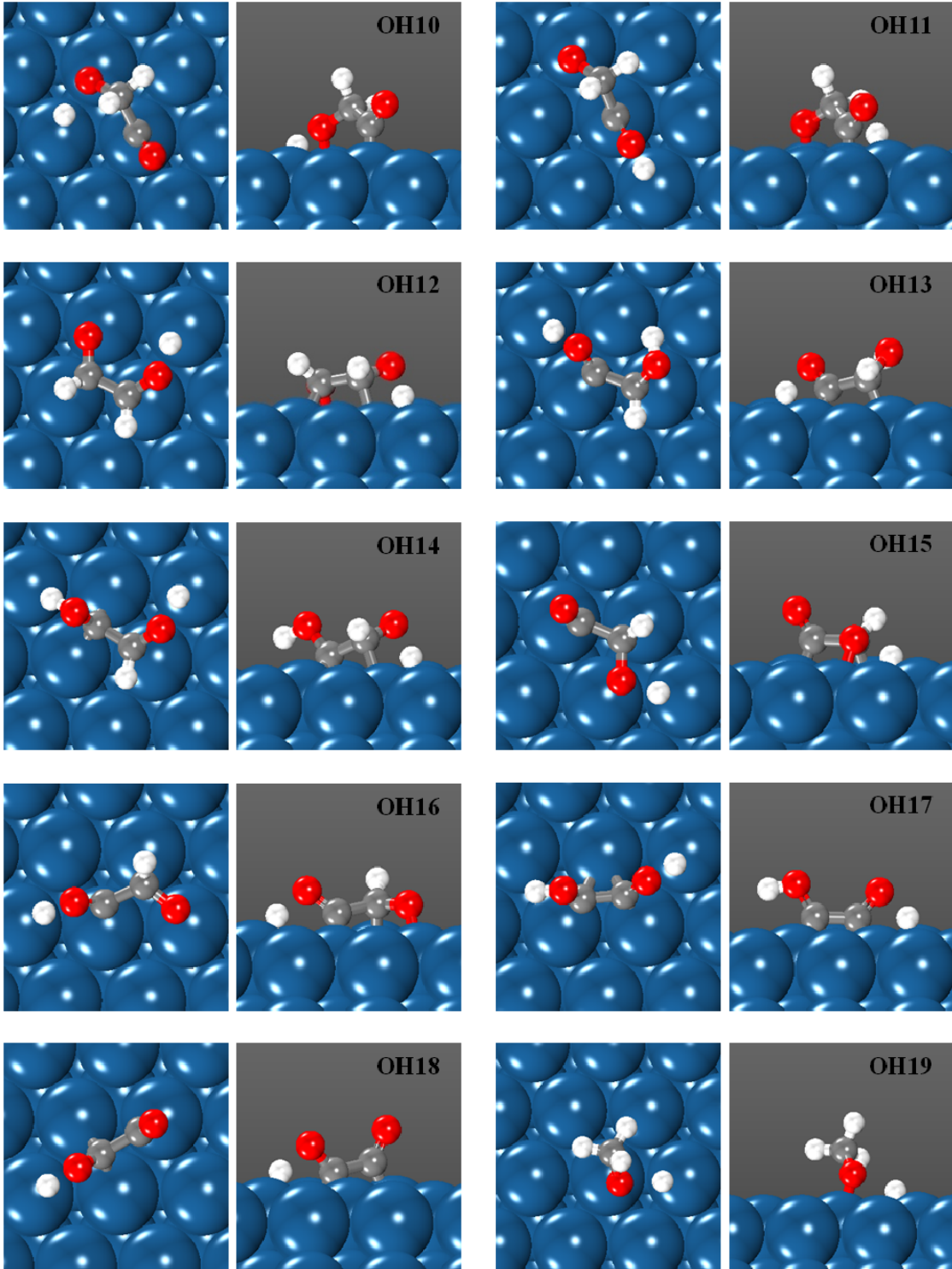












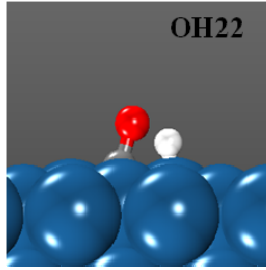
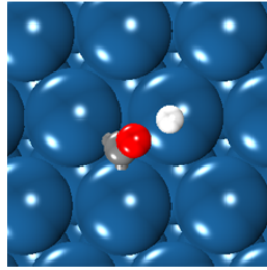
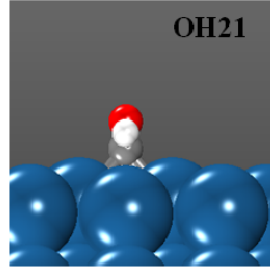
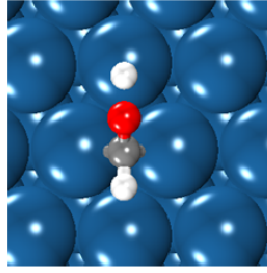
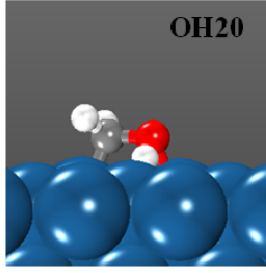
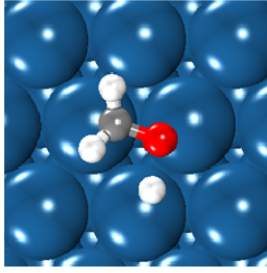


Table C.3. Number of unique structures used for fitting CO–CO and H–H lateral interactions.

θ (CO or H)	N
1/36	1
1/9	1
2/9	2
3/9	5
4/9	5
5/9	5
6/9	5
7/9	2
8/9	1
9/9	1

Table C.4. Number of unique structures used for fitting EG–CO and EG–H lateral interactions (EG = Ethylene Glycol).

θ (CO or H)	θ_{EG}	N
1/16	1/16	8

Table C.5. Number of unique structures used for fitting CO–H lateral interactions.

θ_{co}	θ_{H}	N
1/9	1/9	2
1/9	2/9	7
1/9	3/9	13
1/9	4/9	18
1/9	5/9	13
1/9	6/9	7
1/9	7/9	2
1/9	8/9	1
2/9	1/9	7
2/9	2/9	18
2/9	3/9	32
2/9	4/9	32
2/9	5/9	18
2/9	6/9	7
2/9	7/9	2
3/9	1/9	13
3/9	2/9	32
3/9	4/9	32
3/9	5/9	13
3/9	6/9	5
4/9	1/9	18
4/9	2/9	32

APPENDIX D

PERMISSION TO REPRINT



RightsLink®

[Home](#)

[Account Info](#)

[Help](#)



ACS Publications
MOST TRUSTED. MOST CITED. MOST READ.

Title: New Implicit Solvation Scheme for Solid Surfaces
Author: Muhammad Faheem, Suwit Suthirakun, and Andreas Heyden
Publication: The Journal of Physical Chemistry C
Publisher: American Chemical Society
Date: Oct 1, 2012

Logged in as:
Muhammad Faheem
Account #:
3000797579

[LOGOUT](#)

Copyright © 2012, American Chemical Society

PERMISSION/LICENSE IS GRANTED FOR YOUR ORDER AT NO CHARGE

This type of permission/license, instead of the standard Terms & Conditions, is sent to you because no fee is being charged for your order. Please note the following:

- Permission is granted for your request in both print and electronic formats, and translations.
- If figures and/or tables were requested, they may be adapted or used in part.
- Please print this page for your records and send a copy of it to your publisher/graduate school.
- Appropriate credit for the requested material should be given as follows: "Reprinted (adapted) with permission from (COMPLETE REFERENCE CITATION). Copyright (YEAR) American Chemical Society." Insert appropriate information in place of the capitalized words.
- One-time permission is granted only for the use specified in your request. No additional uses are granted (such as derivative works or other editions). For any other uses, please submit a new request.



Title: Hybrid Quantum
Mechanics/Molecular Mechanics
Solvation Scheme for Computing
Free Energies of Reactions at
Metal–Water Interfaces

Logged in as:
Muhammad Faheem
Account #:
3000797579

[LOGOUT](#)

Author: Muhammad Faheem and
Andreas Heyden

Publication: Journal of Chemical Theory and
Computation

Publisher: American Chemical Society

Date: Jun 1, 2014

Copyright © 2014, American Chemical Society

PERMISSION/LICENSE IS GRANTED FOR YOUR ORDER AT NO CHARGE

This type of permission/license, instead of the standard Terms & Conditions, is sent to you because no fee is being charged for your order. Please note the following:

- Permission is granted for your request in both print and electronic formats, and translations.
- If figures and/or tables were requested, they may be adapted or used in part.
- Please print this page for your records and send a copy of it to your publisher/graduate school.
- Appropriate credit for the requested material should be given as follows: "Reprinted (adapted) with permission from (COMPLETE REFERENCE CITATION). Copyright (YEAR) American Chemical Society." Insert appropriate information in place of the capitalized words.
- One-time permission is granted only for the use specified in your request. No additional uses are granted (such as derivative works or other editions). For any other uses, please submit a new request.

American Chemical Society's Policy on Theses and Dissertations

If your university requires you to obtain permission, you must use the RightsLink permission system.
See RightsLink instructions at <http://pubs.acs.org/page/copyright/permissions.html>.

This is regarding request for permission to include your paper(s) or portions of text from your paper(s) in your thesis. Permission is now automatically granted; please pay special attention to the **implications** paragraph below. The Copyright Subcommittee of the Joint Board/Council Committees on Publications approved the following:

Copyright permission for published and submitted material from theses and dissertations

ACS extends blanket permission to students to include in their theses and dissertations their own articles, or portions thereof, that have been published in ACS journals or submitted to ACS journals for publication, provided that the ACS copyright credit line is noted on the appropriate page(s).

Publishing implications of electronic publication of theses and dissertation material

Students and their mentors should be aware that posting of theses and dissertation material on the Web prior to submission of material from that thesis or dissertation to an ACS journal may affect publication in that journal. Whether Web posting is considered prior publication may be evaluated on a case-by-case basis by the journal's editor. If an ACS journal editor considers Web posting to be "prior publication", the paper will not be accepted for publication in that journal. If you intend to submit your unpublished paper to ACS for publication, check with the appropriate editor prior to posting your manuscript electronically.

Reuse/Republishing of the Entire Work in Theses or Collections: Authors may reuse all or part of the Submitted, Accepted or Published Work in a thesis or dissertation that the author writes and is required to submit to satisfy the criteria of degree-granting institutions. Such reuse is permitted subject to the ACS' "Ethical Guidelines to Publication of Chemical Research" (<http://pubs.acs.org/page/policy/ethics/index.html>); the author should secure written confirmation (via letter or email) from the respective ACS journal editor(s) to avoid potential conflicts with journal prior publication*/embargo policies. Appropriate citation of the Published Work must be made. If the thesis or dissertation to be published is in electronic format, a direct link to the Published Work must also be included using the ACS Articles on Request author-directed link – see <http://pubs.acs.org/page/policy/articlesonrequest/index.html>

* Prior publication policies of ACS journals are posted on the ACS website at <http://pubs.acs.org/page/policy/prior/index.html>

If your paper has **not** yet been published by ACS, please print the following credit line on the first page of your article: "Reproduced (or 'Reproduced in part') with permission from [JOURNAL NAME], in press (or 'submitted for publication'). Unpublished work copyright [CURRENT YEAR] American Chemical Society." Include appropriate information.

If your paper has already been published by ACS and you want to include the text or portions of the text in your thesis/dissertation, please print the ACS copyright credit line on the first page of your article: "Reproduced (or 'Reproduced in part') with permission from [FULL REFERENCE CITATION.] Copyright [YEAR] American Chemical Society." Include appropriate information.

Submission to a Dissertation Distributor: If you plan to submit your thesis to UMI or to another dissertation distributor, you should not include the unpublished ACS paper in your thesis if the thesis will be disseminated electronically, until ACS has published your paper. After publication of the paper by ACS, you may release the entire thesis (**not the individual ACS article by itself**) for electronic dissemination through the distributor; ACS's copyright credit line should be printed on the first page of the ACS paper.

10/10/03, 01/15/04, 06/07/06, 04/07/10, 08/24/10, 02/28/11